
**Sensitivity studies for a search for charginos in final
states with one lepton with the ATLAS detector
and interpretation of a search for gluinos and
squarks in the pMSSM**



LUDWIG-MAXIMILIANS-UNIVERSITY MUNICH
FACULTY OF PHYSICS

MASTER THESIS

Eric Schanet

September 2018

**Sensitivitätsstudien zu einer Suche nach Charginos
in Endzuständen mit einem Lepton mit dem
ATLAS Detektor und Interpretation einer Suche
nach Gluinos und Squarks im pMSSM**



LUDWIG-MAXIMILIANS-UNIVERSITÄT MÜNCHEN
FAKULTÄT FÜR PHYSIK

MASTERARBEIT

Eric Schanet

September 2018

Supervisor: Prof. Dr. Dorothee Schaile

Abstract

Supersymmetry is a promising extension of the Standard Model of Particle Physics. It provides a mathematically elegant solution to some of the open questions of the Standard Model. Supersymmetry can, for example, provide a candidate particle for dark matter.

In the first part of this work, ideas for an analysis in a final state with one lepton, searching for the electroweak production of charginos with decays to W bosons and the lightest supersymmetric particles, using the ATLAS detector, are presented. Due to low cross-sections of chargino pair production and a high similarity to Standard Model backgrounds, this specific decay got only recently into reach of the LHC experiments. Using the presented ideas, statements about this model can be made for the first time in final states with one lepton.

In the second part of this work, a simplification of a published analysis searching for gluinos and squarks in events with exactly one lepton, multiple jets and missing transverse momentum is presented. The simplification allows to interpret the analysis in a large number of different models belonging to the phenomenological MSSM. Using this approximation, a precise statement about the sensitivity of the analysis to a class of more complete supersymmetric models (in comparison to simplified models) can be made for the first time.

Zusammenfassung

Supersymmetrie ist eine vielversprechende theoretische Erweiterung des Standardmodells der Teilchenphysik und liefert mathematisch elegante Lösungen zu mehreren offenen Fragen des Standardmodells. Viele supersymmetrische Modelle liefern, zum Beispiel, einen Kandidaten für dunkle Materie.

Im ersten Teil dieser Arbeit werden Ideen für eine Suche nach elektroschwacher Produktion von Charginos mit anschließendem Zerfall in W Bosonen und leichteste supersymmetrische Teilchen, in Ereignissen mit einem Lepton mit dem ATLAS Detektor, vorgestellt. Aufgrund der niedrigen Wirkungsquerschnitte für die Produktion von Charginos sowie der starken Ähnlichkeit zu Standardmodell Untergründen, gelang dieses spezielle Modell erst kürzlich in Reichweite der LHC Experimente. Mit den vorgestellten Ansätzen ist es erstmals möglich, eine Aussage über dieses Modell in Endzuständen mit einem Lepton zu treffen.

Im zweiten Teil dieser Arbeit wird eine Vereinfachung einer Suche nach Gluinos und Squarks in Endzuständen mit exakt einem Lepton, Jets und fehlender transversaler Energie vorgestellt. Die Vereinfachung erlaubt die Interpretation der Analyse in einer großen Anzahl von Modellen des phänomenologischen MSSM. Mit dieser Approximation ist es erstmals möglich, eine präzise Aussage über die Sensitivität der Analyse in vollständigeren supersymmetrischen Modellen (verglichen mit vereinfachten Modellen) zu machen.

Contents

1 Theory	3
1.1 The Standard Model of Particle Physics	3
1.1.1 Quantum field theories	4
1.1.2 Gauge symmetries	5
1.1.3 Particle content	7
1.2 Supersymmetry	9
1.2.1 Limitations and open questions of the SM	9
1.2.2 Mathematical description	12
1.2.3 Supersymmetry breaking	13
1.2.4 Particle content in the MSSM	14
1.2.5 R-parity	15
1.2.6 Simplified models	16
1.2.7 The phenomenological MSSM	17
2 The LHC and ATLAS	19
2.1 The Large Hadron Collider	19
2.2 The ATLAS Experiment	21
2.2.1 Coordinate System	21
2.2.2 Subdetectors	22
2.2.3 Trigger system	24
3 Data and Monte Carlo Simulation	25
3.1 Data	25
3.2 Monte Carlo simulation	26

3.2.1	Used Monte Carlo samples	27
4	The 1-lepton final state	29
4.1	Analyses overview	29
4.2	Standard Model backgrounds	31
4.3	Object definitions and event selection	33
4.3.1	Event selection	33
4.3.2	Electrons	33
4.3.3	Muons	34
4.3.4	Jets	35
4.3.5	B-tagging	35
4.3.6	Missing transverse momentum	36
4.4	Overlap removal	36
5	Statistical data analysis	39
5.1	Likelihood	39
5.2	Test statistics	40
5.3	p -values	41
6	Sensitivity studies for electroweak Supersymmetry	43
6.1	Discriminating observables	43
6.2	Optimisation methods	51
6.2.1	Multidimensional cut scan	51
6.2.2	N-1 plots	53
6.3	Cut optimisation	53
6.3.1	Setup and technical details	53
6.3.2	Optimisation results	54
6.4	Preliminary signal region definition	62
6.5	Multi-bin approach	64
6.5.1	Method	64
6.5.2	Setups and results	65
6.6	Multivariate approach	70

6.6.1	General method and technical details	71
6.6.2	Input data	72
6.6.3	Setup	73
6.6.4	Results	76
6.7	Discussion	79
7	Sensitivity of the 1-lepton analysis to the phenomenological MSSM	81
7.1	Motivation and procedure	81
7.1.1	Smearing algorithms	83
7.1.2	Simplified shape fit	84
7.2	Truth- and reco-level comparisons	86
7.2.1	Comparison at preselection level	86
7.2.2	Comparison in the signal regions	90
7.3	Simplified shape fit application	90
7.4	Application on pMSSM signal samples	96
7.4.1	Model generation	96
7.4.2	Observed exclusion power improvement	96
7.4.3	Future prospects	99
8	Summary	103
Bibliography		105
Symbols		113
Appendix A		117
A.1	N-1 plots for cut-scan results	117
A.2	Truth- and full-reconstruction-level comparisons	126
A.3	Available statistics for training MLP	128
Appendix B		129
B.1	Scatter plots comparing truth and reco yields in the SRs	129
B.2	Available truth samples for the gluino one-step model	132
B.3	pMSSM parameter scan ranges	133

Introduction

Particle physics studies the fundamental constituents and interactions of matter. The theoretical framework used to describe nature at the subatomic scale is called the Standard Model of Particle Physics. It has been developed throughout the second half of the 20th century and is one of the most successful physical theories to date. The predictions provided by the Standard Model have been found to match experimental results at an unprecedented precision. Even at the high energies achievable with modern accelerator technologies, no new physics beyond the Standard Model has been discovered so far.

It is, however, evident that the Standard Model cannot be a complete theory of nature. It fails, for example, to correctly describe phenomena that become apparent on cosmological scales. For example, the Standard Model only describes three of the four fundamental forces of the universe, namely the strong, weak and electromagnetic interactions. Gravity, the last of the four fundamental forces, is not described by the Standard Model. Furthermore, although many astronomical observations indicate the existence of dark matter, the Standard Model is unable to provide a suitable candidate particle for it. It seems that the Standard Model, even though extremely precise and successful, is only a low-energy approximation to a more fundamental theory of nature.

A plethora of theories aiming to explain these deficiencies exists. One very promising class of theories is Supersymmetry. It extends the Standard Model by associating supersymmetric partners to the Standard Model particles and could, for example, be able to provide a candidate for dark matter. Although the first supersymmetric theories have already been proposed in the 1970s [1], no supersymmetric particles have been found so far. With a centre-of-mass energy of 13 TeV attained by the Large Hadron Collider in 2015, and maybe even 14 TeV in 2021 [2], there is still the possibility that supersymmetric particles could be found in the data collected with the ATLAS detector in the coming years.

In this work, various improvements to an analysis searching for supersymmetric particles in events with exactly one lepton (electron or muon), multiple jets and missing transverse momentum with the ATLAS detector are presented. After an introduction to the Standard Model and Supersymmetry, a brief overview of the Large Hadron Collider and the ATLAS experiment is given. Then, details on the simulations used and data collected are discussed, followed by a description of the physics objects used within this work and a discussion of the methods needed for statistical data analysis. In chapter 6, possibilities for a search to

electroweak production of supersymmetric particles by means of a specific supersymmetric model are presented and discussed. Chapter 7 presents studies to broaden the scope of the search to the phenomenological MSSM, a class of supersymmetric models with 19 parameters.

Chapter 1

Theory

The supersymmetric particles considered in this work mostly decay into the well-known particles of the Standard Model of Particle Physics (SM). This chapter therefore aims to give an overview on the SM, followed by an introduction to the concepts and motivations of Supersymmetry which solves some of the short-comings of the SM.

1.1 The Standard Model of Particle Physics

Since the discovery of the electron in 1897 by J.J.Thomson [3], an observation that is often considered to be the birth of particle physics itself, physicists have made extraordinary progress in describing nature at the microscopic scale. Today, over 120 years and many theoretical and experimental milestones later, the resulting theoretical framework, the Standard Model of Particle Physics (SM), provides a precise and predictive description of the interactions of elementary particles. It has been experimentally tested and verified to a high degree of precision up to the electroweak (EWK) scale.

Due to its success in delivering extremely precise predictions of the interactions between elementary particles, it is not surprising that the history of the SM is paved with numerous awards, both for theoretical and experimental work. For example, in 1979, Glashow, Weinberg and Salam (GWS) were awarded with the Nobel Prize for their work leading to the electroweak unification. A few years later, in 1984, the Nobel prize was awarded to Carlo Rubbia and Simon van der Meer for their work resulting in the observation of the W^\pm and Z bosons, the mediators of the weak force that were theoretically predicted by GWS through the electroweak unification. The most prominent recent progress is the discovery of the Higgs (H) boson in 2012, that not only led to the Nobel prize being awarded to Higgs and Englert for their theoretical prediction, but also completed the SM with its last particle being discovered roughly 50 years after its prediction. In its current state, the SM successfully describes three of the four fundamental forces in the universe, namely the electromagnetic, the weak, and the strong interaction. This leaves gravity as the only fundamental force not described by the SM.

The following mathematical description of the SM follows, if not otherwise indicated, Refs. [4, 5].

1.1.1 Quantum field theories

From a mathematical point of view, the SM is a collection of a special type of quantum field theories, called gauge theories. Quantum field theory (QFT) is the unification of field theory with relativistic quantum mechanics and gives a uniform description of quantum mechanical particles and classical fields while including special relativity.

In classical mechanics, a particle can be described as a discrete point mass of which the position in space is a function of time. By introducing a Lagrangian $L(q_i, \dot{q}_i)$ depending on the coordinates q_i and velocities \dot{q}_i of the particle, the equation of motion of the particle can be determined through the Euler-Lagrange equation

$$\frac{d}{dt} \left(\frac{\partial L}{\partial \dot{q}_i} \right) - \frac{\partial L}{\partial q_i} = 0. \quad (1.1)$$

In quantum field theory, however, particles are no longer considered to be localized mass points but excitations in an underlying field occupying a certain region of space. These continuous fields need to be described by one or more functions of space and time $\phi_i(\vec{x}, t)$. Similar to classical mechanics though, quantum field theory also introduces a Lagrangian, or rather a Lagrangian density $\mathcal{L}(\phi_i, \partial_\mu \phi_i)$ that is a function of one or more fields and its spacetime derivatives. The spacetime integral of the Lagrangian density is the action

$$S = \int \mathcal{L}(\phi_i, \partial_\mu \phi_i) d^4x. \quad (1.2)$$

Using the principle of least action $\delta S = 0$, the equation of motion of each field in the Lagrangian density is given by the Euler-Lagrange equation,

$$\partial_\mu \left(\frac{\partial \mathcal{L}}{\partial (\partial_\mu \phi_i)} \right) - \frac{\partial \mathcal{L}}{\partial \phi_i} = 0. \quad (1.3)$$

Taking for example the free Dirac Lagrangian for a spin-1/2 field,

$$\mathcal{L} = \bar{\psi} (i\gamma^\mu \partial_\mu) \psi - m\bar{\psi}\psi, \quad (1.4)$$

and applying eq. (1.3) on the adjoint spinor $\bar{\psi}$ yields

$$i\gamma^\mu \partial_\mu \psi - m\psi = 0, \quad (1.5)$$

which is the Dirac equation describing a particle of spin 1/2 and mass m in a quantum field theory.

1.1.2 Gauge symmetries

Symmetries are of central importance for the SM. As Emmy Noether has shown in 1918 [6], symmetries of the action of a physical system lead to conservation laws. In classical mechanics the invariance of laws of physics under spatial translations gives rise to momentum conservation and, similarly, the invariance under time translations results in energy conservation.

Taking again the example of the Dirac Lagrangian in eq. (1.4), it is worth noting that this Lagrangian is invariant under a global phase transformation

$$\psi \rightarrow e^{i\theta} \psi, \quad (1.6)$$

where θ is real and spacetime independent. According to Noether's theorem, the existence of global symmetries in the SM is related to the conservation of charge-like quantum numbers. But even more important than the existence of global symmetries in the SM is the procedure of enforcing these global symmetries to hold locally. In the SM, the introduction of local symmetries, called gauge symmetries, directly dictates the existence of massless gauge fields and their corresponding gauge particles.

Turning again to the free Dirac Lagrangian, it is clear that a local phase transformation (where the phase θ is a function of spacetime)

$$\psi \rightarrow e^{i\theta(x)} \psi, \quad (1.7)$$

does not leave the Lagrangian invariant, since it picks up an additional term from the derivative of θ , leading to

$$\mathcal{L} \rightarrow \mathcal{L} - (\partial_\mu \theta) \bar{\psi} \gamma^\mu \psi. \quad (1.8)$$

However, by introducing a new gauge field $A_\mu(x)$ that transforms under local phase transformations according to

$$A_\mu \rightarrow A_\mu - \frac{1}{e} \partial_\mu \theta(x), \quad (1.9)$$

and furthermore replacing the derivative ∂_μ by the covariant derivative[†]

$$D_\mu \equiv \partial_\mu + ieA_\mu, \quad (1.10)$$

the Lagrangian in eq. (1.4) becomes

$$\mathcal{L} = \bar{\psi} (i\gamma^\mu \partial_\mu) \psi - m\bar{\psi}\psi - (e\bar{\psi} \gamma^\mu \psi) A_\mu. \quad (1.11)$$

[†] The procedure of achieving local gauge invariance through the substitution of ∂_μ with D_μ is called *minimal coupling rule*.

As can be easily verified, this Lagrangian is indeed invariant under a local phase transformation. Yet, the modified Lagrangian in eq. (1.11) cannot be complete as it is still missing a free term for the field A_μ itself. For a vector field like A_μ , the Lagrangian describing the free case is the Proca Lagrangian

$$\mathcal{L}_{Proca} = \frac{-1}{16\pi} F^{\mu\nu} F_{\mu\nu} + \frac{1}{8\pi} m_A^2 A^\nu A_\nu, \quad (1.12)$$

where $F^{\mu\nu} \equiv (\partial^\mu A^\nu - \partial^\nu A^\mu)$ is the field strength tensor that is invariant under the transformation in eq. (1.9). Since $A^\nu A_\nu$ is not invariant under the same transformation, the only way to keep the full Lagrangian invariant under a local phase transformation is by requiring $m_A = 0$, i.e. the introduced gauge field A_μ has to be massless. This yields the full Lagrangian

$$\mathcal{L} = \bar{\psi} (i\gamma^\mu \partial_\mu) \psi - m\bar{\psi}\psi - \frac{1}{16\pi} F^{\mu\nu} F_{\mu\nu} - (e\bar{\psi}\gamma^\mu\psi) A_\mu, \quad (1.13)$$

which turns out to be the Lagrangian of quantum electrodynamics (QED). The introduced gauge field A^μ is thus nothing else but the electromagnetic potential with its associated particle, the photon. Thus, by forcing a global phase invariance to hold locally, a new massless gauge field has to be introduced in order for the Lagrangian to be invariant under local phase transformations. The new gauge field not only comes with its own kinetic term in the Lagrangian, but also introduces coupling to the fields already existing in the Lagrangian. In the above case of the Dirac Lagrangian, the requirement of local phase invariance produces all of quantum electrodynamics through the introduction of the massless photon field, interacting with charged particles.

As the global phase transformation in eq. (1.6) is part of the unitary group $U(1)$, the Lie group of all 1×1 matrices with $U^\dagger U = \mathbb{1}$, this symmetry is called $U(1)_{\text{em}}$ *gauge symmetry*[†]. But, as Yang and Mills have shown in 1954 [7], it is also perfectly possible to require a global phase invariance to hold locally in the case of the special unitary group $SU(n)$, the Lie group of $n \times n$ matrices with determinant 1. As it finally turns out, the SM is based upon a combination of three symmetry groups

$$SU(3)_C \times SU(2)_L \times U(1)_Y, \quad (1.14)$$

where $SU(3)_C$ generates quantum chromodynamics (QCD), i.e. the interaction of particles with colour charge through the exchange of gluons, and $SU(2)_L \times U(1)_Y$ describes the electroweak interaction. It is worth noting that the $U(1)_Y$ symmetry group present in the SM is not exactly the $U(1)_{\text{em}}$ symmetry group from QED, since they have different generators. Section 1.1.3 discusses this further.

In the electroweak interaction, the subscript L indicates that $SU(2)_L$ only couples to left-handed particles, while Y refers to the weak hypercharge, given by the Gell-Mann-

[†] Here, the subscript ‘em’ stands for electromagnetic and is used to distinguish $U(1)_{\text{em}}$ from $U(1)_Y$.

Table 1.1: Names, electric charges and masses (rounded to three significant digits if known to that precision) of all observed fermions in the SM. More details can be found in [8].

	generation	particle	electric charge [e]	mass
leptons	1	electron (e)	-1	511 keV
		electron neutrino (ν_e)	0	< 2 eV
	2	muon (μ)	-1	106 MeV
		muon neutrino (ν_μ)	0	< 0.19 MeV
	3	tau (τ)	-1	1.78 GeV
		tau neutrino (ν_τ)	0	< 18.2 MeV
quarks	1	up (u)	$\frac{2}{3}$	2.3 MeV
		down (d)	$-\frac{1}{3}$	4.8 MeV
	2	charm (c)	$\frac{2}{3}$	1.28 GeV
		strange (s)	$-\frac{1}{3}$	95 MeV
	3	top (t)	$\frac{2}{3}$	173 GeV
		bottom (b)	$-\frac{1}{3}$	4.18 GeV

Nishijima relation

$$Q = I_3 + \frac{1}{2}Y, \quad (1.15)$$

where Q is the electric charge and I_3 the third component of the weak isospin. Eventually, in the SM, all the fundamental interactions are generated through gauge symmetries.

1.1.3 Particle content

In the SM, particles are classified into two main categories, depending on whether they have integer or half-integer spin. Particles with half-integer spin follow Fermi-Dirac statistics and are called fermions. Since they are subject to the Pauli exclusion principle, they make up ordinary matter. Particles with integer spin follow the Bose-Einstein statistics and are called bosons. They are needed in order to mediate the fundamental interactions as fermions do not directly interact with each other. An overview of all particles in the SM is given in tables 1.1 and 1.2.

Fermions

Fermions are further divided into leptons and quarks that each come in three generations with increasing masses. Leptons form $SU(2)_L$ doublets consisting of an electrically charged lepton and a corresponding neutral neutrino. While the SM assumes neutrinos to be massless, the observation of neutrino oscillations [9] requires that at least two of them

Table 1.2: Names, electric charges and masses (rounded to three significant digits if known to that precision) of all observed bosons in the SM. More details can be found in [8].

particle	spin	electric charge [e]	mass
photon (γ)	1	0	0
gluon (g)	1	0	0
W^\pm	1	± 1	80.4 GeV
Z^0	1	0	91.2 GeV
Higgs boson (H)	0	0	125 GeV

are massive. By introducing neutrino masses[†], the oscillations can be explained with a lepton generation mixing, described by the Pontecorvo-Maki-Nakagawa-Sakata (PMNS) matrix [10]. As neutrinos only interact through the weak interaction, their experimental detection is inherently difficult. Quarks carry both colour charge and electric charge and form $SU(2)_L$ doublets of an up-type (u, c, t) and a down-type (d, s, b) quark. The coupling between the three quark generations through the weak interaction can be described by the Cabibbo-Kobayashi-Maskawa (CKM) matrix [11]. Since the SM is a relativistic quantum theory, each fermion has an anti-particle that has the same mass and spin, but inverted charge-like quantum numbers. In this work, the term ‘lepton’ refers only to electrons and muons, but not taus.

Bosons

Bosons are the force carrier particles that mediate the forces between the fermions. As described in section 1.1.2, each of the three symmetry groups in the SM is at the origin of one or more massless gauge bosons that couple to the conserved charge of the respective symmetry group they originate from.

The gauge theory associated with the $SU(3)_C$ symmetry group is quantum chromodynamics (QCD), describing the strong interaction. The gauge bosons of the strong interaction are the gluons (g), which couple only to particles with a colour charge. There are three types of colour charge: *red*, *green* and *blue* (and their respective anti-colour). Gluons themselves carry one unit of colour and one unit of anti-colour. Due to colour-confinement, colour charged particles like gluons and quarks cannot exist as free particles, instead they will always form colour-neutral bound states. Although, nine gluon states are possible, only eight of them are realized in nature: the singlet state $\frac{1}{\sqrt{3}}(|r\bar{r}\rangle + |g\bar{g}\rangle + |b\bar{b}\rangle)$ would be colour-neutral and allow long-range strong interactions, which have not been observed [4].

The remaining two symmetry groups $SU(2)_L \times U(1)_Y$ of the electroweak theory are not as straight-forward. Theoretically, $SU(2)_L$ manifests itself through the existence of three massless spin-1 gauge bosons W_μ^1 , W_μ^2 , and W_μ^3 , while $U(1)_Y$ causes the existence of

[†] Strictly speaking, introducing massive neutrinos is already an extension to the SM.

another massless spin-1 gauge boson B_μ . However, since the gauge bosons mediating the weak force observed in nature are not massless, the electroweak symmetry has to be broken. The mechanism allowing this spontaneous symmetry breaking of the $SU(2)_L \times U(1)_Y$ gauge symmetry into $U(1)_{\text{em}}$ and introducing heavy gauge bosons is called Higgs mechanism. It requires the introduction of a new complex scalar field, the Higgs field, with a non-zero vacuum expectation value (VEV) causing spontaneous symmetry breaking while giving rise to four Goldstone bosons[†]. Three of the Goldstone bosons are absorbed by the gauge bosons, that, in turn, gain a longitudinal polarization mode and become massive. Two of the three W_μ bosons form a linear combination producing the physical W^\pm bosons that couple to $SU(2)_L$ doublets,

$$W_\mu^\pm = \frac{1}{\sqrt{2}} (W_\mu^1 \mp i W_\mu^2). \quad (1.16)$$

The remaining W_μ^3 boson and the B_μ boson mix to form the photon A_μ and the massive Z_μ boson

$$A_\mu = B_\mu \cdot \cos \theta_W + W_\mu^3 \cdot \sin \theta_W, \quad (1.17)$$

$$Z_\mu = -B_\mu \cdot \sin \theta_W + W_\mu^3 \cdot \cos \theta_W, \quad (1.18)$$

where θ_W is the mixing angle, called Weinberg angle. While the photon couples to electric charges Q , the Z boson has a coupling proportional to $I_3 - Q \sin^2 \theta_W$. The remaining Goldstone boson manifests itself as an additional scalar boson, called the Higgs boson. It couples to the W^\pm and Z^0 bosons as well as to all the massive fermions due to the coupling terms being proportional to the fermion masses. With the discovery of the Higgs boson in 2012, all particles predicted by the SM have been experimentally detected.

1.2 Supersymmetry

The following section presents an introduction to the concept of supersymmetry (SUSY). It starts with a motivation of SUSY itself, followed by an introduction to the mathematical description and phenomenological consequences of a supersymmetric theory. A complete and detailed introduction to SUSY can be found in Ref. [14].

1.2.1 Limitations and open questions of the SM

Although the SM is a wildly successful theory able to describe and predict with extremely high precision the interactions between elementary particles, there are still phenomena in nature that cannot be suitably understood by the SM. Those limitations and open

[†] Goldstone's theorem [12, 13] dictates that the spontaneous breaking of a generic continuous symmetry causes the existence of as many massless spin-0 bosons as generators that have been broken.

questions of the SM are the reason for countless searches looking for new physics beyond the SM (BSM). A class of BSM theories used in this work is supersymmetry.

Dark Matter

Multiple astrophysical observations hint to additional sources of gravity apart from the ordinary visible matter described by the SM. One example of such an astrophysical observation is the deviation in the rotation curves of galaxies. By observing stars in the galaxies, the distribution of the orbital velocity with respect to their distance from the galactic centre can be measured. When comparing the observed rotation curves with those that would be expected based on the visible mass distribution in the galaxies, a significant disagreement is seen. Objects on the verge of galaxies tend to rotate much faster than expected, hinting at the presence of an additional source of gravity [15].

Another very compelling evidence for the existence of dark matter is the bullet cluster, consisting of two colliding galaxy clusters. The visible mass of the colliding clusters is mostly composed of hot gas interacting electromagnetically. During the collision, the gases interact with each other and are significantly slowed down and distorted. The dark matter, however, making up most of the clusters' total masses and showing very little interaction, survives the collision without much distortion. This can be experimentally verified by observing background objects where the bullet cluster acts as gravitational lens, showing that most of the clusters' mass must have passed each other without significant interaction [16].

While ordinary visible matter makes up only 4.9% of the energy density in the universe, dark matter represents 26.8% of the energy density in our universet[†] [18]. It is therefore particularly interesting to develop theories that provide candidates for dark matter. One very popular possibility is the construction of dark matter through weakly interacting massive particles (WIMPs). In many supersymmetric theories, the lightest supersymmetric particle (LSP) is stable and neutral and thus constitutes an ideal candidate for dark matter.

The Hierarchy Problem

Due to its deficiencies, it is clear that the SM is not a complete theory of nature, but rather a low-energy approximation to a more fundamental theory. As such, the SM is at least valid up to the currently probed energies of $\mathcal{O}(\text{TeV})$. At no later than the Planck scale $\mathcal{O}(10^{15} \text{ TeV})$, the scale where quantum gravitational effects become important [14], a new theoretical framework is necessary and new physics is expected to appear. However, the mere fact that the two scales are roughly 15 orders of magnitude in energy apart

[†] The remaining 68.3% are occupied by *Dark Energy*, whose nature is yet another open question. More information is available in e.g. Ref. [17].

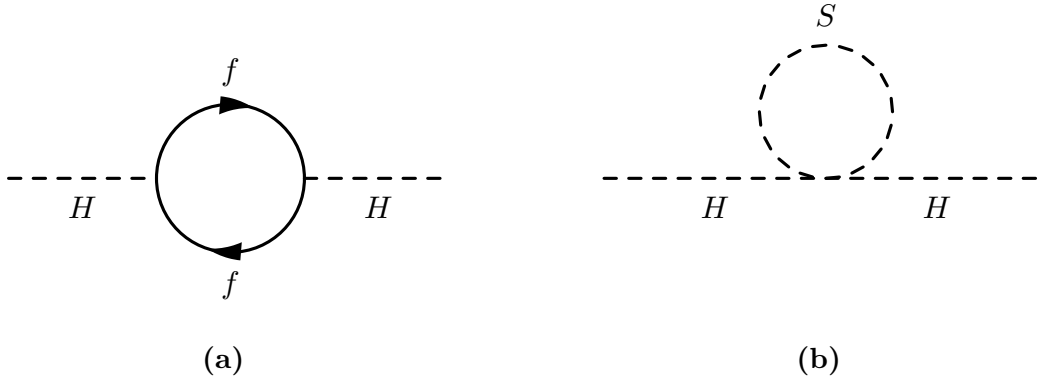


Figure 1.1: A massive fermion (a) and a hypothetical massive scalar particle (b) coupling to the Higgs boson.

from each other is already a strong indication that new physics can be expected to exist already far below the Planck scale.

The peculiarities introduced by the sheer difference between the two scales becomes much more apparent when considering the Higgs mass. Since the Higgs boson is a scalar particle, its mass is not protected from high quantum corrections through chiral symmetry. The coupling of the Higgs field to a fermion f with mass m_f as in fig. 1.1(a) yields a one-loop correction to the Higgs squared mass given by

$$\Delta m_H^2 = -\frac{|\lambda_f|^2}{8\pi^2} \Lambda_{UV}^2 + \dots \quad (1.19)$$

Similarly, a one-loop correction due to the coupling to a hypothetical heavy complex scalar particle S with mass m_S as in fig. 1.1(b) is given by

$$\Delta m_H^2 = \frac{\lambda_S}{16\pi^2} \left[\Lambda_{UV}^2 + 2m_S^2 \log(\Lambda_{UV}/m_S) + \dots \right]. \quad (1.20)$$

In eqs. (1.19) and (1.20), Λ_{UV} refers to a cut-off scale at which the computation of the loop corrections are cut off. This is necessary because the corrections are quadratic and not logarithmic and therefore divergent. If Λ_{UV} is taken to be the Planck scale, where new physics is expected to appear, then the corrections to the Higgs boson squared mass can become many orders of magnitude larger than the measured Higgs mass itself. Thus the natural scale of the Higgs boson mass is the Planck scale, and not the electroweak scale. In order to get to the observed value of roughly 125 GeV, the bare Higgs mass parameter has to be tuned in such a way that it cancels precisely with the large corrections. This extreme fine-tuning and sensitivity to physics at arbitrarily high scales is considered to be unnatural.

In SUSY, the Higgs boson mass is automatically protected from the high contributions to Δm_H^2 by introducing, for each fermion in the SM, two real scalars with $\lambda_S = |\lambda_f|^2$. Since the fermion loop and boson loop corrections in eqs. (1.19) and (1.20) enter with

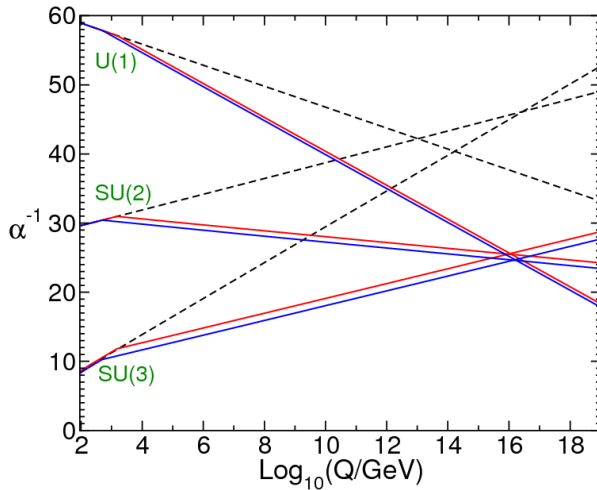


Figure 1.2: The running of the electroweak and strong coupling constants in the SM (dashed lines) and in the MSSM (solid lines). Figure taken from [19].

a relative minus sign, this introduced symmetry between fermions and bosons exactly cancels the high corrections, making it possible for the observed Higgs mass to be at the electroweak scale without the need of unnatural fine tuning.

Unification of forces

After the successful unification of the electromagnetic and the weak force to the electroweak force, a valid question is if and how the SM could be extended to a grand unified theory (GUT), a theory where the strong and the electroweak force are unified in one single interaction. In a GUT, the symmetry groups of the SM are embedded in a single symmetry group that is a superset of $SU(3)_C \times SU(2)_L \times U(1)_Y$ with the advantage that all the interactions would be described by one single symmetry group with a single coupling constant. Accordingly, at the unification scale, the three running coupling constants of the SM would combine into the single coupling constant of the GUT. Although the inverse of the coupling constants of the SM run towards each other, they do not exactly meet in a single point without new physics altering the running of the coupling at some scale beyond the electroweak scale. This behaviour is illustrated in fig. 1.2. In the Minimal Supersymmetric Standard Model (MSSM) with new particles at the TeV scale, exact unification is possible at roughly 10^{16} GeV, making SUSY an ideal candidate for enabling the extension of the SM to a GUT.

1.2.2 Mathematical description

A supersymmetry transformation converts a fermionic state $|f\rangle$ into a bosonic state $|b\rangle$, and vice versa. The operator Q necessary to achieve such a transformation is an

anti-commuting spinor with

$$Q |b\rangle = |f\rangle, \quad (1.21)$$

$$Q |f\rangle = |b\rangle. \quad (1.22)$$

Since Q is a spinor, its hermitian conjugate Q^\dagger is also a symmetry operator. As both Q and Q^\dagger are fermionic operators, they carry a spin of $\frac{1}{2}$, meaning that supersymmetry must be a spacetime symmetry, i.e. a Poincaré symmetry. In 1967, Coleman and Mandula have shown with their ‘no go’ theorem [20], that the symmetry group of a consistent spacetime quantum field theory must be the direct product of the internal symmetry group and the Poincaré group. This would in principle rule out the possibility of supersymmetry if it were not for the Haag-Lopuszanski-Sohnius extension [21], stating that the only non-trivial combination of an internal and spacetime symmetry is to use Lie superalgebra (as opposed to Lie algebra) with fermionic generators [22]. Thus, it is not a coincidence that the symmetry operator in SUSY is a spinor, it is the only possibility. In order to obey the Coleman-Mandula theorem and simultaneously allow for parity-violating interactions (as have been observed in the SM), the SUSY generators must satisfy the following anti-commutation and commutation relations

$$\{Q, Q^\dagger\} = P^\mu, \quad (1.23)$$

$$\{Q, Q\} = \{Q^\dagger, Q^\dagger\} = 0, \quad (1.24)$$

$$[P^\mu, Q] = [P^\mu, Q^\dagger] = 0, \quad (1.25)$$

where P^μ is the four-momentum generator of spacetime translations [14]. The irreducible representations of the supersymmetry algebra are called *supermultiplets* and each contain bosonic and fermionic states. In the Minimal Supersymmetric Standard Model (MSSM), the smallest possible supersymmetric extension of the SM, the supermultiplets each contain a SM particle as well as its *superpartner*. As can be seen in eq. (1.25), both SUSY generators commute with spacetime translations P^μ and hence also with the squared mass operator $-P^2$. Therefore, both single-particle states of a supermultiplet have the same eigenvalues under $-P^2$, meaning that $m_f = m_b$. Furthermore, the SUSY generators also commute with the gauge transformation generators, thus supersymmetric particles must have the same electric charge, weak isospin and colour charge as their SM partner, living in the same supermultiplet.

1.2.3 Supersymmetry breaking

As set out in section 1.2.2, supersymmetric particles have the same masses as their SM partners. If this were really the case, then the detection of supersymmetric particles (*sparticles*) would have been straight-forward, as they would live in the same energy range as the SM particles. Clearly, SUSY has to be a broken symmetry causing the superpartners to have much higher masses than their SM counterparts. However, if broken

Table 1.3: Chiral supermultiplets in the MSSM. The spin-0 fields are complex scalars and the spin-1/2 fields are left-handed Weyl fermions. Taken from [14].

Names		spin 0	spin 1/2	$SU(3)_C, SU(2)_L, U(1)_Y$
squarks, quarks 3 families	Q	$(\tilde{u}_L \quad \tilde{d}_L)$	$(u_L \quad d_L)$	$(\mathbf{3}, \mathbf{2}, \frac{1}{6})$
	\bar{u}	\tilde{u}_R^*	u_R	$(\bar{\mathbf{3}}, \mathbf{1}, -\frac{2}{3})$
	\bar{d}	\tilde{d}_R^*	d_R	$(\bar{\mathbf{3}}, \mathbf{1}, \frac{1}{3})$
sleptons, leptons 3 families	L	$(\tilde{\nu} \quad \tilde{e}_L)$	$(\nu \quad e_L)$	$(\mathbf{1}, \mathbf{2}, -\frac{1}{2})$
	\bar{e}	\tilde{e}_R^*	e_R	$(\mathbf{1}, \mathbf{1}, 1)$
Higgs, higgsinos	H_u	$(H_u^+ \quad H_u^0)$	$(\tilde{H}_u^+ \quad \tilde{H}_u^0)$	$(\mathbf{1}, \mathbf{2}, \frac{1}{2})$
	H_d	$(H_d^0 \quad H_d^-)$	$(\tilde{H}_d^0 \quad \tilde{H}_d^-)$	$(\mathbf{1}, \mathbf{2}, -\frac{1}{2})$

SUSY is still to provide a solution to the hierarchy problem through the cancellation of the quadratic divergences in the Higgs boson squared mass, then the symmetry breaking needs to be of a special form. In the MSSM, the supersymmetric theory considered in this work, this is achieved through *soft* SUSY breaking such that the effective Lagrangian of the MSSM can be written as

$$\mathcal{L} = \mathcal{L}_{\text{SUSY}} + \mathcal{L}_{\text{soft}}. \quad (1.26)$$

Here, $\mathcal{L}_{\text{SUSY}}$ is supersymmetry invariant and contains all the couplings while $\mathcal{L}_{\text{soft}}$ breaks supersymmetry [14]. This procedure allows for supersymmetric particles with masses in the TeV scale. Therefore, SUSY could potentially be discovered at the CERN Large Hadron Collider.

1.2.4 Particle content in the MSSM

The supermultiplets in the MSSM contain the same number of bosonic degrees of freedom n_b and fermionic degrees of freedom n_f . In total, there are two main categories of supermultiplets in the MSSM, chiral and gauge supermultiplets. The nomenclature of the sparticles is as follows. On the one hand, the scalar partners of SM fermions are constructed by prepending an ‘s’ to their name (e.g. *selectron*, *stop*, ...). On the other hand, the spin-1/2 partners of the SM bosons are constructed by appending ‘-ino’ to their name (e.g. *Wino*, *Higgsino*, ...). In general, the symbols for sparticles are the same as for their SM counterparts, but with an additional tilde (e.g. \tilde{e} , \tilde{u} , \tilde{g} , ...).

Chiral supermultiplets are the simplest supermultiplets for which $n_b = n_f$ holds. They consist of a Weyl fermion with two spin helicity states and two real scalar fields with one degree of freedom each. The SM quarks and leptons are part of a chiral supermultiplet and their spin-0 partners are scalar quarks (\tilde{q}) and scalar leptons ($\tilde{\ell}$). The left- and right-

Table 1.4: Gauge supermultiplets in the MSSM. Taken from [14].

Names	spin 1/2	spin 1	$SU(3)_C, SU(2)_L, U(1)_Y$
gluino, gluon	\tilde{g}	g	(8, 1, 0)
winos, W bosons	$\tilde{W}^\pm \tilde{W}^0$	$W^\pm W^0$	(1, 3, 0)
bino, B boson	\tilde{B}^0	B^0	(1, 1, 0)

handed versions of the quarks and leptons are separate supermultiplets and therefore have their own superpartners (e.g. \tilde{e}_L and \tilde{e}_R). The subscripts L and R used to highlight this separation are obviously only referencing to the helicity state of the SM particle and not of the superpartner[†]. The particles in the chiral supermultiplets are summarized in table 1.3.

The next-simplest supermultiplets for which $n_b = n_f$ holds are the gauge supermultiplets. They contain a massless[§] spin-1 gauge boson with two helicity states and a massless spin-1/2 Weyl fermion with two helicity states. The SM gauge bosons (W^\pm , W and B) are part of a gauge supermultiplet and their spin-1/2 superpartners are the *gauginos*. Table 1.4 summarizes the particles in the gauge supermultiplets.

The Higgs boson, being a scalar particle, must live in a chiral supermultiplet. However, in order to avoid gauge anomalies, the MSSM actually needs two Higgs supermultiplets, one with $Y = 1/2$ and one with $Y = -1/2$. The two $SU(2)_L$ doublets with $Y = \pm 1/2$ are called H_u and H_d , respectively. In total, the Higgs doublets lead to eight degrees of freedom, three of which are absorbed in order to generate the gauge boson masses in the electroweak symmetry breaking. The remaining five degrees of freedom lead to five different Higgs bosons, two CP even states h^0 and H^0 , one CP odd state A^0 and two charged bosons H^\pm . The state h^0 is considered to be the SM Higgs boson.

Additionally, the MSSM predicts particles that have no direct equivalent in the SM. After electroweak symmetry breaking, the electroweak gauginos and higgsinos mix to form mass eigenstates that are identified with new particles. The two charged winos and the two charged higgsinos form two charged mass eigenstates called *charginos* ($\tilde{\chi}_1^\pm, \tilde{\chi}_2^\pm$), while the neutral wino and bino mix with the remaining neutral higgsinos to form four neutral mass eigenstates called *neutralinos* ($\tilde{\chi}_1^0, \tilde{\chi}_2^0, \tilde{\chi}_3^0$ and $\tilde{\chi}_4^0$, ordered with increasing masses).

1.2.5 R-parity

If the superpotential is to be renormalisable and follow the gauge-invariance of the SM, then its most general form allows for terms that violate the baryon number B or the lepton number L . Processes that violate the baryon or the lepton number have not yet

[†] Squarks and sleptons are scalar and therefore do not have different helicity eigenstates.

[§] Massless before the respective gauge symmetry is broken.

been observed in the SM, causing the violating terms in the superpotential to be heavily constrained. One very prominent constraint is the non-observation of proton decays by the Super-Kamiokande Experiment, determining the lower limit for the decay time of the proton into lepton+meson final states to be above 10^{32} years [23]. In order to ensure that the B - and L -violating terms in the general form of the superpotential do not appear in the MSSM, a new conserved quantity, called R-parity, is introduced

$$P_R = (-1)^{3(B-L)+2s}. \quad (1.27)$$

Here, s is the spin of the particle the R-parity is to be computed of. As can be easily verified, $P_R = +1$ for SM particles and $P_R = -1$ for SUSY particles. Apart from suppressing the L- and B-violating terms in the MSSM Lagrangian, this multiplicative quantity introduces some interesting phenomenological consequences. SUSY particles can only be produced in pairs and each vertex in the MSSM must have an even number of SUSY particles. Furthermore, the LSP, being the lightest supersymmetric particle, has to be stable. Considering that the LSP only interacts weakly, this makes it an ideal candidate for dark matter.

1.2.6 Simplified models

In searches for new physics at the Large Hadron Collider, it is common to use simplified models [24, 25] as a way to reduce the parameter space to a manageable level. This circumvents the issue of having to search for SUSY in a vast parameter space where a lot of parameters may have only small effects on observables. In the simplified models appearing in this work, all branching fractions are considered to be at 100% and all supersymmetric particles not explicitly participating in the decay chain are set to be kinematically inaccessible. The masses of the produced SUSY particles in each model are free parameters that need to be scanned. It is therefore common to sort the scanned signal models in *signal grids* where the mass parameters each occupy an axis. As each scanned signal model occupies a single grid point corresponding to its specific combination of SUSY particle masses in the grid, the term *signal point* is in the following often used to refer to a single signal model with a given set of mass parameters.

The simplified model primarily used within this work is depicted in fig. 1.3(a). In the following, it is referred to as the *WW model*. It considers the electroweak pair production of two lightest charginos $\tilde{\chi}_1^\pm$ that each decay into a W boson and a lightest neutralino $\tilde{\chi}_1^0$. One of the two W bosons is required to further decay leptonically, the other one hadronically. As described in section 1.2.5, due to R-parity conservation, the produced lightest neutralinos are stable and therefore escape the detector without interaction, producing missing transverse energy, a quantity described in detail in section 4.3.6. As this rather generic simplified model easily produces a final state that is of interest for an analysis requiring an isolated lepton (called *1-lepton analysis* and further described in chapter 4), one main topic discussed in this work is the evaluation of the sensitivity of this analysis to the *WW* model.

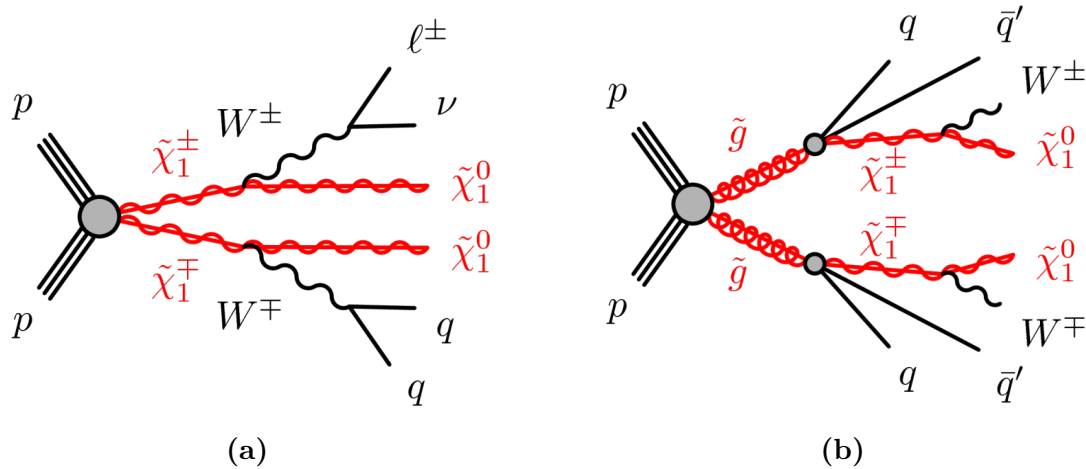


Figure 1.3: Simplified models considered in this work.

A second model of special interest for this work is the model pictured in fig. 1.3(b). It has already been investigated by the 1-lepton analysis [26] and, in this work, is used to validate a procedure developed for the analysis in order to broaden the scope of the search for the phenomenological MSSM, a class of supersymmetric models with 19 parameters (further explained in section 1.2.7). Details and results of these studies are discussed in chapter 7. The model considers the strong pair production of two gluons that each decay via an intermediate $\tilde{\chi}_1^\pm$ to the $\tilde{\chi}_1^0$. In each of the two decay branches, two quarks and a W boson appear. If one of the W bosons decays leptonically, then this simplified model can again produce a final state with an isolated lepton, multiple jets and missing transverse energy. The model is defined by three parameters: the gluino mass, the LSP mass and the ratio of mass differences between the chargino and the LSP and the gluino and the LSP, $x = \frac{m(\tilde{\chi}_1^\pm) - m(\tilde{\chi}_1^0)}{m(\tilde{g}) - m(\tilde{\chi}_1^0)}$. In order to allow for varying values for all three parameters, two separate signal grids are defined, one with $x = \frac{1}{2}$ and one with varying x but $m(\tilde{\chi}_1^0)$ fixed to 60 GeV. Due to its decay chain with production of an intermediate $\tilde{\chi}_1^\pm$, the model will in the following be referred to as *gluino one-step* model.

1.2.7 The phenomenological MSSM

Since searches for SUSY have not yet found supersymmetric particles, their results are used to constrain the model space in which supersymmetry can be realised. In SUSY, this is usually done by setting lower limits to the masses of the sparticles involved in the respective search. Within the ATLAS Collaboration, there are a multitude of different SUSY searches, each setting lower limits. Naturally, it is of particular interest to be able to state a combined performance and sensitivity to SUSY. This would also allow to identify regions in the parameter space without any (or only poor) sensitivity to supersymmetric models, yielding additional input to the design of analyses.

Although the use of simplified models is often a very useful method to capture a wide range of different phenomena, this method fails to capture more complex effects resulting from a larger set of parameters and the influence of other production and decay processes.

In order to derive a combined sensitivity to SUSY as well as combined constraints to the model space in SUSY, it is therefore necessary to do a systematic scan of a set of parameters properly describing the entire model space. Although the MSSM is a minimal supersymmetric theory, it still has a total of 105 free parameters, which is too much to be scanned exhaustively and compared to data. By applying a series of constraints designed to discard models that are not phenomenologically viable but select those that are more realistic, the set of free parameters can be reduced to 19. This is called the phenomenological MSSM (pMSSM).

The reduction of parameters is obtained by applying the following constraints on the MSSM [27]:

- The parameters arising from soft SUSY breaking must be real, such that no new source of CP violation appears.
- No new source of additional flavour-changing neutral currents (FCNC).
- The first and second generation sfermions must have degenerate masses.

These three constraints, together with the electroweak symmetry breaking conditions, reduce the number of parameters to the following 19:

- $\tan \beta$: the ratio of the VEVs of the two Higgs fields.
- M_A : the mass of the CP odd Higgs boson.
- μ : the Higgs-higgsino mass parameter.
- M_1, M_2, M_3 : the bino, wino and gluino mass parameters.
- $m_{\tilde{q}}, m_{\tilde{u}_R}, m_{\tilde{d}_R}, m_{\tilde{\ell}}, m_{\tilde{e}_R}$: the masses of the first and second generation sfermions.
- $m_{\tilde{Q}}, m_{\tilde{t}_R}, m_{\tilde{b}_R}, m_{\tilde{L}}, m_{\tilde{\tau}_R}$: the masses of the third generation sfermions.
- A_t, A_b, A_τ : the trilinear couplings of the third generation sfermions.

The above list of parameters and more information on the pMSSM itself can be found in Ref. [27]. With the reduced number of parameters, it is possible to perform exhaustive scans of the pMSSM parameter space and compare the results with data from ATLAS. The results from a Run-1 pMSSM scan with ATLAS data are available in Ref. [28].

Chapter 2

The LHC and ATLAS

One of Europe's first joint ventures in science [29], CERN (Conseil Européen pour la Recherche Nucléaire) is one of the largest research centres in the world. Located at the Franco-Swiss border near Geneva, it was founded in 1954 and, by now, counts 22 member states [29]. CERN's main research area is particle physics, which is why the organization operates a multitude of different particle accelerators and detectors.

2.1 The Large Hadron Collider

The Large Hadron Collider (LHC) [30] is the largest particle accelerator situated at CERN. The tunnel housing the LHC was previously built for the Large Electron Positron Collider (LEP) and lies between 175 m (under the Jura) and 50 m (close to Lake Geneva) below the surface, resulting in a tilt of about 1.4%. With a circumference of 26.7 km [30], the LHC is the largest accelerator on Earth. Due to the geometry of the tunnel, the accelerator is composed of eight arcs and eight straight sections. The arcs are filled with a total of 1232 [30] dipole magnets responsible for keeping the particle beam on their trajectory around the ring. These dipole magnets are the limiting factor of the maximal centre-of-mass energy \sqrt{s} of the LHC. In order to reach the design energy $\sqrt{s} = 14 \text{ TeV}$, i.e. 7 TeV per beam, the magnets have to create a magnetic field with a strength of 8.3 T [31]. Such high magnetic fields can only be reached by using superconductive magnets that need to be operated at a temperature of 1.9 K [31]. Together with the quadrupole magnets used for beam-shaping, as well as other magnets used for beam-injection and -dumping, the LHC contains a total of 9593 magnets [30]. The eight straight sections each serve as insertion region (IR) either for particle detectors or for machine hardware of the collider itself. The IRs are labelled clockwise, with IR 1 being the closest one to the CERN Meyrin site. IR 4 contains a total of 16 radio-frequency (RF) cavities, responsible for accelerating the particles. Due to the RF cavities, the accelerated particles are grouped in packages called *bunches*, with a length of ca. 7.5 m (or 25 ns) each. Each beam contains a total of 2808 bunches as design value [30]. The counter-rotating beams are brought

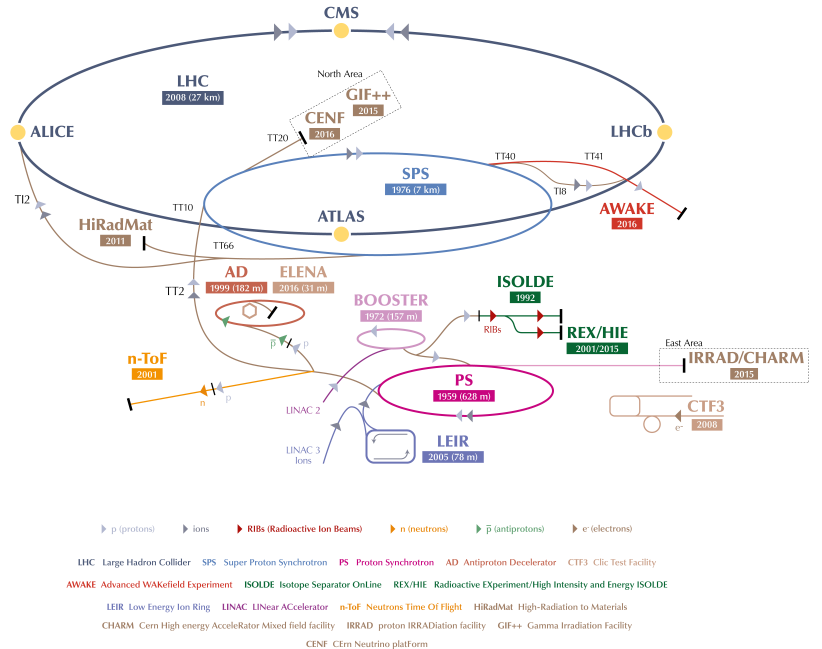


Figure 2.1: CERN accelerator complex as of 2018 [34].

to collision at four of the eight IRs, called interaction points (IPs). IP 1 houses the ATLAS (A Toroidal LHC ApparatuS) detector, while IP 5, located on the opposite site of the ring, is where the Compact Muon Solenoid (CMS) experiment is situated. The two remaining IPs 2 and 8 next to ATLAS host the Large Hadron Collider beauty (LHCb) experiment and A Large Ion Collider Experiment (ALICE). While ATLAS and CMS are general-purpose detectors, LHCb is specialized on b-physics and ALICE on heavy ion physics. Apart from the four main experiments, there are three more making use of the proton or ion beams of the LHC: the Large Hadron Collider forward (LHCf) experiment, the Total Elastic and diffractive cross section measurement (TOTEM) and the Monopole and Exotics Detector at the LHC (MoEDAL).

Before being injected into the LHC, the particles are pre-accelerated by CERN's accelerator complex, pictured in fig. 2.1. The particles start at the linear accelerator 2 (LINAC2), pass through the Booster, then are further accelerated in the Proton Synchrotron (PS), followed by the Super Proton Synchrotron (SPS) before finally reaching the LHC with an energy of 450 GeV. The LHC is responsible for the last acceleration step to the nominal beam energy. In its first proton-proton run (Run-1), the LHC reached a beam energy of 3.5 TeV (2010-2011) and 4 TeV (2012) [32]. After a two year long shut down phase used for maintenance and upgrades, the second run of proton-proton collisions (Run-2) started at 6.5 TeV beam energy ($\sqrt{s} = 13$ TeV) in 2015 [33], which is just short of the design centre-of-mass energy of $\sqrt{s} = 14$ TeV [30].

2.2 The ATLAS Experiment

The ATLAS detector is one of two general-purpose detectors at the LHC. Located at IP 1, it is 44 m long and 25 m high and sits in a cavern roughly 100 m below the surface. A detailed description off the ATLAS detector can be found in Ref. [35].

2.2.1 Coordinate System

In order to properly describe events in the ATLAS detector, a suitable coordinate system is needed. The right-handed coordinate system [36] has the nominal interaction point as its origin. The beam line is used to define the z -axis, the positive x -axis points towards the centre of the LHC ring and the positive y -axis is defined to point straight upwards. In the x - y -plane, called the transverse plane, the azimuthal angle ϕ is the angle around the beam axis while the polar angle θ is measured from the beam axis. The rapidity y [37] is defined to be

$$y = \frac{1}{2} \ln \left(\frac{E + p_z}{E - p_z} \right). \quad (2.1)$$

Since differences in the rapidity are invariant under Lorentz boosts in the z -direction, y is preferred over the polar angle θ .

The pseudorapidity [37] is the high-energy limit of the rapidity, only valid for $p \gg m$ and $\theta \gg \frac{1}{\gamma}$ and defined as

$$\eta = -\ln \tan \frac{\theta}{2}. \quad (2.2)$$

Compared to the rapidity, the pseudorapidity has the advantage of not depending on the energy and momentum calibration of the detected objects. Additionally, it gives a direct correspondence to the polar angle θ .

The distance between two objects is given by

$$\Delta R = \sqrt{(\Delta\eta)^2 + (\Delta\phi)^2}. \quad (2.3)$$

The longitudinal momentum of the partons composing the colliding hadrons is only known by means of parton distribution functions (PDFs), stating the probabilities of the partons to have a certain energy in the direction of the beam. Therefore, the total longitudinal energy in each collision is not exactly known, making it difficult to use physics quantities in the z -direction. In the x - y plane, however, momentum conservation can be easily applied, which is why mainly transverse physics quantities are used, indicated by a subscript ‘T’, e.g. E_T or p_T .

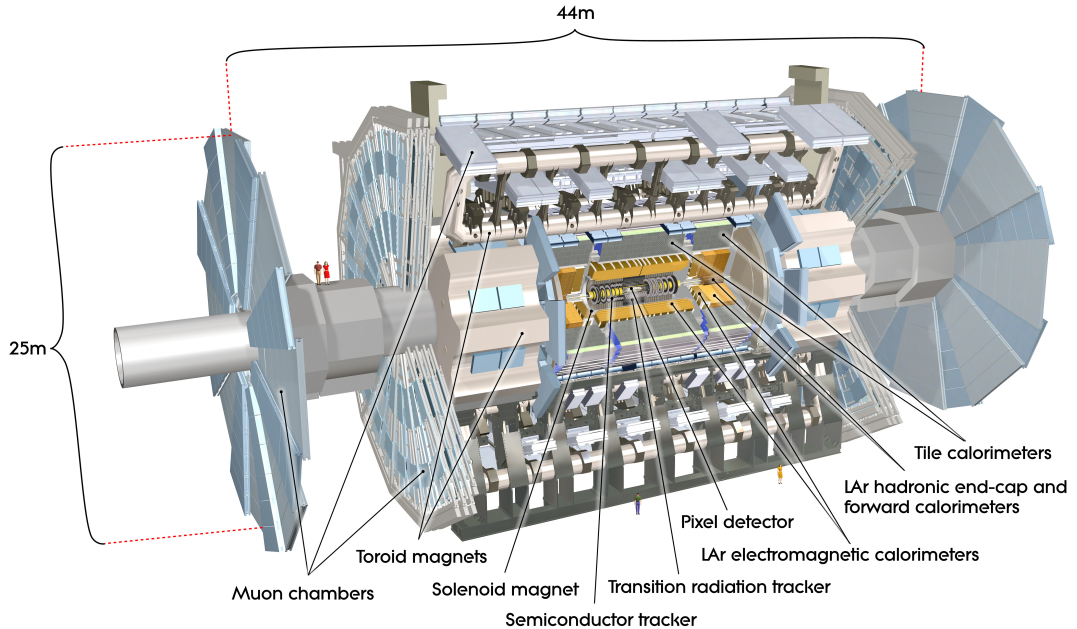


Figure 2.2: Computer generated picture of the ATLAS detector, giving an overview on the various subsystems [38].

2.2.2 Subdetectors

The ATLAS detector has a toroidal symmetry and is built of multiple subdetector systems [35]. Most of the subdetectors are built following the toroidal symmetry of ATLAS. In general, they have a central *barrel* part, designed to detect particles with relatively small $|\eta|$, complemented by two disk-shaped *end caps* that detect particles travelling close to the beam pipe with high $|\eta|$. A computer generated picture of the detector is shown in fig. 2.2.

Inner detector

The inner detector (ID) is the subdetector closest to the beam pipe. It consists of three different detector systems and is embedded in a 2 T solenoid magnetic field [35]. The magnetic field causes the tracks of charged particles to be bent in the transverse plane through the Lorentz force. This can be used to determine the momentum and charge sign of the detected particle.

The innermost layer of the ID is composed of silicon pixel detectors. Originally the pixel detector consisted of three layers specifically built to withstand the high-radiation environment close to the beam pipe, while being able to deliver the high spatial resolution necessary for a reliable vertex identification. In order to increase redundancy and reliability in even higher radiation environments caused by higher luminosity, a new innermost pixel

layer, called Insertable B-Layer (IBL) [39] was inserted before the start of Run-2 [40]. The pixel detector provides a spatial resolution in $r - \phi$ (z) direction of 10 (115) μm [35]. The second subsystem of the ID, the silicon strip trackers (SCT) provide an additional source of particle tracking with a spatial resolution of 17 (580) in $r - \phi$ (z) direction [35]. Similar to the pixel detector, the SCT provides tracking information up to $|\eta| < 2.5$ [35]. The third and largest of the ID subsystems is the transition radiation tracker (TRT), using drift tubes to provide particle tracking information. The drift tubes have a diameter of 4 mm [35] and are orientated parallel to the beam pipe. Filled with a gas mixture, the tubes can detect transition radiation photons emitted by traversing particles. This is also used to provide additional electron identification. The TRT covers a range up to $|\eta| < 2.0$ [35].

Calorimeters

Energy measurements in ATLAS are done with calorimeters. Since they are designed to fully absorb the particles, the calorimeters are located around the tracking system of the inner detector. In the ATLAS detector, there are two types of calorimeters, an electromagnetic calorimeter (ECal) and a hadronic calorimeter (HCal). Both calorimeters are sampling calorimeters, consisting of alternating layers of active and absorbing material. The absorbing material interacts with the traversing particles and causes them to deposit their energy by creating showers of particles. The active layers are then used to record the shape and intensity of the produced showers.

The ECal uses liquid argon (LAr) as active material and accordion-shaped lead plates as absorber. Located next to the inner detector, the ECal is responsible for measuring the energies of electromagnetically interacting particles. It has a thickness of > 22 radiation lengths[†] in the barrel and > 24 radiation lengths in the end-cap [35].

The HCal in the barrel uses scintillating tiles (Tile calorimeter) as active material and lead absorber plates. In the end-cap region, the HCal uses LAr as active material and copper as absorber.

Together with the LAr forward calorimeters, the calorimeter system in ATLAS provides energy measurements up to $|\eta| < 4.9$ [35].

Muon spectrometers

Muons are minimally ionizing particles and pass through the calorimeter system without losing much energy. Immersed in a toroidal magnetic field, the muon spectrometers (MS) form the outermost layer of the ATLAS detector and allow a measurement of the muon momentum that is independent from the measurement of the inner detector.

[†] The radiation length is a characteristic of a material and describes the length after which the energy of a traversing particle has decreased to $1/e$ of its initial energy due to radiation losses.

The muon spectrometers consist of four different detector types. Most of the precision tracking information is obtained with Monitored Drift Tube (MDT) chambers with an average precision of $35\text{ }\mu\text{m}$ per chamber [35]. In the innermost layer of the forward region $2.0 < \eta < 2.7$, Cathode Strip Chambers (CSC), multi-wire proportional chambers, are used. The muon trigger system relies on Resistive Plate Chambers (RPCs) in the barrel region and Thin Gap Chambers (TGCs) in the end-caps.

2.2.3 Trigger system

With a bunch spacing of 25 ns and up to 10^{11} protons in a single bunch, the event rates in ATLAS can get as high as 40 million events per second [35]. With a mean event size of approximately 1.3 MB [35], this equals a data volume of up to 50 TB per second, orders of magnitude more than any database in the world could write to tape, and much higher than any detector technology would be able to properly read out. In order to keep the amount of data written to tape at a manageable level and select only events containing potentially interesting physics, ATLAS employs a trigger system composed of a hardware-based first level trigger (L1) and a software-based High-Level-Trigger (HLT) [41]. The L1 trigger reduces the event rate from to about 100 kHz, based on muon spectrometer and calorimeter information. In order to achieve this event rate reduction, the L1 trigger has to make a decision within 2.5 μs . The HLT uses full granularity detector information in order to run reconstruction algorithms. With a processing time of 200 ms per event, the HLT reduces the event rate from 100 kHz to approximately 1 kHz. At this reduced rate, events can be written to permanent storage.

Chapter 3

Data and Monte Carlo Simulation

3.1 Data

The number of events recorded by the ATLAS detector is usually expressed by the integrated luminosity \mathcal{L} through

$$N = \sigma \mathcal{L} = \sigma \int L dt, \quad (3.1)$$

where N is the number of events, σ is the total cross section of the studied processes and L is the instantaneous luminosity of the LHC at IP 1 [31]. The instantaneous luminosity is given by

$$L = \frac{N_b^2 n_b f_{\text{rev}} \gamma_r}{4\pi \epsilon_n \beta^*} F, \quad (3.2)$$

where N_b is the number of particles per bunch, n_b the number of bunches in each beam, f_{rev} the collision frequency, γ_r the relativistic Lorentz factor, ϵ_n the normalized transverse beam emittance and β^* the beta function at the collision point. The factor F is a geometric factor indicating the luminosity reduction due to the crossing angle at the interaction point. The design peak instantaneous luminosity at IP 1 (ATLAS) and IP 5 (CMS) for proton-proton collisions is $L = 10^{34} \text{ cm}^{-2}\text{s}^{-1}$ [31]. Figure 3.1 summarises the peak instantaneous luminosities per fill of the LHC during data taking in 2015 and 2016.

Part of the studies presented in this work uses data from proton-proton collisions recorded by ATLAS throughout 2015 and 2016 at $\sqrt{s} = 13 \text{ TeV}$. In total, the data that is used corresponds to an integrated luminosity of $\mathcal{L} = 36.1 \text{ fb}^{-1}$.

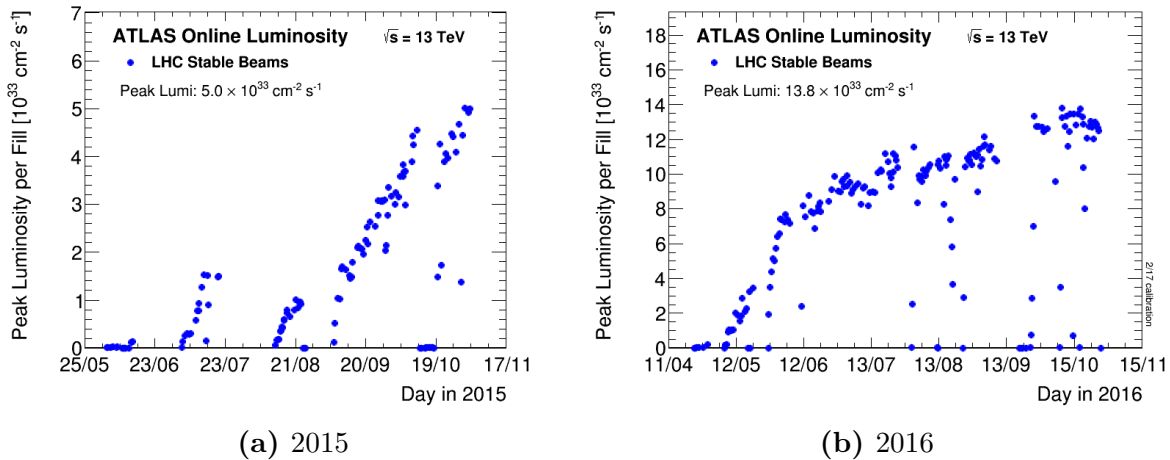


Figure 3.1: Peak instantaneous luminosities per fill during 2015 and 2016 data taking. Taken from [33].

3.2 Monte Carlo simulation

Monte Carlo (MC) simulations play a crucial role in high energy physics analyses. MC simulations are computational algorithms that use repeated random sampling to solve problems, often the estimation of multi-dimensional integrals for which an analytic answer is not known [42]. As, in principle, this approach can be used for any problem that has a probabilistic interpretation, it is especially suitable for particle physics where many aspects are inherently connected to probability distributions. Here, MC simulations are used to estimate the expected events of SM processes and predict the events of physics beyond the SM in a given phase space.

The generation of a simulated proton-proton collision at the LHC with a general-purpose MC generator can be divided in the following steps [43]:

- i. Hard scattering
 - ii. Parton shower
 - iii. Hadronisation
 - iv. Underlying event
 - v. Unstable particle decays

The *hard scattering* simulates the process with the highest momentum transfer in an event. Since incoming partons can be described with parton distribution functions (PDFs), the probabilistic distribution of the outgoing partons can be computed with perturbative QCD. *Parton showering* is the result of initial and final state radiation (ISR,FSR). Similar to bremsstrahlung in QED, scattered partons carrying colour charge radiate gluons. Since

gluons themselves carry colour charge, an emitted gluon can cause new radiation, resulting in a showering process with mostly soft gluons filling up the phase space. This process is simulated as a sequential step-by-step process, from high momentum (hard gluons) to low momentum scale (soft gluons), down to a point where perturbative QCD starts to break down and partons hadronise. The *hadronisation* step forming colour neutral hadrons uses non-perturbative models like the cluster model [37] used in the HERWIG generator [44] or the Lund model [37] used in the PYTHIA generator [45]. As there is a high probability that there will be other interactions in the recorded event contaminating the hard process, the simulation adds additional soft *underlying events*, also called *in-time pile-up*. In the final step of the simulation, unstable hadrons are decayed into particles that can be observed in the detector.

In order to allow for a direct comparison with data, the predicted number of MC events N_{pred} needs to be normalised to the total cross section σ_{tot} of the processes in consideration and scaled to the integrated luminosity of the data that is used. In general, MC events have weights that also need to be accounted for in the correct normalisation. Weights are for example used when including next-to-leading order (NLO) corrections in the MC generation or when using event filters during the generation, filtering only interesting events and thereby increasing the computational efficiency. Thus, instead of using the raw number of generated MC events, the sum of event weights w , scaled to the desired integrated luminosity and total cross section has to be used [46],

$$N_{\text{pred}} = \frac{\sigma_{\text{tot}} \int L dt}{\sum_{i \in \text{generated}} w_i} \cdot \sum_{i \in \text{selected}} w_i. \quad (3.3)$$

The statistical uncertainty on the MC simulation caused by the finite size of the simulated sample is then given by the square root of the sum of squared weights,

$$\Delta N_{\text{pred}} = \sqrt{\sum_{i \in \text{selected}} w_i^2}. \quad (3.4)$$

As a physical detector is not a perfect or ideal machine, the generated MC events usually undergo a detector simulation aiming to reproduce effects caused by the detector response. This is done either with GEANT4 [47] or an ATLAS fast simulation [48].

3.2.1 Used Monte Carlo samples

An overview of the MC generators used for the simulation of the SM background and SUSY signal processes considered in this work is given in table 3.1. The different SM processes considered as background in this work are further explained in section 4.2. Backgrounds like $W + \text{jets}$, $Z + \text{jets}$ and diboson production are simulated with the SHERPA generator [49]. The generation of $t\bar{t}$ and single top processes is done with POWHEG-Box v2 [50] while the parton showering is performed by PYTHIA 8 [45, 51].

Table 3.1: Overview of MC generators used for the various background and signal processes. The considered background processes are further explained in section 4.2.

Process	Generator	Parton shower
$W + \text{jets}$	SHERPA 2.2.1	SHERPA
$Z + \text{jets}$	SHERPA 2.2.1	SHERPA
WW, WZ, ZZ	SHERPA 2.2.1 / SHERPA 2.2.2	SHERPA
$t\bar{t}$	POWHEG-BOX v2	PYTHIA 8
$t\bar{t} + W/Z/WW$	MADGRAPH5_AMC@NLO 2.3	PYTHIA 8
Single top	POWHEG-BOX v2	PYTHIA 8
QCD multi-jet	PYTHIA 8	PYTHIA 8
WW SUSY signal	MADGRAPH5_AMC@NLO 2.6	PYTHIA 8
Gluino one-step SUSY signal	MADGRAPH5_AMC@NLO 2.2	PYTHIA 8

The SM background process $t\bar{t} + V^\dagger$ is generated with MADGRAPH5_AMC@NLO [52], while the parton showering is done again with PYTHIA 8. QCD multi-jet processes are simulated with PYTHIA 8. All simulated SM processes are subject to a full ATLAS detector simulation (Fullsim) [48] using GEANT 4.

The simulation of SUSY Signal is done with MADGRAPH5_AMC@NLO and PYTHIA 8. Contrary to the SM background processes, the used SUSY simulations do not undergo a full detector simulation, but the fast ATLAS simulation (AtlFast-II), allowing a 10 to 100 times faster processing than Fullsim [48]. The faster processing time is achieved by replacing the simulation of particles interacting with the detector material in the calorimeters with pre-computed parametrizations of the energy deposits per particle[§].

[†] The V in $t\bar{t} + V$ stands for *vector boson*.

[§] The parametrizations are based on a fully-simulated (i.e. with GEANT4) sample with 30 million events containing single photons and charged pions with energies between 200 MeV – 500 GeV, evenly distributed in η and ϕ [48].

Chapter 4

The 1-lepton final state

The studies presented in this work are part of ongoing research and development efforts done within an ATLAS analysis group searching for supersymmetric particles in final states with exactly one lepton. This chapter starts with a brief introduction of the existing analyses that provide the basis for this work, followed by a presentation of the backgrounds that need to be considered when studying the 1-lepton channel. Finally, the definitions of the used physics objects are discussed.

4.1 Analyses overview

This work is based on two separate analyses searching for SUSY in final states with exactly one lepton. The first analysis, hereafter called *strong 1-lepton analysis* [26] (as opposed to electroweak), considers models where squarks and gluinos are pair-produced through strong interaction and subsequently, via varying decay chains, decay into final states with exactly one isolated lepton, multiple jets and missing transverse momentum. One of the models considered by the strong 1-lepton analysis is the gluino one-step model depicted in fig. 1.3(b). This model will be of further interest in chapter 7. The strong 1-lepton analysis is a powerful search sensitive to a large variety of signal models and providing highly competitive exclusion limits on gluino and squark masses [26]. More information on the signal regions and statistical methods employed in the analysis are given in section 7.1.2.

The second analysis providing a basis for this work, is a search for supersymmetric particles that have been produced through electroweak interaction [53]. The simplified model studied by this search is depicted in fig. 4.1(a). It considers the electroweak production of the lightest chargino $\tilde{\chi}_1^\pm$ and the next-to-lightest neutralino $\tilde{\chi}_2^0$. The $\tilde{\chi}_1^\pm$ further decays into an LSP and a W boson, that, in turn, decays into a lepton and a neutrino, thereby producing a final state with a single lepton. The $\tilde{\chi}_2^0$ decays into an LSP and a Higgs boson that further decays into two b -quarks. In the detector, the two b -quarks will appear as two b -jets originating from a displaced secondary vertex and have

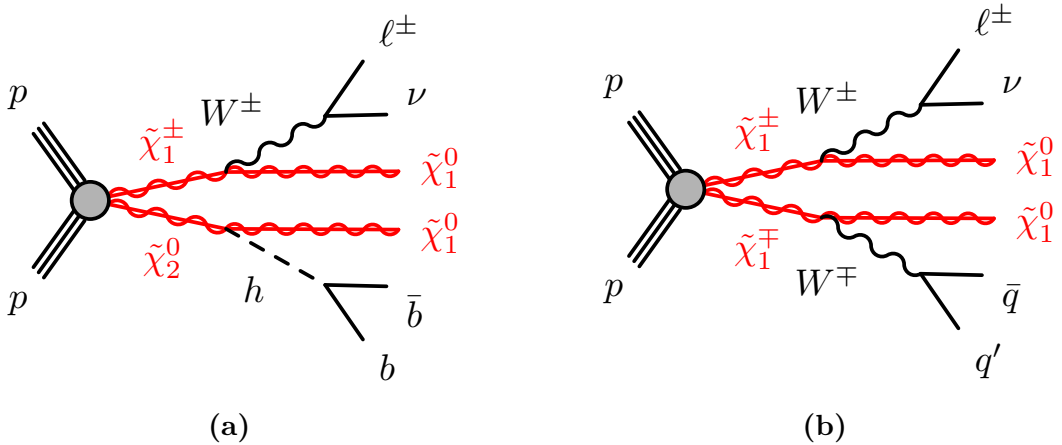


Figure 4.1: Figure (a) shows the simplified model considered in the electroweak 1-lepton analysis [53]. In the following, it will be referred to as the *Wh model*. Figure (b) shows the *WW* model again, already introduced in section 1.2.6 and used to study a possible extension of the 1-lepton analysis.

an invariant mass close to the Higgs mass. As other decays of the Higgs boson are not considered, the branching ratio $\text{BR}(H \rightarrow b\bar{b}) = 0.58$ for a Higgs boson mass of 125 GeV is factored in. In the following, this search will be referred to as the *electroweak 1-lepton analysis* and the model in question will be referred to as the *Wh model*. The presence of the two b -jets originating from a Higgs boson provides a powerful discrimination against SM processes, such that sensitivity to this model can already be expected with partial Run-2 data [53]. On the other hand, however, this introduces an inevitable model-dependency since the appearance of a Higgs boson decaying into two b -quarks is required in the supersymmetric decay chain.

Previous experience in the strong 1-lepton analysis has shown that the 1-lepton final state is a powerful channel for searching for SUSY particles produced by strong interaction while remaining model-independent to a large degree[†]. Due to the growing amount of data collected by the ATLAS detector, searches for electroweak production of SUSY particles, that have in the past often been out of reach due to lower cross-sections, are becoming increasingly interesting. Therefore, one possible improvement of the 1-lepton analyses is the extension to electroweak SUSY models that do not require distinctive decays like $H \rightarrow b\bar{b}$ and thus are more generic and result in a more model-independent search. Chapter 6 presents and discusses the results of studies assessing whether or not the 1-lepton channel is sensitive to such a generic model, namely the *WW* model shown in fig. 4.1(b).

[†] The observed data is of course interpreted in simplified models, however the studied models are chosen to be as generic as possible.

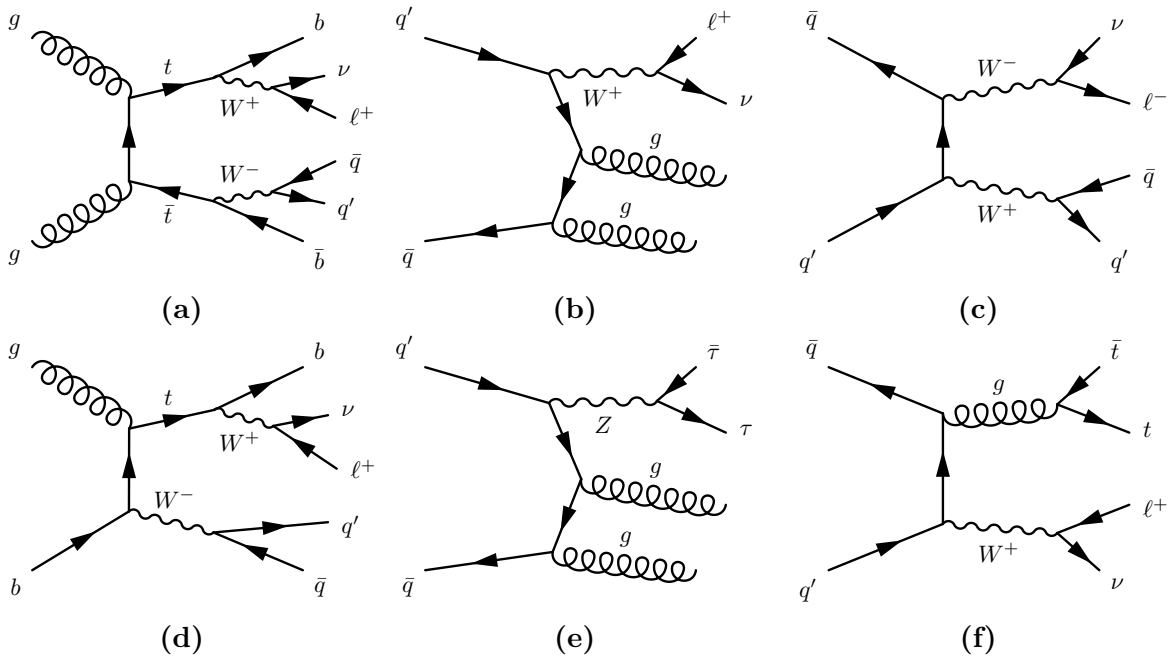


Figure 4.2: Exemplary Feynman diagrams showing (a) $t\bar{t}$, (b) $W + \text{jets}$, (c) diboson, (d) single top, (e) $Z + \text{jets}$ and (f) $t\bar{t} + V$ production with subsequent decays.

4.2 Standard Model backgrounds

Although the requirement of exactly one lepton reduces the majority of the QCD background, numerous SM processes can yield final states with exactly one isolated lepton, multiple jets and missing transverse momentum. In general, background sources can be classified into *reducible* and *irreducible* backgrounds. Irreducible backgrounds are processes that have a phase space that is indistinguishable from the signal final state. Reducible backgrounds stem from partially misreconstructed processes. An example of a source of reducible backgrounds are events where a lepton originates from a heavy flavour (HF) decay, photon conversions, or misreconstructed jets. In the SM, processes that yield an isolated lepton, jets and missing transverse momentum typically involve a leptonic decay of a W boson. The neutrino from the W boson decay will result in missing transverse momentum. QCD radiation or other branches of the process can cause additional jets to appear in the final state.

The largest SM background contribution stems from the production of a W boson with additional jets ($W + \text{jets}$) and $t\bar{t}$ production. Another important source of background in many interesting kinematic regions is diboson production. The production of single top quarks and top quark pairs with an associated vector boson ($t\bar{t} + V$) are also considered, as is the production of $Z + \text{jets}$. Figure 4.2 shows exemplary Feynman diagrams of these SM background processes, illustrating how a final state with one isolated lepton, multiple jets and missing transverse momentum can occur.

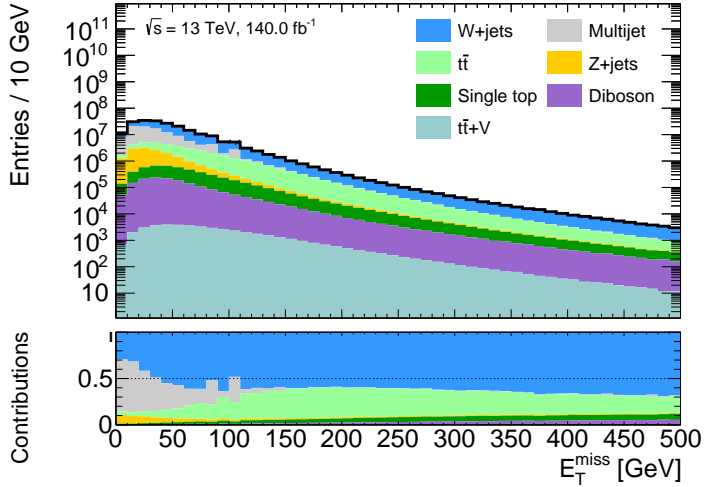


Figure 4.3: QCD background can be successfully suppressed by a cut on the missing transverse momentum. In the top part of the plot, the missing transverse energy distribution of SM processes is shown. The lower pad shows the relative contributions of the different backgrounds when integrating to the right. A preselection of exactly one isolated lepton and at least two jets is applied. With cut values above 150 GeV, the QCD multi-jet background can be reduced to a negligible amount.

For $Z + \text{jets}$, the only irreducible process comes from $Z \rightarrow \tau\tau$ where one τ -lepton undergoes a leptonic and the other one a hadronic decay. Since τ -leptons are not identified within the 1-lepton analysis, the hadronic τ is reconstructed as a jet. Other processes contributing to $Z + \text{jets}$ are reducible backgrounds, where some sort of misidentification takes place, e.g. one lepton from $Z \rightarrow \ell^+\ell^-$ could be lost during the reconstruction. Reducible processes contributing to the other backgrounds are also considered.

Pure QCD multi-jet background can only appear in the 1-lepton final state through the false reconstruction of a lepton (*fake* leptons). In this work, no MC simulation of QCD background is considered for the majority of the studies. One reason for this is the fact that a reliable MC simulation of QCD is inherently difficult and thus, signal regions with tight requirements on observables often result in very few raw MC events with unrealistically high event weights. Another reason justifying neglecting a QCD MC simulation is the suppression power of a missing transverse energy (E_T^{miss}) requirement. As can be seen in fig. 4.3 a moderate requirement of $E_T^{\text{miss}} > 150 \text{ GeV}$ already suppresses the majority of a QCD multi-jet MC simulation, to a point where the contribution from it is well below the levels of minor backgrounds like $Z + \text{jets}$ or single top. As all preselections applied within this work apply a requirement of at least $E_T^{\text{miss}} > 150 \text{ GeV}$, QCD contribution is considered to be negligible and thus a QCD estimation is not incorporated in the following[†].

[†] In a full analysis, QCD would need to be estimated with data-driven methods or more detailed studies would need to show that it is indeed negligible in every considered kinematic region.

4.3 Object definitions and event selection

The reconstruction of physics objects requires the combination of information from multiple sub-detectors. Due to the sheer amount of data generated in the collisions, this procedure does not always work without flaws. Sometimes, objects are falsely reconstructed, or not reconstructed at all. In order to minimise reconstruction errors, quality and reconstruction criteria are introduced for each physics object category. Electrons and muons are classified into *baseline* and *signal* objects. Baseline objects have a smaller purity but a higher acceptance which is useful for the computation of e.g. the missing transverse momentum in an event. Signal objects have stricter requirements on the isolation and identification criteria, leading to lower acceptance rates but also a lower rate of reconstruction errors. Signal objects are used as the physical objects within this work.

4.3.1 Event selection

Before being considered for analysis, data events need to pass the following set of event cleaning criteria:

- **Good Runs List:** Data events, where beam or detector conditions were not sufficient for physics analysis, are rejected. This information is stored in Good Runs Lists (GRL) and event-level detector flags.
- **Primary vertex:** The primary vertex of an event is the vertex with the highest $\sum p_T^2$ of its associated tracks. Only events with at least two tracks associated to this vertex are kept, others are rejected.
- **Jet rejection:** In order to reject events containing detector noise or other beam induced backgrounds, events are rejected if they do not pass the `LooseBad` quality criterion described in Ref. [54].
- **Bad Muon Veto:** Events containing a bad muon are rejected. With the charge q and momentum p of the muon, as well as the uncertainty $\sigma(q/p)$ on the q/p measurement, bad muons are muons with $\frac{\sigma(q/p)}{|q/p|} > 0.2$.
- **Cosmic Muon Veto:** Events containing cosmic muons are rejected. Reconstructed muons are considered to come from cosmic radiation if the longitudinal z_0 and transverse d_0 impact parameter with respect to the primary vertex are $z_0 > 1$ mm and $d_0 > 0.2$ mm.

4.3.2 Electrons

Electrons are charged particles and thus are reconstructed from tracks in the ID and energy deposits in the ECal [55]. The entries in the ECal are formed by clustering the

deposits starting from seeds with an energy deposit of at least 2.5 GeV. The reconstructed tracks are extrapolated to the middle layer of the ECal and matched to the clusters if close enough in η and ϕ . The tracks of signal electrons are required to fulfil $d_o/\sigma_{d_0} < 5$ and $\Delta z_0 \sin \theta < 0.5$ mm, with d_0 the transverse impact parameter, σ_{d_0} the uncertainty on d_0 and Δz_0 the distance between the nominal interaction point and the point at which d_0 is measured.

In order to discriminate electrons against background sources like HF hadron decays, photon conversions or Dalitz decays, multiple electron identification working points are defined [56]. The identification is based on a likelihood (LH) method and defines *loose*, *medium* and *tight* working points with increasing background rejection power. In this work, baseline electrons are required to pass the `LooseAndBLayerLLH` identification criterion that takes the tracking information from the insertable B-Layer into account. Signal electrons need to pass the tighter `TightLLH` working point in order to guarantee a low misidentification rate necessary for physics objects. Electrons are furthermore required to have a minimum p_T of 7 GeV and $|\eta| < 2.47$.

Additionally, signal electrons are required to be *isolated*, meaning that the vicinity of reconstructed electrons needs to be clear of other objects. This is verified by means of two variables, one based on reconstructed tracks, the other based on calorimeter entries. The track based isolation criterion $p_T^{\text{varcone}30}$ is the sum of track momenta above 1 GeV (without the electron track) in a cone around the electron. The size of the cone is chosen to be $\Delta R = \min(10 \text{ GeV}/p_T, 0.3)$, i.e. decreases with increasing p_T down to a minimal size of 0.3. The calorimeter based variable $E_T^{\text{topocone}20}$ is the sum of the transverse energies in topological calorimeter clusters (again without the electron itself) in a cone with $\Delta R = 0.2$ around the lepton. In this work, signal electrons are required to pass the `GradientLoose` requirement if the transverse momentum of the electron satisfies $p_T \leq 400$ GeV and the `FixedCutHighPtCaloOnly` requirement otherwise. The `GradientLoose` requirement makes η - and p_T -dependent requirements on the two isolation variables such that the efficiency is 95% at $E_T = 25$ GeV and 99% at $E_T = 60$ GeV. The `FixedCutHighPtCaloOnly` criterion requires that $E_T^{\text{topocone}20} < 3.5$ GeV. More details on the different working points are given in Ref. [57].

4.3.3 Muons

Muons are reconstructed from their tracks in both the inner detector and the muon spectrometer. In a first step, the muon tracks in the ID are reconstructed independently from the reconstruction in the MS. After the separate reconstruction, a statistical combination of both tracks is performed. In this work, both the baseline and signal muons are required to pass the *medium* [58] muon identification requirement. In the region with $|\eta| < 2.5$, the medium working point requires the combined muon tracks to have at least 3 hits in at least two MDT layers. In the $|\eta| < 0.1$ region, tracks with at least one MDT layer but not more than one MDT hole layer are allowed for combined tracks. In the region $2.5 < |\eta| < 2.7$ at least three MDT or CSC layers are required for tracks

extrapolated from the MS. Additionally, the medium working point also requires the q/p significance to be below 7. Baseline muons are also required to have a minimum p_T of 6 GeV and $|\eta| < 2.7$. Signal muons need to have $|\eta| < 2.5$ and the impact parameters need to fulfil $d_o/\sigma_{d_0} < 3$ and $\Delta z_0 \sin \theta < 0.5$ mm.

Similar to electrons, muons need to be isolated. Signal muons are required to pass the `GradientLoose` requirement.

4.3.4 Jets

Quarks and gluons are colour-charged particles and can, due to colour-confinement, not be detected individually. Instead, they hadronise[†] and form a collection of hadrons that can be observed in the detector as so-called *jets*. Since the hadrons in a jet tend to be boosted in the same direction, jets are in general cone-shaped. Two main approaches of reconstructing jets exist. The most intuitive method is to use a bottom-up approach that defines a cone with a certain radius R , then iteratively computes the sum of the momenta of its constituents and uses the resulting direction as the centre of the next cone in the iteration. This procedure stops once a stable cone has been found. However, such a bottom-up approach has the disadvantage of being infrared and/or collinear unsafe, meaning that it is not robust against adding a soft parton and/or splitting a parton into two collinear partons. A way of circumventing this issue is by using the top-down approach of a sequential recombination algorithm that iteratively recombines the constituents of a jet until the remaining objects are too far away from each other.

In this work, jets are clustered by the anti- k_t algorithm [59, 60], a sequential recombination algorithm that is infrared and collinear safe. The topological clusters used as input for the anti- k_t algorithm are formed by a topological cell clustering algorithm [61] selecting calorimeter cells with a certain threshold energy and signal-over-noise ratio as seeds and clustering topologically connected cells that satisfy a set of conditions. A standard radius parameter of $R = 0.4$ is used for the anti- k_t algorithm.

Jets with $p_T < 50$ GeV and $|\eta| < 2.4$ have to be matched to the primary vertex through the jet vertex tagger (JVT) [62], suppressing jets from pile-up. Additionally, jets are calibrated following the criteria in Ref. [63], which, among other things, includes corrections to the jet energy and resolution. Furthermore, jets are required to have a minimum p_T of 20 GeV and $|\eta| < 4.5$. Observables built from jets (e.g. the jet multiplicity) use central jets with $|\eta| < 2.8$ and $p_T > 30$ GeV.

4.3.5 B-tagging

As can be easily seen through the CKM matrix, the primary decay of the b -quark is into a b -quark via $b \rightarrow W c$. However, due to the small coupling constant $\propto V_{cb}$ [§], the decay is so

[†] Except for the top quark because it is so massive that it decays before hadronising.

[§] V_{cb} is the entry in the CKM matrix corresponding to the $b \leftrightarrow c$ transition.

slow that B -mesons have typical lifetimes of $\mathcal{O}(\text{ps})$ [37], which is, in typical momentum ranges of $\mathcal{O}(10^2 \text{ GeV})$, long enough to see displaced decay vertices in the detector.

In this work, b -jets are identified with the MV2 classifier [64], a multivariate discriminant using boosted decision trees (BDT) in order to combine the output of three different b -tagging algorithms. The first of these is an impact parameter based algorithm, the second is a secondary vertex finder and the third is a multi-vertex reconstruction algorithm that tries to reconstruct full b -hadron decay chains. The MV2c10 classifier is used to identify b -jets by cutting on the output score such that the b -tagging efficiency is at 77% [64].

4.3.6 Missing transverse momentum

Since the exact momentum fraction of the colliding partons is unknown, momentum and energy conservation cannot be used in the longitudinal direction, but only in the transverse plane[†]. Therefore, particles escaping the detector without interaction lead to a momentum imbalance in the transverse plane. The missing transverse momentum is reconstructed by using the set of reconstructed and fully calibrated electrons, muons, photons and jets (denoted as ξ in eq. (4.1)) as well as the tracks not associated to a reconstructed object (track soft terms, TST) [65],

$$\mathbf{p}_T^{\text{miss}} = - \sum_{i \in \xi} \mathbf{p}_{T,i} - \sum_{i \in \text{TST}} \mathbf{p}_{T,i}. \quad (4.1)$$

The magnitude of the missing transverse momentum is denoted as the missing transverse energy $E_T^{\text{miss}} \equiv |\mathbf{p}_T^{\text{miss}}|$.

4.4 Overlap removal

During the reconstruction procedure, it can happen that the same tracks or energy deposits are reconstructed and identified as two separate physics objects. For example, electrons tend to be clustered as well as jets and are therefore often also reconstructed as a jet [66]. In order to prevent this kind of double-counting but also improve the isolation of physics objects, an overlap removal (OR) procedure is carried out on baseline objects. The OR uses $\Delta R = \sqrt{(\Delta y)^2 + (\Delta\phi)^2}$ as distance measure and applies the following steps [46, 66]:

1. If two electrons share the same ID track, then the one with the lower p_T is discarded.
2. Electrons sharing the same ID track with a muon are rejected.
3. Non b -tagged jets within $\Delta R < 0.2$ of an electron are rejected.

[†] Assuming that the initial momenta of the colliding partons in the transverse plane is negligible.

4. Electrons overlapping with one of the remaining jets are removed. The cone size used to define the overlap is $\Delta R = \min(0.4, 0.04 + 10 \text{ GeV}/p_T)$, i.e. shrinks with increasing electron p_T .
5. Reject non b -tagged jets within $\Delta R < 0.2$ of a muon or where muons have been matched to the jet through ghost association [67], a procedure that associates four-vectors of infinitesimal magnitude to tracks before using them in the jet reconstruction, preventing the tracks to change the properties of the calorimeter-based jets. A muon is matched with a jet if a ghost version of one of its partial tracks, reconstructed from hits in the MS, is contained in the jet after reclustering.
6. Muons overlapping with a remaining jet are removed. The same shrinking cone size as for the electrons is used.

Chapter 5

Statistical data analysis

In high energy particle physics, it is necessary to perform statistical data analysis in order to get objective assessments of the observed data. Therefore, this chapter aims to introduce the basic statistical concepts that are used for the signal region optimisation as well as for the computation of the exclusion limits presented throughout this work. The introduction to the statistical methods given in this chapter largely follows Refs. [68] and [69].

5.1 Likelihood

In the statistical models used within this work, binned *Likelihood* fits are employed (see sections 6.5 and 7.1.2 for details concerning the implementation). Each bin corresponds to a kinematic region used in the analysis. In general, in the SUSY searches considered in this work, three types of kinematic regions are designed: *signal regions*, *control regions* and *validation regions*. Each region type can be composed of one or many bins. Signal regions are phase spaces enriched in signal events, used to detect and study the signal processes. Control regions are background-dominated regions that are used to estimate background events in the signal regions by comparing the predicted events in each control region with data and extrapolating correction factors to the signal regions. Finally, validation regions are used to validate this extrapolation and are therefore typically placed in phase spaces between the control and the signal regions.

In simple counting experiments where each event is independent from previous events, each defined bin can be described by its own Poisson term. The Poisson probability to observe k events with an expectation of λ is given by

$$P(k|\lambda) = \frac{\lambda^k}{k!} e^{-\lambda}. \quad (5.1)$$

The total Likelihood is constructed through the product over all Poisson distributions for each considered bin. The expectation λ_i in each bin i can be parametrised through the introduction of a signal strength parameter μ_{sig} , yielding

$$\lambda_i = \mu_{\text{sig}} s_i + b_i, \quad (5.2)$$

where, for each bin i , s_i is the number of expected signal events and b_i the number of expected background events. This allows to use μ_{sig} as a free parameter in the fit, with $\mu_{\text{sig}} = 0$ being the *background-only* hypothesis and $\mu_{\text{sig}} = 1$ corresponding to the *signal-plus-background* hypothesis with the nominal cross-section considered in the model. Since only positive signals are considered in this work[†], the signal strength parameter is constrained by $\mu_{\text{sig}} \geq 0$. The expected signal and background event yields generally depend on a set of *nuisance parameters* $\boldsymbol{\theta}$ (the bold font is used to emphasize the fact that this is a set of parameters). Nuisance parameters that are directly constrained through data observations in background-dominated control regions are called *normalisation factors* $\boldsymbol{\mu}_{\text{bkg}}$. On the other hand, nuisance parameters can also be used to describe systematic uncertainties $\boldsymbol{\alpha}$ [46]. Each uncertainty is constrained by an auxiliary measurement described by a unit Gaussian G_{sys} with central value α^0 . In general, the likelihood can be constructed by

$$L(\mu_{\text{sig}}, \boldsymbol{\mu}_{\text{bkg}}, \boldsymbol{\alpha}) = \prod_{i \in \text{bins}} P(k_i | \lambda_i(\mu_{\text{sig}}, \boldsymbol{\mu}_{\text{bkg}}, \boldsymbol{\alpha})) \prod_{j \in \text{sys}} G_{\text{sys}}(\alpha^0 | \alpha_j). \quad (5.3)$$

A single likelihood function can be built for the full set of signal, control and validation regions used within an analysis.

5.2 Test statistics

Test statistics are a tool used in the evaluation of hypotheses. At the LHC, the definitions of test statistics for hypotheses based on models that can be expressed through a likelihood, use the *profile likelihood ratio*,

$$\lambda(\mu) = \frac{L(\mu, \hat{\boldsymbol{\theta}})}{L(\hat{\mu}, \hat{\boldsymbol{\theta}})}. \quad (5.4)$$

Here, $\hat{\boldsymbol{\theta}}$ is the conditional maximum-likelihood (ML) estimator of $\boldsymbol{\theta}$, i.e. the value of $\boldsymbol{\theta}$ that maximises L for a given μ . The parameters $\hat{\mu}$ and $\hat{\boldsymbol{\theta}}$ are the ML estimators for the unconditionally maximised likelihood function. For the sake of notational conciseness, $\mu \equiv \mu_{\text{sig}}$ in the following.

[†] The presence of new physics can, in this work, only cause an increase in the number of total events.

In order to discover a new signal, i.e. rejecting the $\mu = 0$ hypothesis, a one-sided discovery test statistic q_0 is built with $\lambda(\mu)$,

$$q_0 = \begin{cases} -2 \ln \lambda(0), & \hat{\mu} \geq 0, \\ 0, & \hat{\mu} < 0. \end{cases} \quad (5.5)$$

If the data presents fluctuations such that fewer events are seen than expected by only considering background processes, then $q_0 = 0$ and the background-only hypothesis cannot be rejected. This is sensible since $\mu \geq 0$ and hence the observation of fewer events than expected is not considered as evidence against the background-only hypothesis. In case more events are seen than expected by background processes, this definition produces increasingly large values of q_0 , corresponding to an increasing level of incompatibility between data and the background-only hypothesis.

If the background-only hypothesis cannot be rejected, the hypothesis test can be swapped around and instead the signal-plus-background hypothesis can be tested. For this case, the one-sided exclusion test statistic q_μ is built,

$$q_\mu = \begin{cases} -2 \ln \lambda(\mu), & \hat{\mu} \leq \mu, \\ 0, & \hat{\mu} > \mu. \end{cases} \quad (5.6)$$

Setting $q_\mu = 0$ for $\hat{\mu} > \mu$ (i.e. defining the test statistic to be one-sided) ensures that the observation of more events than expected with the signal-plus-background hypothesis is not considered as evidence against it. The test statistic q_μ allows to establish upper limits on the signal strength parameter and therefore is used to exclude signals.

5.3 *p*-values

In order to quantify the level of disagreement between the considered null hypothesis and the observed data, a *p*-value can be computed. The *p*-value indicates the probability of obtaining a similar or even more extreme outcome, often corresponding to higher values of the test statistic. The *p*-value is therefore defined as the integral of the test statistic distribution $f(q|\xi)$ given certain model assumptions ξ ,

$$p = \int_{q_{\text{obs}}}^{\infty} f(q|\xi) dq. \quad (5.7)$$

The *p*-value is often interpreted in terms of Gaussian standard deviations through the quantile function Φ^{-1} by

$$Z = \Phi^{-1}(1 - p). \quad (5.8)$$

The *significance* Z indicates how many Gaussian standard deviations the measured value is away from the expected value. In order to claim a discovery, i.e. reject the

background-only hypothesis, a significance of $Z = 5$ is needed. A significance of $Z = 3$ is interpreted as evidence for the existence of a signal. In the case of very large background b and low signal s , i.e. $s \ll b$, the significance can be approximated through

$$Z = \frac{s}{\sqrt{b}}. \quad (5.9)$$

A more accurate calculation also takes uncertainties on background events into account. An implementation of this is given by the **RooStats** framework [70]:

```
RooStats::NumberCountingUtils::BinomialExpZ(s,b,Δbrel),
```

where Δb_{rel} is the total relative uncertainty on the background. In case both statistical and systematic uncertainty are considered, the total relative background uncertainty can be written as

$$\Delta b_{\text{rel}} = \frac{\Delta b}{b} = \sqrt{\left(\frac{\Delta b_{\text{stat}}}{b}\right)^2 + \left(\frac{\Delta b_{\text{sys}}}{b}\right)^2}. \quad (5.10)$$

Based on previous experiences in the 1-lepton final state, a flat 30% systematic uncertainty is, in this work, often taken as an approximation for a full evaluation of systematics.

In the case where the exclusion power for a signal is low, an underfluctuation of data can cause the signal to be accidentally excluded. In order to prevent this, the exclusion p -value p_{s+b} is divided by $1 - p_b$, where p_b is obtained from the exclusion test statistic using $\mu = 0$, resulting in a quantity called CL_s ,

$$CL_s = \frac{p_{s+b}}{1 - p_b}. \quad (5.11)$$

The signal-plus-background hypothesis is excluded by requiring $CL_s < 0.05$, also referred to as 95% confidence level (CL). All exclusion contours shown in this work are drawn at 95% CL.

Chapter 6

Sensitivity studies for electroweak Supersymmetry

As explained in chapter 4, events with one lepton in the final state are a powerful channel for SUSY searches. Previous experiences with strong production signal models [26, 71] have shown that it is possible to design an analysis that is sensitive to a multitude of different production and decay modes. Unlike strong production models, electroweak models have, in the past, often been beyond the reach of searches for SUSY due to the lower cross-sections. With the growing amount of data collected by the ATLAS detector, however, electroweak models are becoming increasingly interesting. Therefore, this chapter presents efforts assessing the sensitivity of the 1-lepton channel to the generic electroweak signal model $\tilde{\chi}_1^\pm \tilde{\chi}_1^\pm \rightarrow WW \tilde{\chi}_1^0 \tilde{\chi}_1^0$, a model that does not rely on distinctive decays like e.g. $h \rightarrow b\bar{b}$. This model has been introduced in sections 1.2.6 and 4.1. All the studies presented in this chapter are performed with MC simulations normalised to an integrated luminosity of 140 fb^{-1} , which roughly corresponds to the currently projected amount of data collected by ATLAS by the end of Run-2 [72].

6.1 Discriminating observables

In order to be able to distinguish supersymmetric events from SM processes, it is necessary to use different discriminative observables. This section introduces the various observables used to determine the sensitivity of the 1-lepton analysis to the WW model.

The plots in figs. 6.1 and 6.2 show exemplary kinematic distributions of each observable introduced in the following. Both the distributions of the SM background (coloured areas) and the SUSY signal (coloured lines) are shown, each normalised to unity in order to emphasize the difference in shape of each distribution. While the different SM processes are stacked on top of each other, the signal histograms are superimposed on the SM

background. Multiple benchmark signal points[†] with different $\tilde{\chi}_1^\pm$ and $\tilde{\chi}_1^0$ masses are shown, each following the naming convention ‘ $(m(\tilde{\chi}_1^\pm), m(\tilde{\chi}_1^0))$ ’, with both masses in GeV. All distributions are shown after requiring exactly one lepton and at least two jets with $p_T > 30$ GeV as a preselection. In the following, the term *cut* refers to a lower or upper requirement on a given observable.

Lepton and jet momenta

The supersymmetric particles in the decay chain of the considered signal model have, in general, higher masses than most of the SM particles. In cases where the mass difference between the $\tilde{\chi}_1^0$ and the $\tilde{\chi}_1^\pm$ is high, the particles originating from the supersymmetric decays tend to have higher momenta than in many SM processes. Therefore, the transverse momenta of the produced jets and the lepton, are considered to be promising observables for discriminating against SM processes.

In more compressed scenarios, i.e. where the mass of the $\tilde{\chi}_1^0$ is closer to the mass of the $\tilde{\chi}_1^\pm$, the transverse momenta have a lower importance since the produced particles in the final state tend to have relatively low energies. Figures 6.1(a) to 6.1(c) illustrate the discriminative power of the transverse momenta for different kinematic scenarios. In the following, objects with high transverse momentum are often referred to as *hard*, while objects with low transverse momentum are called *soft*.

Number of jets N_{jet}

As can be seen in fig. 1.3(a), the final state of the considered WW model explicitly features two jets originating from the decay of one W boson. By allowing a third additional jet in the final state, e.g. due to ISR or FSR, and thereby requiring events to either have two or three jets in the final state, it is possible to reduce the SM background.

Number of b -tagged jets $N_{b\text{-jet}}$

Similar to the total number of jets in the final state, the number of b -tagged jets is a helpful observable allowing to differentiate SUSY processes from SM background. In SM processes involving top quarks, the final state tends to have b -jets since the top quark mainly decays into a bottom quark through $t \rightarrow Wb$. No explicit top quark appears in the considered SUSY decay chain, thus the b -jet multiplicity is in general lower for this SUSY model than for many SM events and an upper cut on the number of b -tagged jets allows to suppress background processes involving top quarks.

[†] As explained in section 1.2.6, a *signal point* is an instance of the considered signal model with a given set of particle masses.

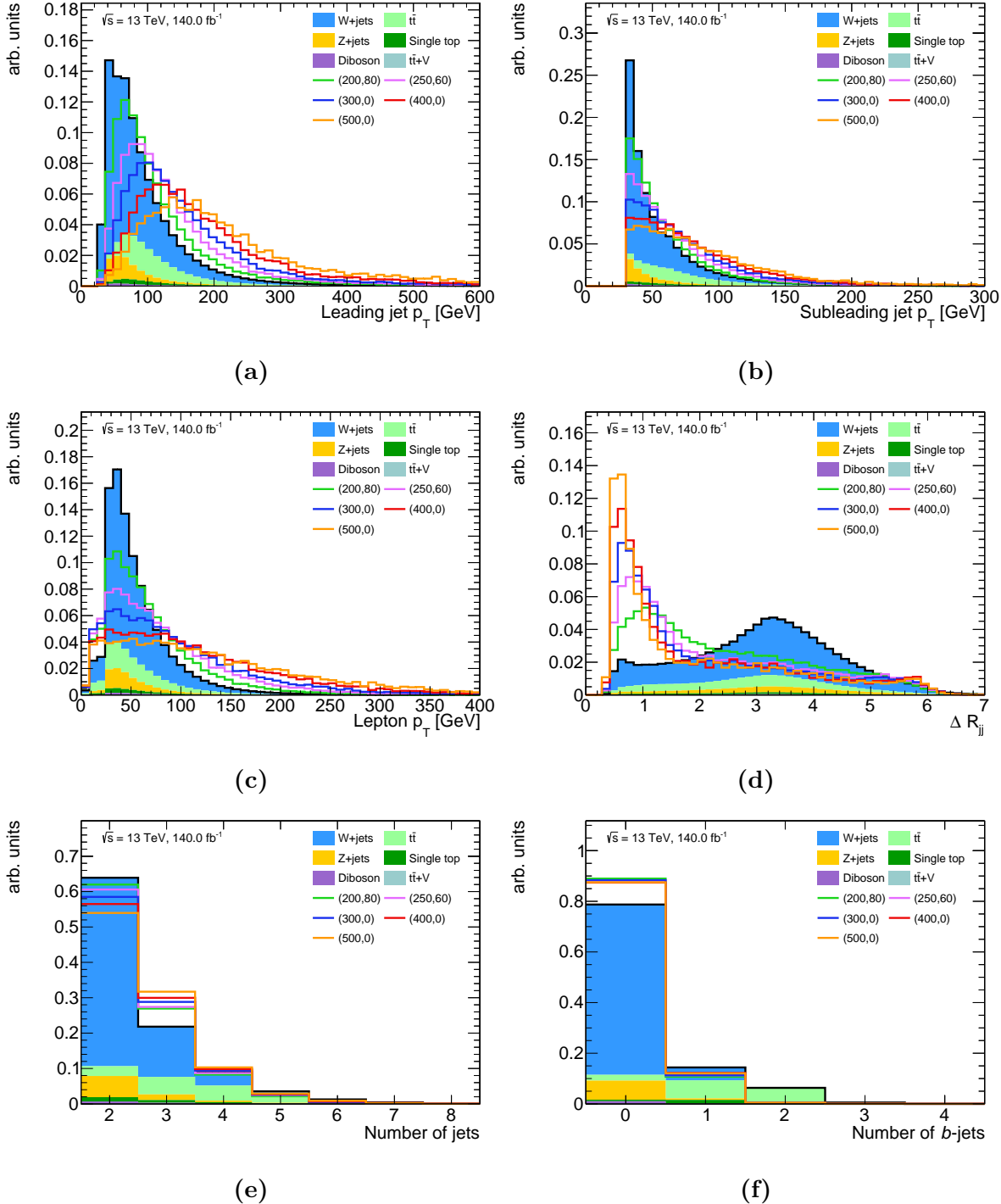


Figure 6.1: First set of observables used in the sensitivity studies. The backgrounds (coloured areas) are stacked on top of each other and the total stack is normalised to unit area. The signals (coloured lines) are superimposed and also normalised to unit area. As a consequence, the difference in shape between the background and the signal for different observables is clearly visible. The naming convention for the different signal points is $(m_{\tilde{\chi}_1^\pm}, m_{\tilde{\chi}_1^0})$, with both masses in GeV.

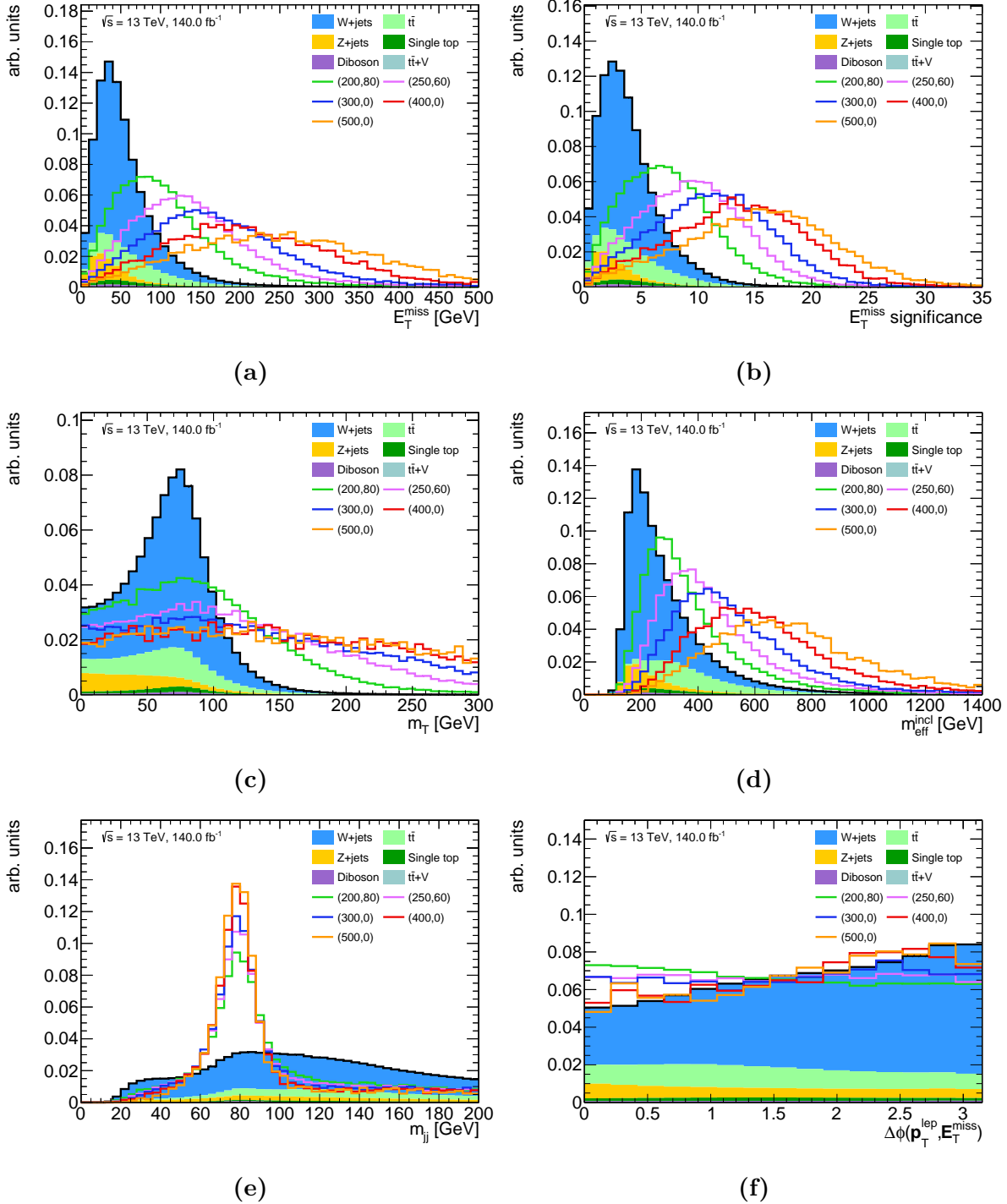


Figure 6.2: Second set of observables used in the sensitivity studies. The backgrounds (coloured areas) are stacked on top of each other and the total stack is normalised to unit area. The signals (coloured lines) are superimposed and also normalised to unit area. As a consequence, the difference in shape between the background and the signal for different observables is clearly visible. The naming convention for the different signal points is $(m_{\tilde{\chi}_1^\pm}, m_{\tilde{\chi}_1^0})$, with both masses in GeV.

Missing transverse energy E_T^{miss}

In SM processes, the missing transverse energy mainly stems from neutrinos escaping the detector. Additional sources of E_T^{miss} come from mismeasurements or errors in the reconstruction.

For the SUSY processes considered, two neutralinos escape the detector in addition to the neutrino. The SUSY processes thus tend to have a much higher E_T^{miss} than SM processes, such that a lower requirement on the E_T^{miss} distribution separates SUSY events from SM processes.

Missing transverse energy significance

Finite detector resolution can cause events without real E_T^{miss} to receive some missing transverse energy during reconstruction. This is called *fake* E_T^{miss} and can have different detector-related origins. For example, the momenta of particles (here especially jets) can be mismeasured and entire particles can be incorrectly or not at all reconstructed, resulting in fake E_T^{miss} . Non-instrumented regions of the detector, where particles can escape without being detected also contribute to fake E_T^{miss} . The E_T^{miss} significance S [73] helps in rejecting events with fake E_T^{miss} . Given a certain $\mathbf{E}_T^{\text{miss}}$ (the bold font is used again for vectorial quantities), it tests the hypothesis that the total transverse momentum carried by invisible particles $\mathbf{p}_T^{\text{inv}}$ is equal to zero against the hypothesis that $\mathbf{p}_T^{\text{inv}}$ is different from zero. With the likelihood function of $\mathbf{p}_T^{\text{inv}}$ for a given measured value of $\mathbf{E}_T^{\text{miss}}$, the significance S is defined as the log-likelihood ratio [73]:

$$S^2 = 2 \ln \left[\frac{\max_{\mathbf{p}_T^{\text{inv}} \neq 0} \mathcal{L}(\mathbf{E}_T^{\text{miss}} | \mathbf{p}_T^{\text{inv}})}{\max_{\mathbf{p}_T^{\text{inv}} = 0} \mathcal{L}(\mathbf{E}_T^{\text{miss}} | \mathbf{p}_T^{\text{inv}})} \right]. \quad (6.1)$$

As can be seen in fig. 6.3(a), events with high fake E_T^{miss} , i.e. events where the resolution $\delta E_T^{\text{miss}} = (E_T^{\text{miss}} - E_T^{\text{miss,truth}})/E_T^{\text{miss,truth}}$ has a high value, have a low E_T^{miss} significance value. A lower requirement on the E_T^{miss} significance would thus get rid of most of the events with high fake E_T^{miss} . However, as fig. 6.3(b) shows, the missing transverse energy itself reveals a similar behaviour, with objects with fake E_T^{miss} accumulating at relatively low E_T^{miss} values. Taking into account the correlation between the missing transverse energy and the E_T^{miss} significance shown in fig. 6.3(c), it is not clear a priori that one of the two observables will perform significantly better than the other. Thus, for the purpose of comparison, both of them are used in the following.

Transverse mass m_T

The transverse mass m_T [74] is a powerful variable in the 1-lepton channel [26]. As can be seen in equation (6.2), its computation closely follows the computation of the invariant

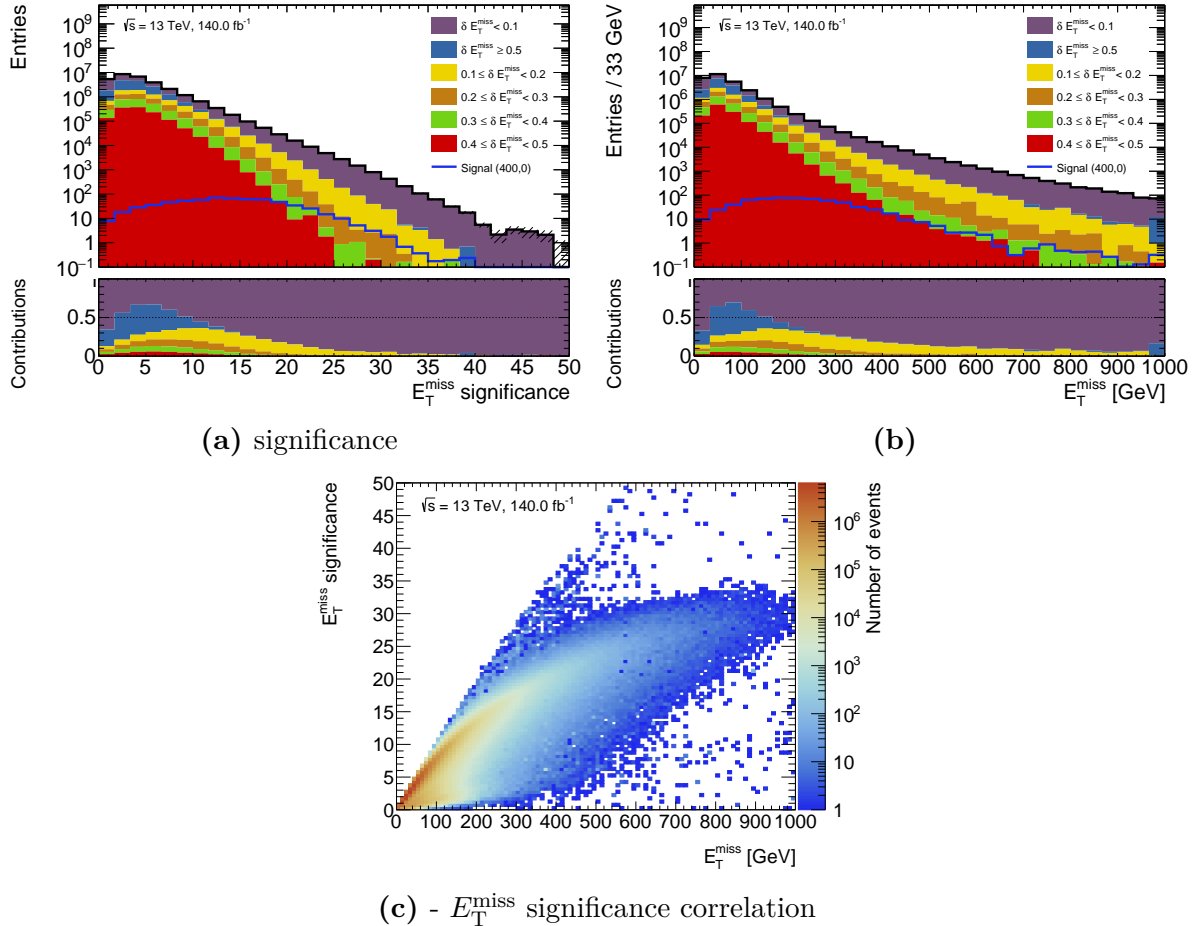


Figure 6.3: The E_T^{miss} significance could help to reduce the amount of $W + \text{jets}$ events with fake E_T^{miss} . In fig. (a), the $W + \text{jets}$ events are classified according to their E_T^{miss} resolution δE_T^{miss} . Events with high δE_T^{miss} have high fake E_T^{miss} . Figure (b) shows the same classification in the E_T^{miss} distribution. In fig. (c), the correlation between E_T^{miss} and the E_T^{miss} significance is shown. In all plots, a preselection of exactly one lepton and at least two jets is applied.

mass, with the difference that transverse objects are used, namely the missing transverse momentum $\mathbf{p}_T^{\text{miss}}$ and the transverse momentum of the lepton \mathbf{p}_T^ℓ :

$$m_T = \sqrt{2p_T^\ell E_T^{\text{miss}} (1 - \cos [\Delta\phi (\mathbf{p}_T^\ell, \mathbf{p}_T^{\text{miss}})])}. \quad (6.2)$$

In most SM processes in the 1-lepton channel, both the lepton and the missing transverse momentum originate from the decay of a W boson, hence the m_T distribution has a kinematic endpoint at the W boson mass. In the SUSY events considered in this work, there are sources of E_T^{miss} other than the decaying W boson, thus the m_T distribution is in general more spread out. As can be seen in fig. 6.2(c), the background rejection power (at a given signal efficiency level) of m_T is best for signal points with a high mass difference between the $\tilde{\chi}_1^\pm$ and the $\tilde{\chi}_1^0$, i.e. for signal points where most of the missing transverse momentum is carried by the two neutralinos instead of the neutrino.

Effective mass m_{eff}

The effective mass m_{eff} is the sum of the missing transverse energy and the transverse momenta of the lepton and the jets,

$$m_{\text{eff}} = p_T^\ell + \sum_{\text{jets}} p_T + E_T^{\text{miss}}. \quad (6.3)$$

Since SUSY particles are heavier than SM particles, their SM decay products tend to be more energetic and consequently the effective mass is in general higher. Additionally, the effective mass distribution is sensitive to the mass difference between the $\tilde{\chi}_1^\pm$ and the $\tilde{\chi}_1^0$. Despite the obvious correlation with the lepton and jet momenta as well as the E_T^{miss} , all of which are already used as stand-alone observables, the m_{eff} is still used as discriminative variable in the cut optimisation.

Distance between jets ΔR_{jj}

In case of a high mass differences between the $\tilde{\chi}_1^\pm$ and the $\tilde{\chi}_1^0$, the W bosons often have high momenta. As a result, the two jets originating from a hadronic decay of one of the W bosons are often highly boosted in one direction, resulting in a small distance between the two jets. The distance measure is defined by

$$\Delta R_{\text{jj}} = \sqrt{(\Delta\phi_{\text{jj}})^2 + (\Delta\eta_{\text{jj}})^2}, \quad (6.4)$$

where ‘jj’ refers to the two leading jets (p_T -wise). As fig. 6.1(d) shows, the distance between the two leading jets tends to be higher in SM processes than in the SUSY events considered. Additionally, it can be seen that ΔR_{jj} is less discriminative for compressed signal points than for points with high mass differences between the $\tilde{\chi}_1^\pm$ and the $\tilde{\chi}_1^0$.

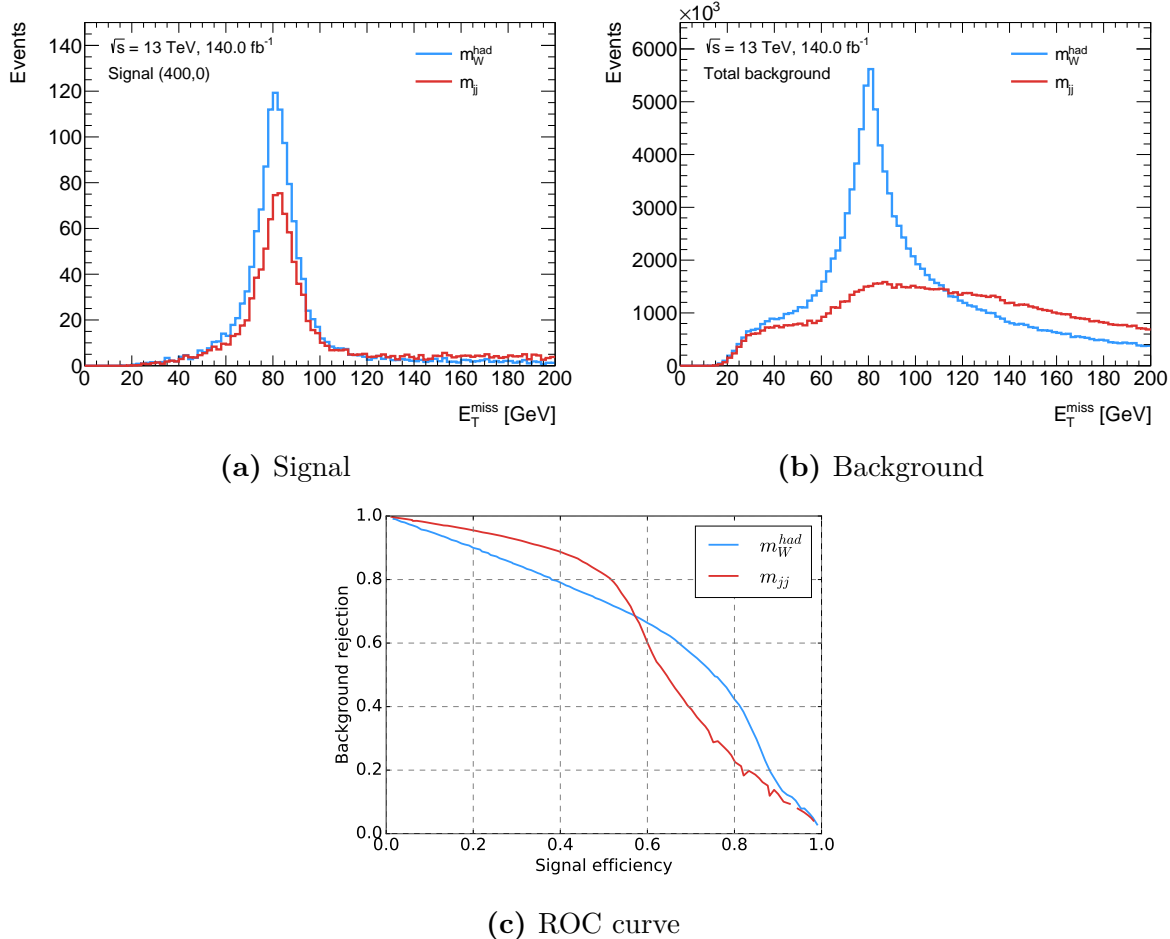


Figure 6.4: Different dijet mass definitions yield different distributions. Figure (a) shows the distribution for an exemplary signal point, while fig. (b) shows the distribution for the total SM background. Figure (c) shows a receiver operating characteristic (ROC) curve comparing the two variations.

Reconstructed mass of the dijet system

In the SUSY events considered, the hadronic decay of one of the W bosons is the main source of jets in the final state. Taking two jets as a combined *dijet system* and reconstructing the invariant mass m_{jj} should therefore yield a peak around the W boson mass. For background events, there are also other sources of jets apart from W bosons decaying into jets. Thus, by simple combinatorial consideration, the reconstructed dijet mass is expected to yield a broader distribution than for SUSY events. A window cut around the W boson mass could therefore predominantly select signal events over background events.

As many events have more than two jets in the final state, there is often no single way to select the two jets that the invariant mass should be computed of. Figure 6.4 shows a comparison of the different variations that are explored in the following. A first definition,

named m_W^{had} , iterates over all the jets in an event and calculates the invariant mass of the different possible dijet systems through their Lorentz vectors, finally taking the value that lies closest to the W boson mass. This yields a distribution with a narrow peak at the W boson mass for signal events, and a slightly broader peak for background events.

In a second variation the Lorentz vectors of the two highest energetic jets are used, regardless of whether there are other jets in the event or not. This obviously results in a higher rate of dijet systems not originating from the same W boson, causing the peak around m_W to be less pronounced in signal events (see fig. 6.4(a)). For background events, however, fig. 6.4(b) shows that the peak around the W boson mass nearly completely disappears.

In fig. 6.4(c), the background rejection rate is plotted against the signal efficiency[†] in a so-called receiver operating characteristic curve (further explained in section 6.2.1). It can be seen that for the high background rejection rate that is needed, m_{jj} yields better signal efficiencies and is therefore preferred over m_W^{had} .

Angular distance between E_T^{miss} and the lepton

Another interesting observable used to discriminate signal events from background events is the angular distance between the E_T^{miss} and the lepton. In background events, the E_T^{miss} and the lepton often originate from processes involving the decay of a W boson through $W \rightarrow \ell\nu$. As fig. 6.2(f) shows, $W + \text{jets}$ events have a higher chance of a back-to-back emission of the lepton and the neutrino, while, in the considered signal events, the $\Delta\phi$ distribution is in general more evenly spread out.

6.2 Optimisation methods

The two optimisation methods used in section 6.3 are based on the approach of maximising the expected discovery significance by appropriately modifying upper and/or lower requirements on the observables presented in section 6.1. The first method is a multidimensional scan over all the possible combinations of cuts on the used observables, employed to scan a broad range of different kinematic regions. The second method uses one-dimensional scans of each of the used observables while applying all the selection cuts except for the cut on the scanned observable, especially useful for fine-tuning individual requirements.

6.2.1 Multidimensional cut scan

A multidimensional cut scan on N observables, therefore also called an N -dimensional cut scan, is the main optimisation method used in section 6.3. By carefully comparing

[†] The term *signal efficiency* denotes the rate of signal events that pass a given cut combination.

with the distributions at preselection level shown in figs. 6.1 and 6.2, it is possible to define a range of discrete cut values for each observable. Since the total number of cut combinations increases rapidly when adding more cuts or variables to be scanned, the ranges have to be chosen carefully. In the N -dimensional cut scan, for each possible cut combination, the number of expected signal and background events, as well as the statistical uncertainty of the background is calculated from the MC samples. As this procedure takes a significant amount of time, it is important to restrict the number of cut combinations to a manageable level. In practice, a total number of the order of 10^7 – 10^8 cut combinations is still computationally feasible.

After determining the expected signal and background yields as well as the statistical uncertainty for each cut combination, the different combinations are binned into a predefined number of signal efficiency bins. For each signal efficiency bin, the background rejection is subsequently maximised, i.e. the cut combination with the highest background rejection is chosen as a candidate for the respective signal efficiency bin. This effectively creates a receiver operating characteristic (ROC) curve. Since only a small subset of all scanned cut combinations are selected as candidates and lie on the ROC curve, more computationally intensive calculations can be performed.

A common problem with N -dimensional cut scans is *overtightening* the cuts compared to the available MC statistics. As the cross sections of SM processes are many orders of magnitude higher than those of SUSY processes, it is often necessary to apply tight cuts on discriminative observables in order to isolate signal events from backgrounds. However, due to the finite amount of MC statistics available to simulate both SM and SUSY events, many of the more extreme cut combinations select kinematic regions where not enough MC statistics is available to correctly simulate the kinematic distributions. By maximising the background rejection, extreme cut combinations favour situations where the mere lack of simulated MC background events produces a high significance value. Significance values obtained from such regions are of course not trustworthy since the obtained background estimation is not reliable. In order to avoid such situations, the N -dimensional scan uses a train-test approach, very common in the machine learning field (see e.g. [75, 76]). The available MC statistics are split in two statistically independent datasets, allowing to have two independent significance values per cut combination as well as two independent ROC curves. A large discrepancy between the two significance values or the ROC curves is a strong indication for overtightening of cuts in the sense that the applied cuts are too extreme for the available MC statistics in the respective kinematic regions.

The implementation of N -dimensional cut scans with a train-test approach used within this work is done with `ahoi` [77], a publicly available software package developed by Nikolai Hartmann.

6.2.2 N-1 plots

Instead of using a brute-force algorithm to scan through a long list of possible combinations, a more manual procedure can be used, called *N-1 plots*. Each of the N observables is scanned in a one-dimensional plot and all the cuts except for the cut on the scanned observable are applied. With this procedure, the impact of a cut on a single observable and the reached significance value in dependence of the exact cut value can be investigated. By repeating this process for each observable, it is theoretically possible to iteratively approach a cut combination yielding comparable results to an N -dimensional scan. While this iterative procedure allows to manually check the statistics and validity of the cut combination at each step, in practice, it often fails to capture more complex correlations between observables.

Therefore, in this work, N-1 plots are used as a complement to an N -dimensional cut scan, allowing to verify and fine-tune the requirements obtained after the cut scan.

6.3 Cut optimisation

6.3.1 Setup and technical details

By examining the kinematic distributions shown in figs. 6.1 and 6.2, the cut ranges in table 6.1 are chosen[†]. Except for the cuts on the jet multiplicity, each cut range features a default requirement that allows the optimisation algorithm to optionally not apply a cut at all on the respective observable. For example, a requirement on $p_T^\ell > 0 \text{ GeV}$ is always fulfilled[§] and thus is the same as applying no lower requirement on p_T^ℓ at all.

Five different benchmark signal points with different $\tilde{\chi}_1^\pm$ and $\tilde{\chi}_1^0$ masses are used in order to get a first sensitivity estimation for models with varying kinematic properties (dictated by the SUSY particle masses). The different signal points are chosen to be around the currently expected exclusion limit for this model, set by an analysis searching for SUSY in events with 2 leptons in the final state with 36.1 fb^{-1} of data [78]. Each signal point is optimised separately in order to get independent significance estimations for the various kinematic regimes in the signal grid. As will be shown in the following, $W + \text{jets}$ is in many kinematic regions the most dominant background, followed by diboson and $t\bar{t}$ production. Unfortunately, $W + \text{jets}$ is also by far the most dominant source of statistical uncertainty. Therefore, in order for a cut combination to be considered by the N -dimensional cut scan, it is required to have at least ten unweighted Monte Carlo $W + \text{jets}$ events with a statistical uncertainty of less than 40% as well as a total statistical uncertainty on the

[†] In fact, the chosen cut ranges are subject to a previous manual optimisation procedure determining ideal ranges in terms of computational efficiency and obtained results.

[§] As described in sections 4.3.2 and 4.3.3, electrons (muons) used within this work are required to have a minimum p_T of 7 GeV (6 GeV).

Table 6.1: List of observables and cut ranges used in the N -dimensional cut scan. All cut ranges, except for N_{jet} , have default values that allow the scan to not apply the cut at all, e.g. a cut of $p_T^\ell > 0 \text{ GeV}$ is always fulfilled and thus equivalent to no cut at all.

Observable	Cut values
p_T^ℓ	$> \in \{0, 20, 40, 60, 80\}$
$p_T^{\text{jet}1}$	$> \in \{0, 75, 100, 125, 150, 175\}$
$p_T^{\text{jet}2}$	$> \in \{0, 50, 75, 100, 125\}$
ΔR_{jj}	$< \in \{0.8, 1.0, 1.2, 2.0, 1000\}$
N_{jet}	$\leq \in \{2, 3\}$
$N_{b\text{-jet}}$	$\leq \in \{0, 1, 100\}$
E_T^{miss}	$> \in \{0, 150, 160, 180, 200, 220\}$
E_T^{miss} significance	$> \in \{0, 5, 10, 15\}$
m_T	$> \in \{0, 140, 160, 180, 200, 220\}$
m_{eff}	$> \in \{0, 300, 400, 500, 600, 700\}$
m_{jj} lower	$> \in \{0, 60, 70, 75\}$
m_{jj} upper	$< \in \{85, 90, 100, 1000\}$
$\Delta\phi(E_T^{\text{miss}}, p_T^\ell)$	$< \in \{2.0, 2.4, 2.8, 3.15\}$

total MC background of less than 50%. Any cut combination not satisfying these criteria is not considered when building the ROC curve.

6.3.2 Optimisation results

As explained in section 6.2.1, after the N -dimensional scan, the cut combinations are sorted in bins of signal efficiency and only the candidates maximising the background rejection and satisfying the statistical criteria introduced in section 6.3.1 are chosen. In fig. 6.5, the expected significances for each signal point are plotted against the signal efficiencies. Different uncertainty scenarios are used in order to get a more complete picture of the possible sensitivity and help choosing a suitable cut combination for each scanned signal point.

The first significance value (shown in blue) is computed with MC statistical uncertainty only and therefore is useful in avoiding kinematic regimes with too low MC statistics.

The second significance value (red) is calculated with a systematic uncertainty of 30%, completely ignoring MC statistical uncertainties. This is useful for estimating the sensitivity of a potential future analysis with a given total uncertainty (typically in the range of 30%) where the estimation of problematic SM backgrounds is not done solely through MC but e.g. through a data-driven method, thereby at least partially avoiding high statistical uncertainties from poor MC simulations. As the MC simulation of the $W + \text{jets}$ background suffers from high statistical uncertainties even in regimes with relatively high statistics, it would be a candidate for a data-driven background estimation. This significance variation thus aims to give a sensitivity estimation in a potential future

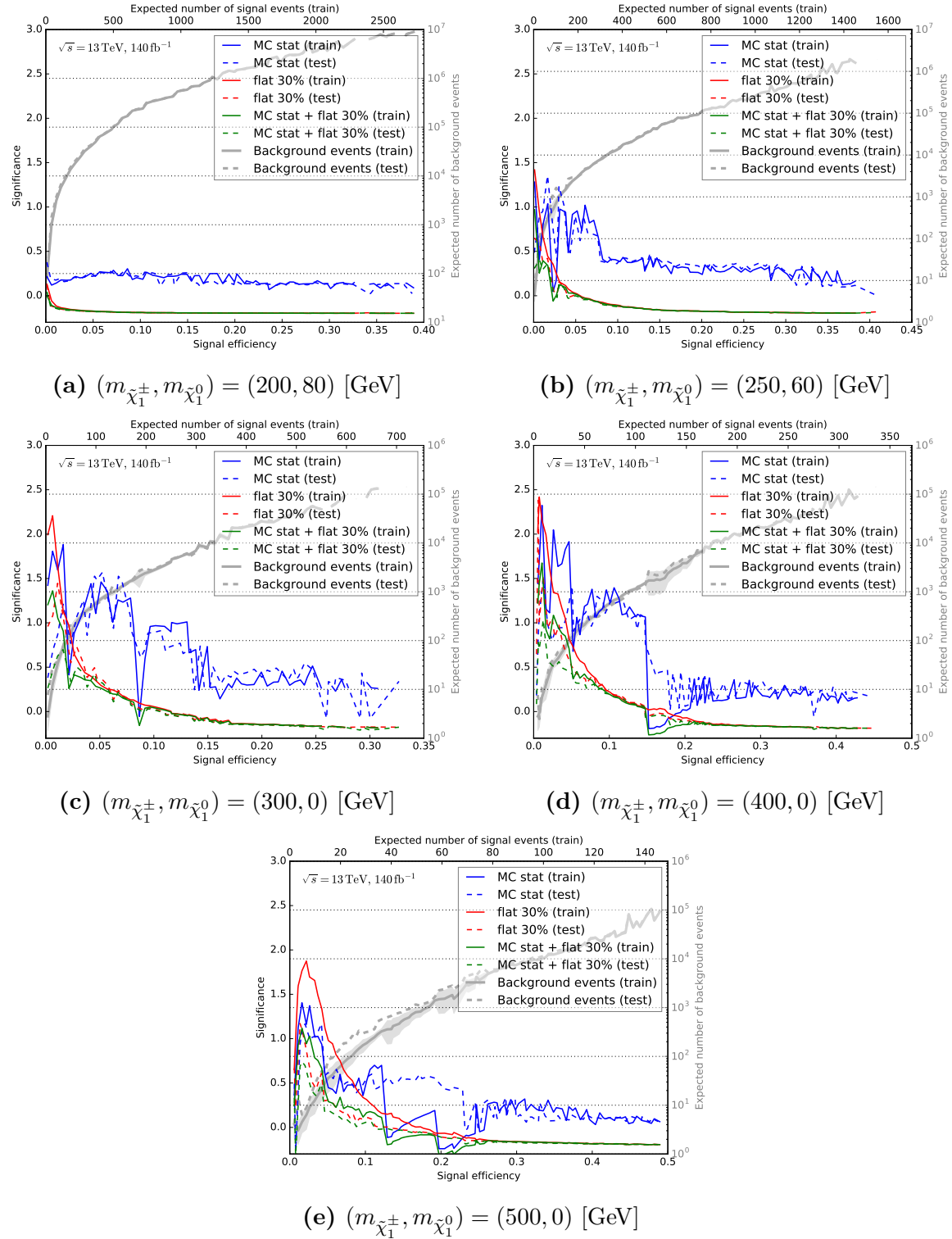


Figure 6.5: Results from the N -dimensional cut scan for each scanned signal point. Shown is the discovery significance in Gaussian standard deviations against the signal efficiency. Three different significance calculations differing in the considered uncertainties are used: (i) MC statistical uncertainty only (blue), (ii) 30% systematic uncertainties (red) and (iii) MC statistical uncertainty plus 30% systematic uncertainty (green). In grey, the expected number of weighted background events is shown. Results from training samples are drawn in solid lines and results from test samples in dashed lines.

Table 6.2: Chosen cut combination for the optimised benchmark signal points. Conservative cut combinations (in terms of statistical uncertainty) are chosen. A manual N-1 iteration further tunes and carefully tightens the cuts (see table 6.3). The significance Z is calculated with `BinomialExpZ` from the total background and signal yields passing the selection and includes a systematic uncertainty of 30%. The (200, 0) signal point is not included as no sensitivity at all is found for it.

Observable	Signal point with $(m_{\tilde{\chi}_1^\pm}, m_{\tilde{\chi}_1^0})$ in GeV			
	(250, 80)	(300, 0)	(400, 0)	(500, 0)
E_T^{miss} [GeV]	> 160	> 160	> 180	> 200
E_T^{miss} significance	> 10	> 5	> 5	> 10
m_T [GeV]	> 160	> 180	> 200	> 200
m_{eff} [GeV]	> 500	> 300	> 600	> 600
N_{jet}	2 – 3	2 – 3	2 – 3	2 – 3
$N_{b\text{-jet}}$	0	0 – 1	0 – 1	0 – 1
$p_T^{\text{jet}1}$ [GeV]	> 125	> 150	> 150	> 150
$p_T^{\text{jet}2}$ [GeV]	> 100	> 100	> 100	> 100
p_T^ℓ [GeV]	> 0	> 0	> 0	> 0
ΔR_{jj}	< 2.0	< 0.8	< 1.0	< 0.8
m_{jj} [GeV]	75 – 90	75 – 90	75 – 90	75 – 90
$\Delta\phi(E_T^{\text{miss}}, p_T^\ell)$	< 2.4	< 2.0	< 2.8	< 2.4
Z [σ]	0.53	1.97	1.52	1.69

analysis, where the $W + \text{jets}$ statistical uncertainties can be slightly reduced through alternative estimation techniques or improved MC statistics.

The third and last significance variation (green) uses MC statistical uncertainties together with a systematic uncertainty of 30% (added quadratically), thereby forming a worst case scenario where the statistics issues with $W + \text{jets}$ are not resolved and systematic uncertainties are taken into account. Hence, this last variation provides an estimation for a lower bound of the sensitivity that could be achieved even if no further effort is invested in alternative background estimation methods[†].

In addition to the different significances, the expected weighted background yields together with the statistical uncertainty are shown (in grey). This is useful to cross-check the background yields for different cut combinations. Each line in fig. 6.5 is drawn for both the training and test samples. As can be seen in fig. 6.5(a), no sensitivity at all is expected for the (200, 0) signal point. In the following, this benchmark point is therefore omitted.

The resulting cut combination for each remaining signal point is chosen by picking a cut candidate from a signal efficiency bin that constitutes a compromise between the two first significance variations. This is sensible, since the significance value only taking 30% systematic uncertainties into account is agnostic to high statistical uncertainties

[†] Given that a signal region with a systematic uncertainty of around 30% is used.

Table 6.3: Cut combinations optimised through a round of N-1 plots based on the cut combinations listed in table 6.2. The cuts on m_{eff} , ΔR_{jj} and the E_T^{miss} significance are removed since they are found not to contribute noticeably to the significance (within the previously defined statistical requirements) and/or are already largely covered by cuts on other, correlated observables. The significance Z includes a systematic uncertainty of 30%.

Observable	Signal point with $(m_{\tilde{\chi}_1^\pm}, m_{\tilde{\chi}_1^0})$ in GeV			
	(250, 80)	(300, 0)	(400, 0)	(500, 0)
E_T^{miss} [GeV]	> 160	> 180	> 200	> 220
m_T [GeV]	> 160	> 180	> 200	> 220
N_{jet}	2	2 – 3	2 – 3	2 – 3
$N_{b\text{-jet}}$	0	0 – 1	0 – 1	0 – 1
$p_T^{\text{jet}1}$ [GeV]	> 150	> 150	> 150	> 150
$p_T^{\text{jet}2}$ [GeV]	> 100	> 100	> 100	> 100
m_{jj} [GeV]	75 – 90	75 – 90	75 – 90	75 – 90
$\Delta\phi(E_T^{\text{miss}}, \mathbf{p}_T^\ell)$	< 2.0	< 2.0	< 2.4	< 2.4
Z [σ]	1.40	2.15	1.98	1.58

(apart from the statistics constraints applied during the optimisation itself), while the significance value only taking into account MC statistical uncertainties does not properly reflect analysis scenarios where MC statistics could be improved and/or other background estimation methods are employed and systematic uncertainties also need to be considered.

By selecting a compromise signal efficiency bin in terms of background statistics and significance value in fig. 6.5, the cut combinations in table 6.2 are chosen. In general, the optimisation only reaches relatively low significances of up to roughly $Z = 2$, even though optimising for 140 fb^{-1} of data. Since the cut combinations from the N -dimensional scan have been chosen conservatively in terms of statistics, a second round of optimisation through N-1 plots is performed. This allows to manually fine-tune and tighten the cuts while ensuring that no kinematic region with too low statistics is selected.

A complete set of all the N-1 plots for each signal point and each observable is listed in appendix A.1. These are used to further tune requirements or even remove some of the cuts that do not noticeably contribute to an increase in sensitivity. Performing this manual optimisation yields the N-1-optimised cuts and significance values listed in table 6.3. The applied changes are the following. The E_T^{miss} significance requirement is removed from the cut combinations for each signal point since it is found not to contribute to a higher significance value and is largely redundant to the cut on E_T^{miss} . The same holds for the m_{eff} requirement. As the various benchmark signal points tend to favour different m_{eff} cuts due to varying m_{eff} shapes (especially visible in fig. 6.2(d)), the removal of the requirement especially also allows the m_{eff} distribution to be used in a shape fit in section 6.5. Finally, the cut on ΔR_{jj} is also removed since events with low ΔR_{jj} are already selected through other, correlated cuts. N-1 plots of the cut combinations obtained through the manual N-1-optimisation are shown in figs. 6.6 to 6.9.

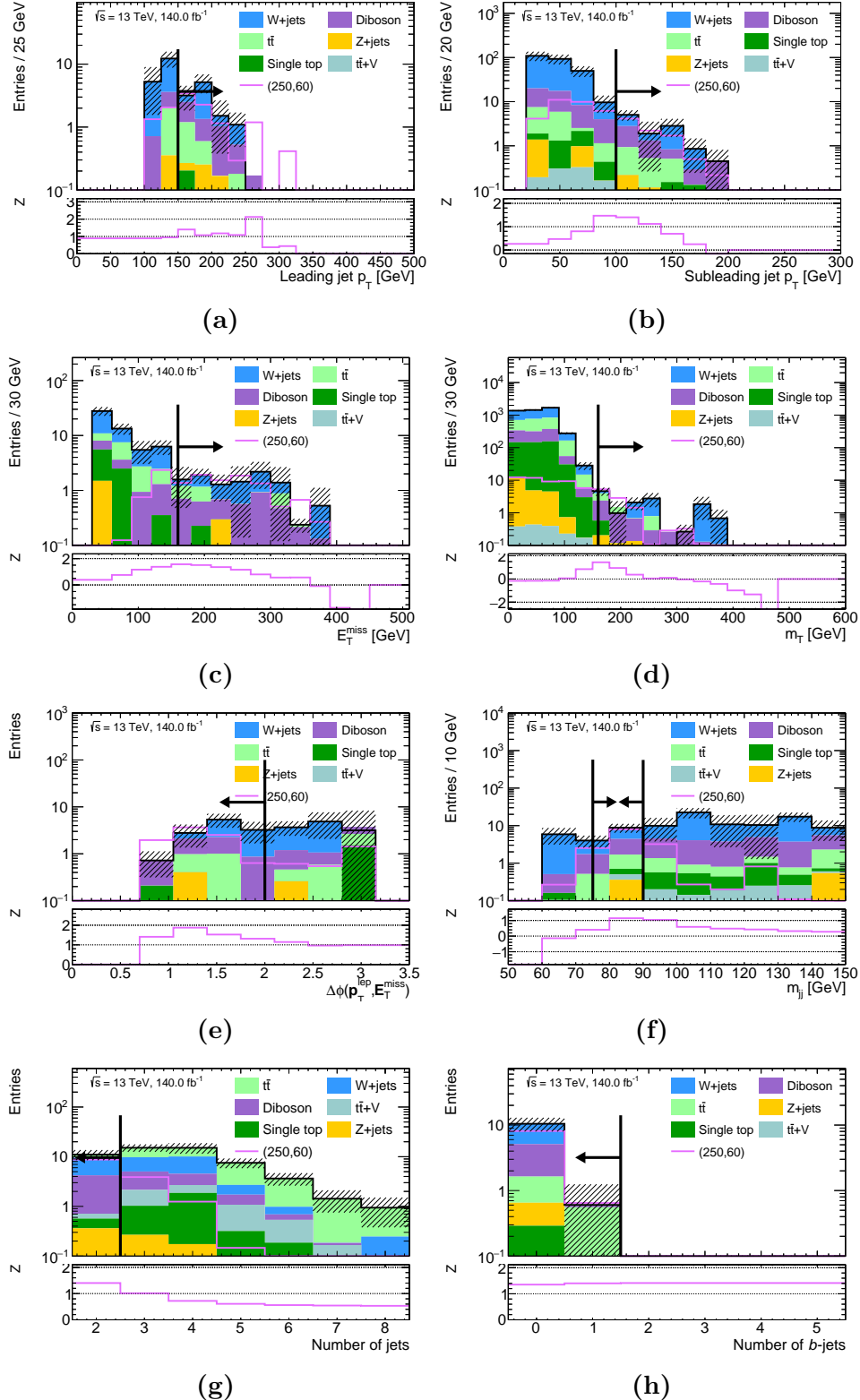


Figure 6.6: N-1 plots for the tuned cuts on the (250, 60) benchmark point. The significance in the lower pad is obtained by summing up all the events in the direction of the cut arrow and includes 30% uncertainty. In fig. (f), both the upper and lower requirement are shown, but the significance in the lower pad refers to scanning only the upper requirement.

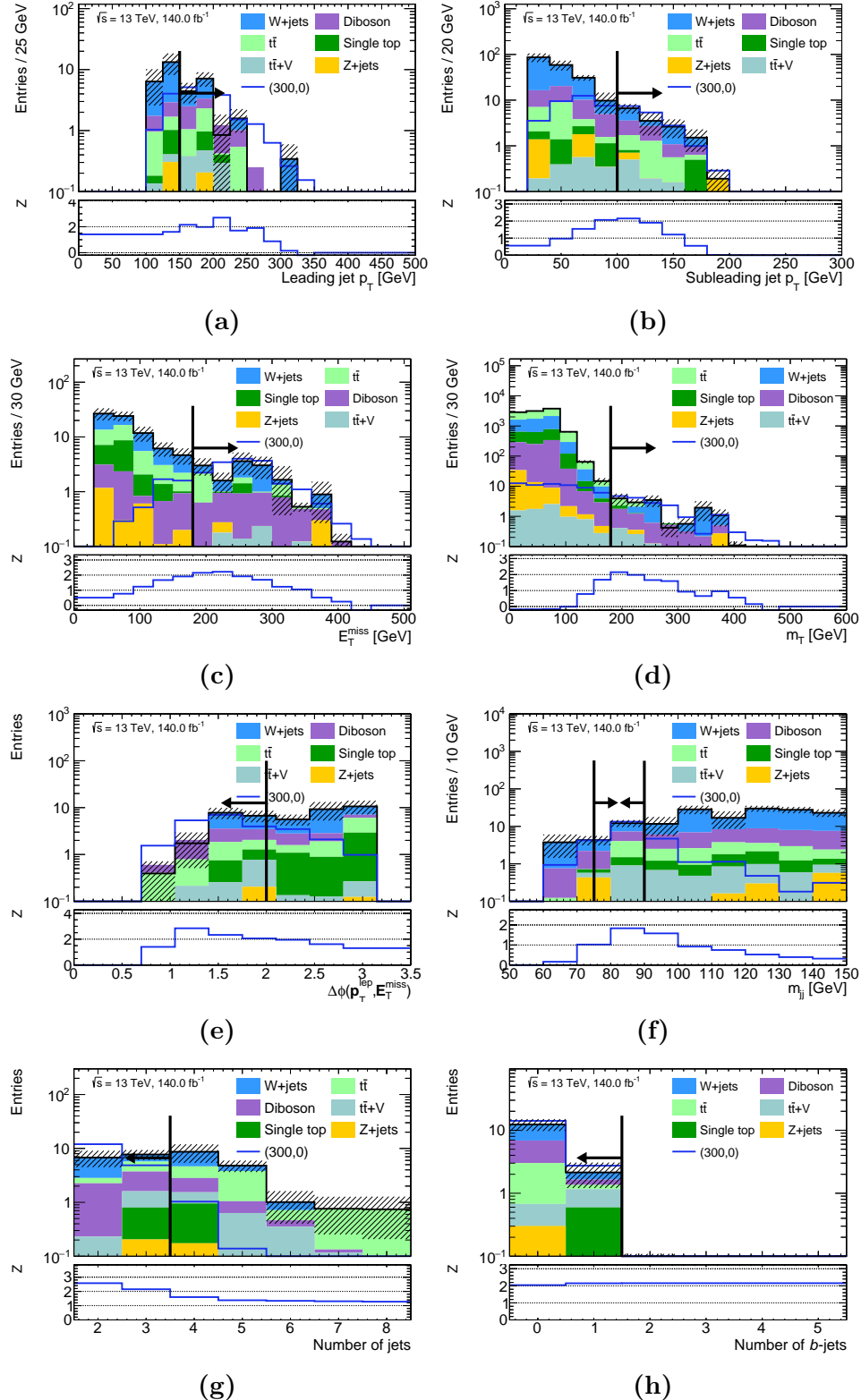


Figure 6.7: N-1 plots for the tuned cuts on the (300, 0) benchmark point. The significance in the lower pad is obtained by summing up all the events in the direction of the cut arrow and includes 30% uncertainty. In fig. (f), both the upper and lower requirement are shown, but the significance in the lower pad refers to scanning only the upper requirement.

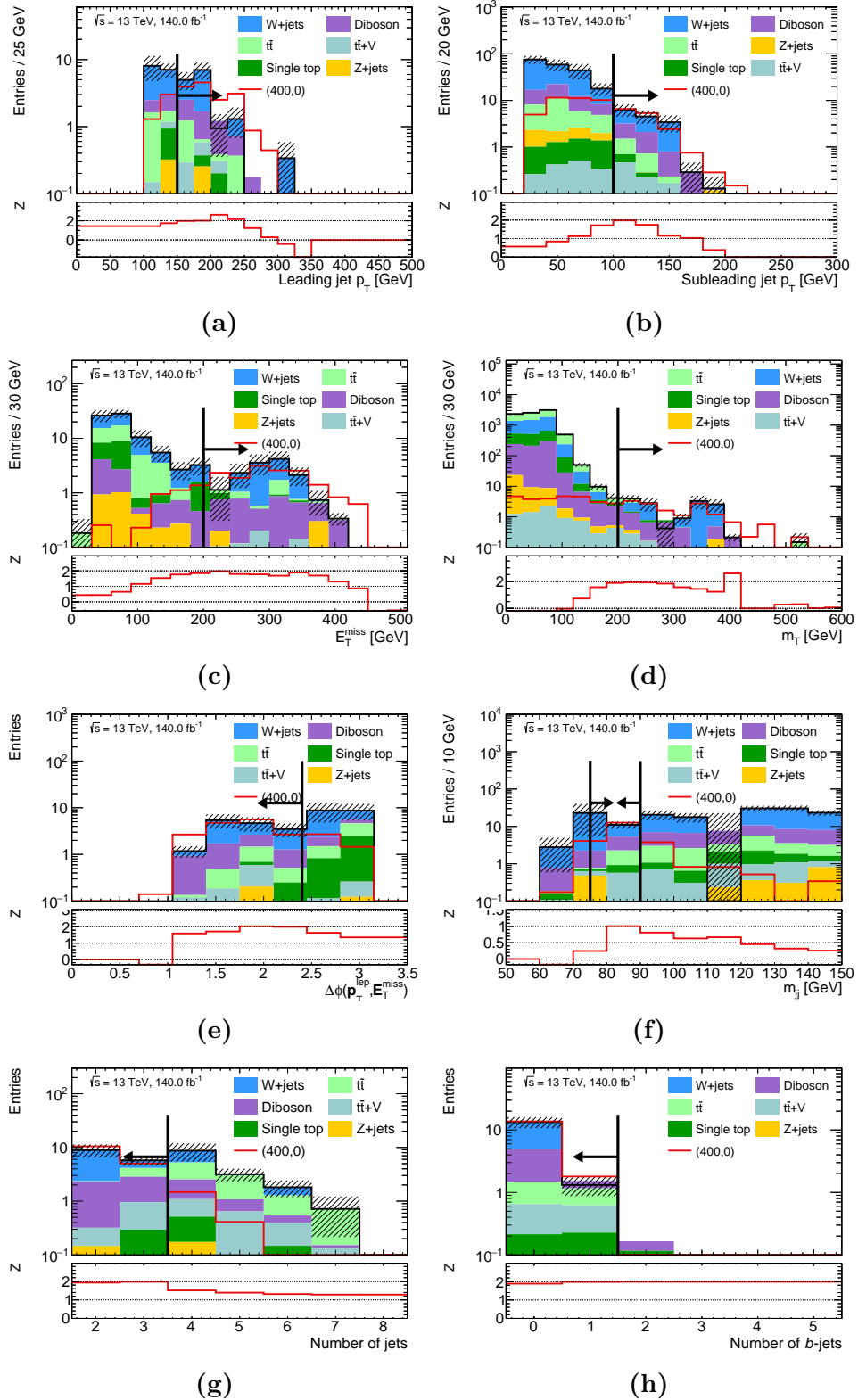


Figure 6.8: N-1 plots for the tuned cuts on the (400, 0) benchmark point. The significance in the lower pad is obtained by summing up all the events in the direction of the cut arrow and includes 30% uncertainty. In fig. (f), both the upper and lower requirement are shown, but the significance in the lower pad refers to scanning only the upper requirement.

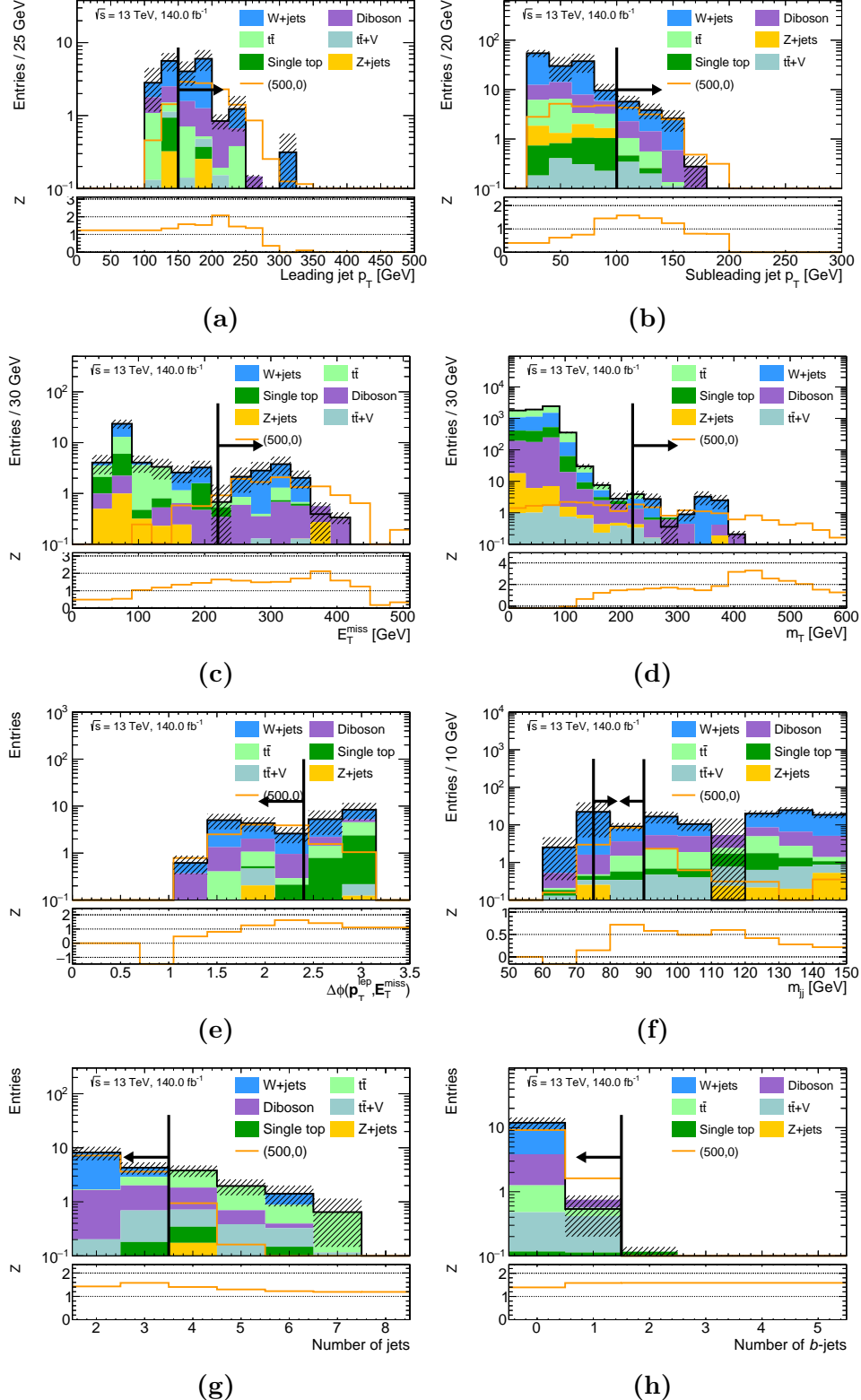


Figure 6.9: N-1 plots for the tuned cuts on the (500, 0) benchmark point. The significance in the lower pad is obtained by summing up all the events in the direction of the cut arrow and includes 30% uncertainty. In fig. (f), both the upper and lower requirement are shown, but the significance in the lower pad refers to scanning only the upper requirement.

Table 6.4: Preliminary definition of a signal region for the WW model. The different cut values are obtained by examining N-1 plots of the cuts obtained in table 6.2.

Observable	SR
E_T^{miss} [GeV]	> 200
m_T [GeV]	> 200
$p_T^{\text{jet}1}$ [GeV]	> 150
$p_T^{\text{jet}2}$ [GeV]	> 100
N_{jets}	$2 - 3$
$N_{b\text{-jets}}$	$0 - 1$
m_{jj}	$75 - 90$
$\Delta\phi(E_T^{\text{miss}}, p_T^\ell)$	< 2.4

6.4 Preliminary signal region definition

By comparing the cuts on the different observables for the various benchmark points obtained in table 6.3, an attempt to consolidate them into a single signal region (SR) can be made. As the remaining low-mass point with $m(\tilde{\chi}_1^\pm) = 250$ GeV and $m(\tilde{\chi}_1^0) = 60$ GeV reaches a considerably lower significance than the higher-mass and less compressed points, the main focus for a signal region in this work lies on the high-mass points[†]. For most of the observables, a compromise is straightforward to choose since similar cut values are favoured. For the cuts on E_T^{miss} and m_T , a value of 200 GeV is chosen as a compromise between the low- and high-mass benchmark points. The requirements defining the preliminary signal region are given in table 6.4. N-1 plots are shown in fig. 6.10.

Table 6.5 summarises the expected event yields and statistical uncertainties for each of the considered backgrounds and the benchmark signal points in the signal region for 140 fb^{-1} . The most dominant background in terms of expected number of events is by far $W + \text{jets}$, followed by diboson and $t\bar{t}$ production. The significances given in table 6.5 are calculated with an uncertainty of 30%. Although the statistical uncertainty of $W + \text{jets}$ alone is, with 31%, slightly higher than 30%, this value is motivated by the anticipation that, in a future analysis, $W + \text{jets}$ is not only estimated through MC but e.g. data-driven methods. This would likely result in a reduction of the statistical uncertainty and yield a more reliable estimation of the $W + \text{jets}$ background. Additionally, slightly more MC statistics will be available at a later stage of Run-2, further improving the reliability of the background prediction.

The significances that are achieved with this relatively simple cut-and-count[§] approach reach up to $Z = 2$ for massless LSPs. Hence, some of the signal points with very low LSP masses lie slightly above the $Z = 1.64$ limit (necessary for exclusion) and could

[†] In a full analysis, multiple signal regions could of course target different kinematic regimes.

[§] The term *cut-and-count* refers to the fact that the significance value is computed by adding up all events surviving the SR requirements in a single SR bin.

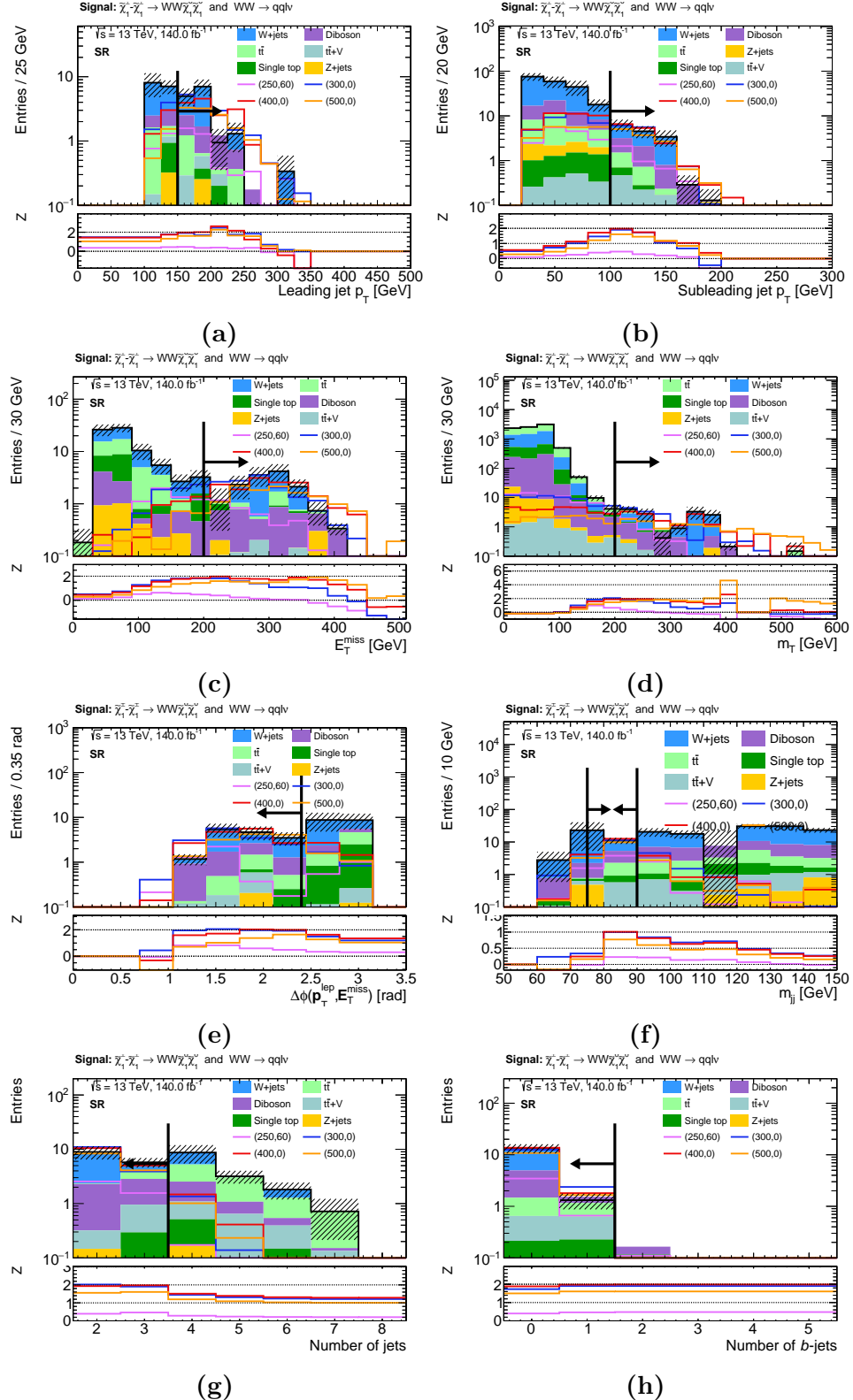


Figure 6.10: N-1 plots for the preliminary signal region. The significance in the lower pad is obtained by summing up all the events in the direction of the cut arrow and includes 30% uncertainty. In fig. (f), both the upper and lower requirement are shown, but the significance in the lower pad refers to scanning only the upper requirement.

Table 6.5: Background and signal yields in the signal region for 140 fb^{-1} as expected from MC. Stated are the expected number of weighted events N_{exp} , the statistical uncertainty δN_{stat} , relative process contribution b_{rel} , the number of raw MC events N_{MC} and the expected signal significance. Significances of up to roughly $Z = 2$ are achieved, calculated with an uncertainty of 30%.

Process	$N_{\text{exp}} \pm \delta N_{\text{stat}}$	b_{rel}	N_{MC}	$Z [\sigma]$
$W + \text{jets}$	8.17 ± 2.56	55.7%	23	–
Diboson	3.87 ± 0.33	26.4%	292	–
$t\bar{t}$	1.35 ± 0.60	9.2%	18	–
$t\bar{t} + V$	0.83 ± 0.16	5.7%	96	–
Single top	0.35 ± 0.14	2.4%	6	–
$Z + \text{jets}$	0.09 ± 0.35	0.6%	4	–
Total background	14.67 ± 2.68	100%	439	–
(250, 60)	4.12 ± 0.86	100%	26	0.46
(300, 0)	14.91 ± 1.46	100%	116	1.91
(400, 0)	15.51 ± 1.32	100%	170	1.98
(500, 0)	12.45 ± 0.85	100%	258	1.61

thus potentially be excluded in a future analysis. However, none of them reach the significance levels needed for discovery. Furthermore, as the LSP mass increases, the reached significance rapidly drops, showing that this signal region is only sensitive to relatively low LSP masses.

6.5 Multi-bin approach

6.5.1 Method

Instead of only evaluating the significance of a given signal model in a single signal region bin, i.e. with a simple cut-and-count approach, it is possible to extract more information about the distributions through the definition of multiple signal region bins in dependence of a discriminating variable. Simultaneously fitting multiple signal region bins (all orthogonal to each other) allows to, for example, explicitly consider the varying shapes for signal and background distributions. Additionally, as seen in the previous section, a single cut-and-count signal region cannot be sensitive to all possible kinematic scenarios or even completely different decay chains. A multi-bin fit, however, in principle allows to choose the binning in such a way that the sensitivity to other decay chains or kinematic scenarios can be increased. As a result, multi-bin fits generally result in higher sensitivities than a simple cut-and-count approach. In the following, a simultaneous fit in multiple signal region bins will be referred to as a *shape fit*.

Table 6.6: Definitions of loosened signal regions, used for shape fit applications. The increased statistics are necessary to provide a more reliable prediction of the shapes of the m_{jj} , m_{eff} , m_{T} and $E_{\text{T}}^{\text{miss}}$ distributions. Multiple different loose SR candidates are tested for each observable and the candidate yielding the best results is chosen. A hyphen indicates that no cut is applied. Requirements written in the middle of the table are applied to all loose SRs.

Observable	loose SR (m_{jj})	loose SR (m_{eff})	loose SR (m_{T})	loose SR ($E_{\text{T}}^{\text{miss}}$)
$E_{\text{T}}^{\text{miss}}$ [GeV]	> 160	> 160	> 160	—
m_{T} [GeV]	> 180	> 180	—	> 180
$p_{\text{T}}^{\text{jet}1}$ [GeV]	> 150	> 100	> 100	> 150
$p_{\text{T}}^{\text{jet}2}$ [GeV]			> 100	
N_{jets}			2 – 3	
$N_{b\text{-jets}}$			0 – 1	
m_{jj} [GeV]	—	75 – 90	75 – 90	75 – 90
$\Delta\phi(\mathbf{E}_{\text{T}}^{\text{miss}}, \mathbf{p}_{\text{T}}^{\ell})$ [rad]			< 2.4	

The technical implementation of the shape fits presented in this section is done through `HistFitter` [79], a software package wrapping around the frameworks `HistFactory` [80] and `RooStats` [70], which are based on `RooFit` [81] and `ROOT` [82, 83]. `HistFitter` conveniently interfaces methods to perform binned likelihood fits as well as their statistical interpretation and is the standard statistical tool employed in searches for SUSY at ATLAS.

As a shape fit needs a reliable background estimation in multiple bins (as opposed to a single bin in a cut-and-count approach), it is necessary to slightly loosen some of the cuts defining the SR from section 6.4 before binning the distribution of the observable used for the multi-bin fit. In the following, shape fits on four different discriminative observables are investigated: m_{jj} , m_{eff} , m_{T} and $E_{\text{T}}^{\text{miss}}$. By carefully comparing with fig. 6.10, and testing multiple different loose signal region candidates for each observable, the loose SRs in table 6.6 are selected. For each observable, the loose SR in table 6.6 represents the tested SR candidate yielding the best results in a shape fit.

6.5.2 Setups and results

Figures 6.11 to 6.13 illustrate the shape fit setups in each distribution for the various benchmark signal points before simultaneously fitting all bins in each setup in a model-dependent[†] fit. In each setup, the signal events are stacked on top of the total background and the data points are ‘fake’ data used in the fit. In order to compute a discovery significance, the discovery test statistic built from the profile likelihood ratio, introduced in section 5.1, is used. In each setup, the statistical uncertainty from the MC samples as

[†] A *model-dependent fit* is used to either derive exclusion limits on a given signal model or quantify the properties of an excess over the number of events given by the background-only hypothesis [79].

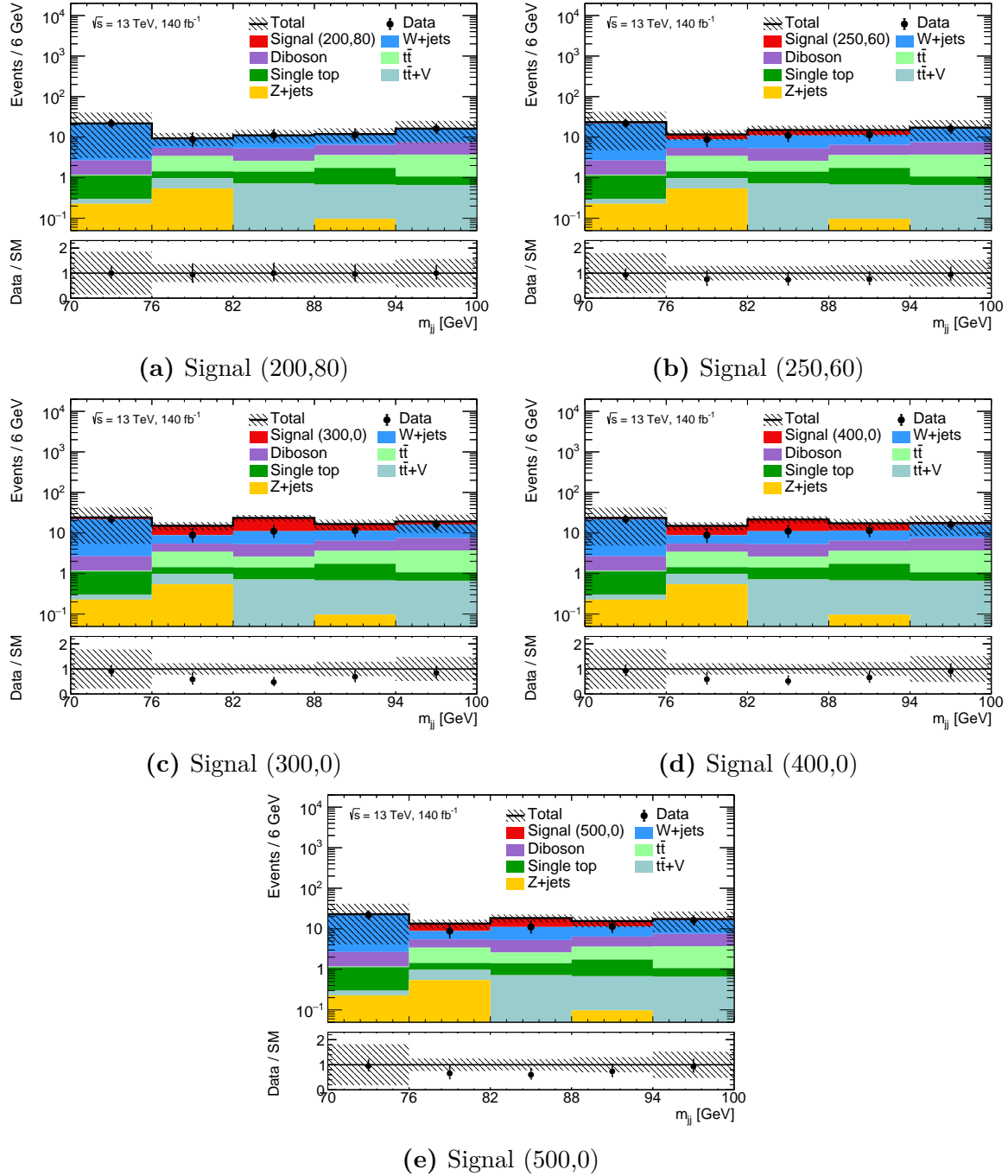


Figure 6.11: Setup of a shape fit in m_{jj} in the loose SR. The setup defines five bins in m_{jj} from 70 GeV to 100 GeV with a width of 6 GeV each, and includes MC statistical uncertainty as well as 30% overall systematic uncertainty, uncorrelated over all bins. All five bins are fit simultaneously in a model-dependent fit. The data points are ‘fake’ data used in the fit. In each plot, the benchmark signal point considered in the fit is stacked on top of the total background.

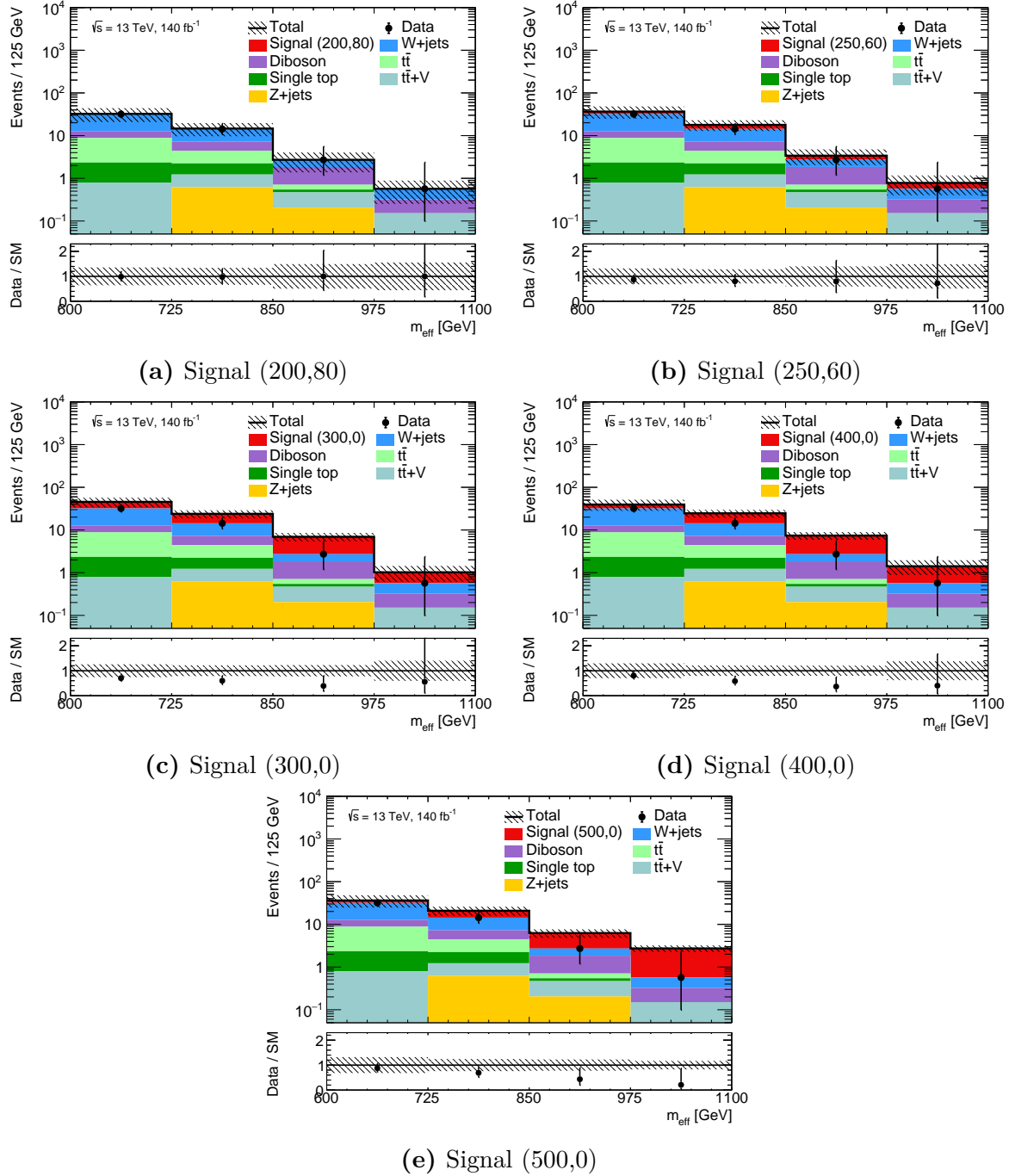


Figure 6.12: Setup of a shape fit in m_{eff} in the loose SR. The setup defines four bins in m_{eff} from 600 GeV to 1100 GeV with a width of 125 GeV each, and includes MC statistical uncertainty as well as 30% overall systematic uncertainty. Overflow is included in the last bin. All four bins are fitted simultaneously in a model-dependent fit. The data points are ‘fake’ data used in the fit. In each plot, the benchmark signal point considered in the fit is stacked on top of the total background.

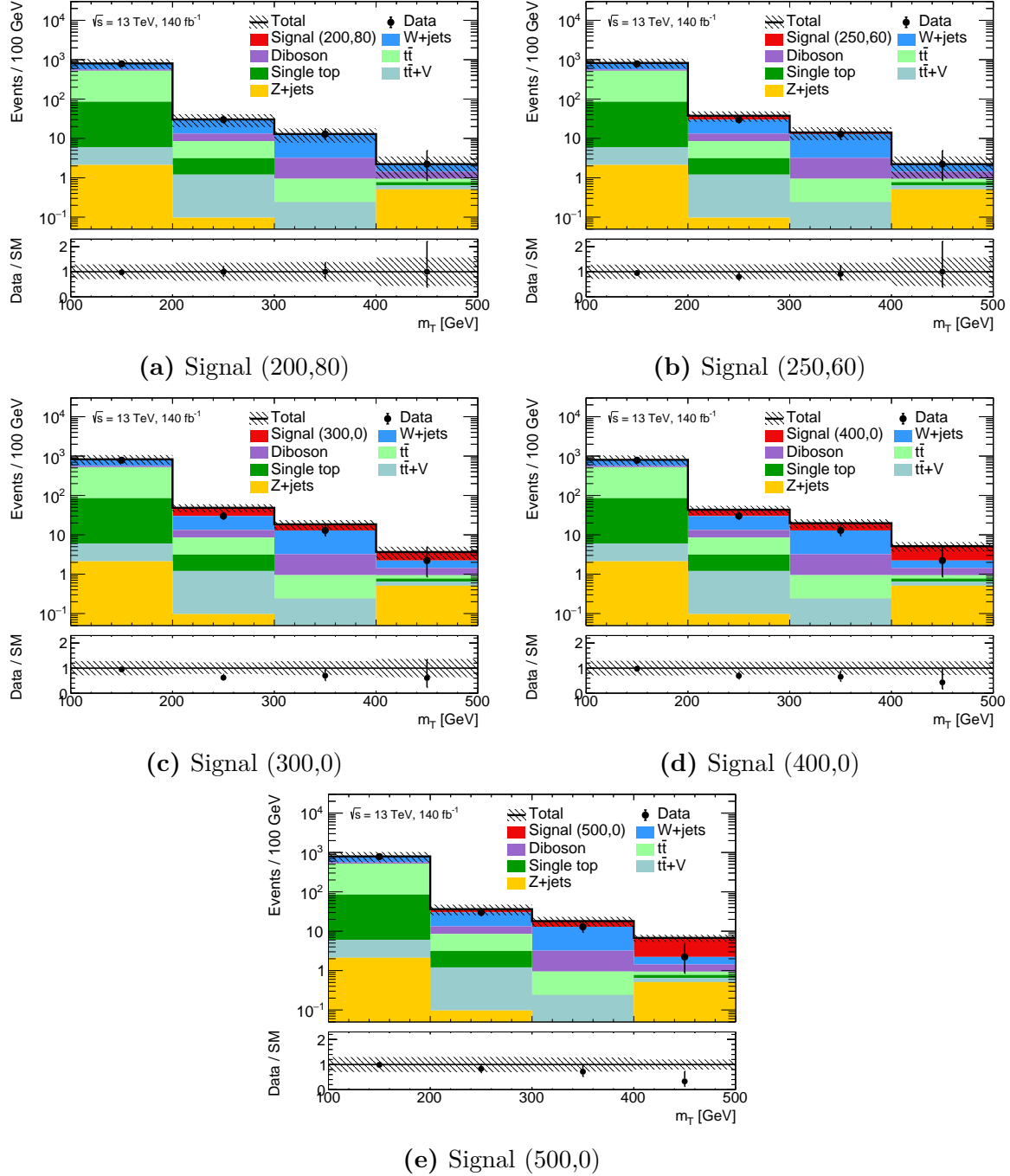


Figure 6.13: Setup of a shape fit in m_T in the loose SR. The setup defines four bins in m_T from 100 GeV to 500 GeV with a width of 100 GeV each, and includes MC statistical uncertainty as well as 30% overall systematic uncertainty. Overflow is included in the last bin. All four bins are fitted simultaneously in a model-dependent fit. The data points are ‘fake’ data used in the fit. In each plot, the benchmark signal point considered in the fit is stacked on top of the total background.

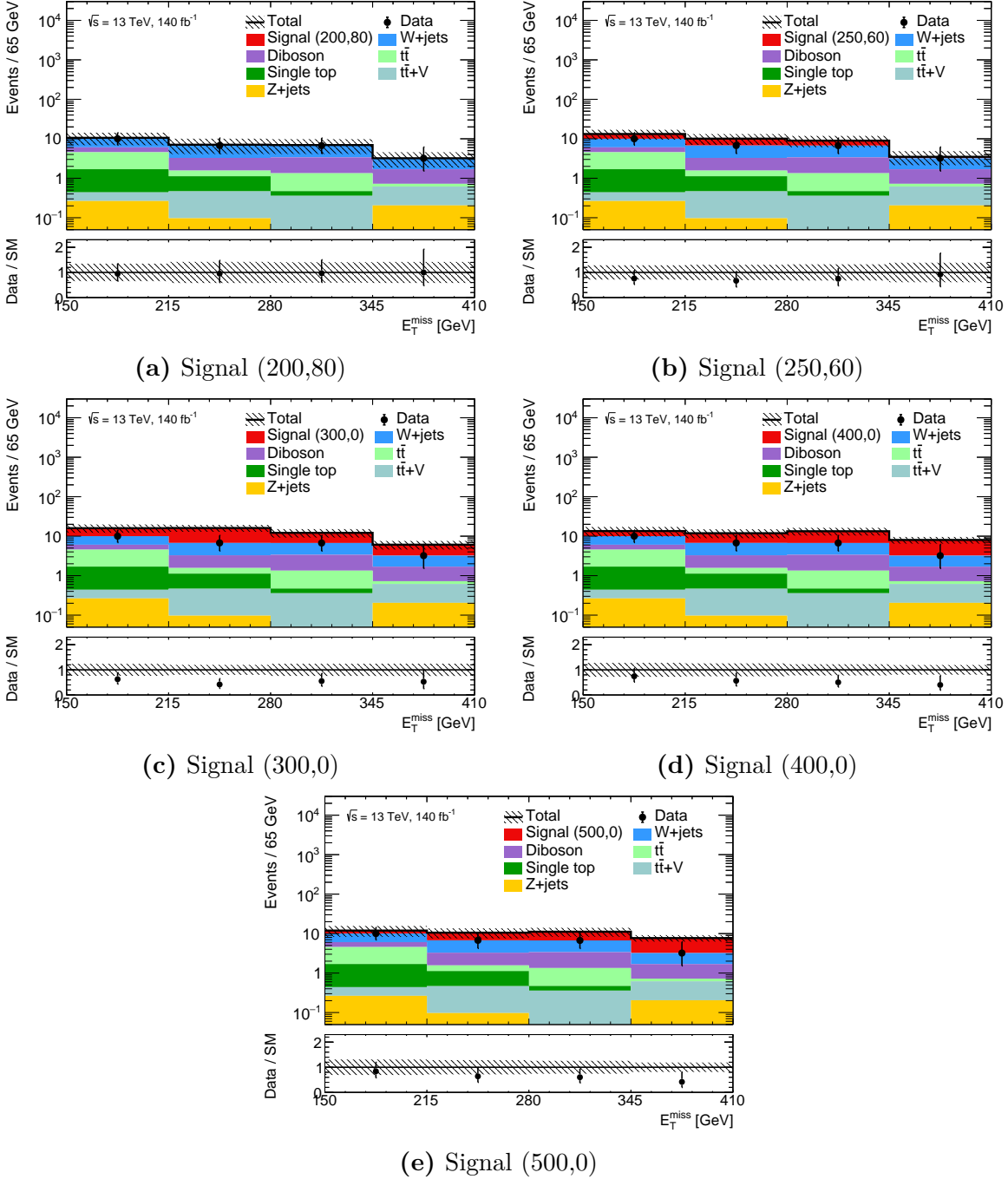


Figure 6.14: Setup of a shape fit in E_T^{miss} in the loose SR. The setup defines four bins in E_T^{miss} from 150 GeV to 410 GeV with a width of 65 GeV each, and includes MC statistical uncertainty as well as 30% overall systematic uncertainty. Overflow is included in the last bin. All four bins are fitted simultaneously in a model-dependent fit. The data points are ‘fake’ data used in the fit. In each plot, the benchmark signal point considered in the fit is stacked on top of the total background.

Table 6.7: Results from the different investigated shape fit setups. In every setup MC statistical uncertainty and a 30% overall systematic uncertainty are considered.

Observable	Binning	Discovery significance [σ]				
		(200, 80)	(250, 60)	(300, 0)	(400, 0)	(500, 0)
m_{jj}	5 bins $\in [70, 100]$	0.15	0.92	2.24	2.02	1.50
m_{eff}	3 bins $\in [600, 975]$	0.06	0.61	2.00	2.32	2.46
	+ $[>975]$					
m_T	3 bins $\in [100, 500]$	0.11	0.78	2.47	2.59	2.63
	+ $[>500]$					
E_T^{miss}	3 bins $\in [150, 345]$	0.14	0.98	2.29	2.25	1.97
	+ $[>345]$					

well as a 30% overall systematic uncertainty on the background is taken into account. In `HistFitter`, this is introduced through a systematic of the type `overallSys` [79].

The achieved discovery significances for each benchmark point in every investigated shape fit setup is shown in table 6.7. For high-mass points, the shape fit on m_{jj} yields the lowest significances, while the shape fit on m_T generally outperforms other setups. The results from fits on the m_{eff} - and E_T^{miss} -shape lie more or less between the fits in m_{jj} and m_T . Although the overall sensitivity is still relatively low, a significant increase compared to the cut-and-count approach in section 6.4 is observed in the m_T shape fit, especially considering that both MC statistical and 30% overall systematic uncertainty are considered. Although no signal point exceeds the 3σ limit needed to claim evidence for SUSY in case of an excess, several signal points exceed the 1.64σ limit needed for exclusion in case no excess in data is seen.

Figure 6.15 shows an interpolation of the achieved significances in the $\tilde{\chi}_1^\pm - \tilde{\chi}_1^0$ mass plane, using the m_T shape fit results from the five benchmark signal points. The interpolation is performed with Delaunay triangles, implemented with `ROOT` and shows a rough estimation of the achievable sensitivity throughout a small portion of the $\tilde{\chi}_1^\pm - \tilde{\chi}_1^0$ mass grid. With this fit setup in the m_T distribution, $\tilde{\chi}_1^\pm$ masses of up to 500 GeV and $\tilde{\chi}_1^0$ masses of up to roughly 40 GeV could potentially be excluded. Section 6.7 further discusses these results.

6.6 Multivariate approach

Another method that could be able to successfully discriminate signal against background events is a multivariate analysis. In this section, the sensitivity results using machine learning algorithms, especially multilayer perceptrons (MLPs) [75, 76], a special form of neural nets, are presented. Machine learning is a promising area in the artificial intelligence domain and is successfully used to let machines learn patterns and structures in data. In this work, MLPs are used to differentiate background from signal events with

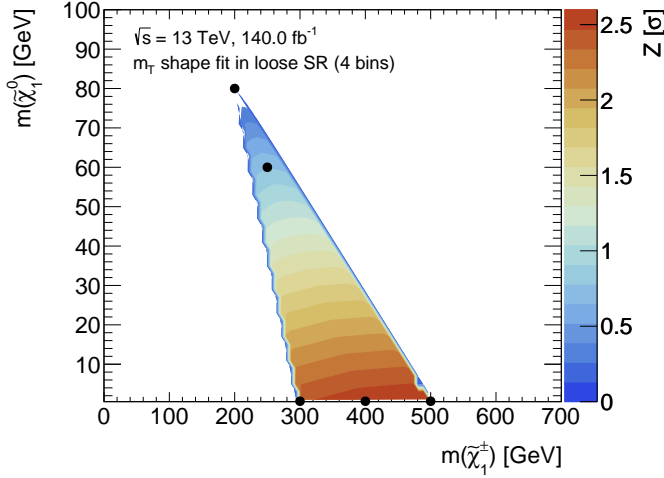


Figure 6.15: Interpolation of the significances achieved with a shape fit in m_T . Since only five benchmark points are available, the interpolated space in the $m(\tilde{\chi}_1^\pm)$ - $m(\tilde{\chi}_1^0)$ grid is rather small. The interpolation is done through a Delaunay triangulation, implemented in ROOT. The input points are shown as black dots.

the hope of at least partially circumventing the MC statistics issues appearing in many cut-based approaches.

6.6.1 General method and technical details

A multilayer perceptron (MLP) is a class of artificial neural networks. Neural networks are based on a collection of connected nodes, called *neurons*, that are ordered in multiple layers and designed to loosely model the neurons of the brain. The connections between the neurons are similar to synapses in the brain in the sense that they transmit information between the connected neurons. Each connection has an individual *weight* parameter indicating the strength of the connection. Additionally, neurons have a *threshold* (or *bias*) parameter that needs to be exceeded for the neuron to become active and transmit information. MLPs are *feedforward* neural nets, meaning that information can only travel in the forward direction[†]. Information is introduced in the MLP through an input layer and travels through multiple *hidden* layers before reaching an output layer where the final output score is determined. An *activation function* dictates how each neuron treats information before transmitting it to each connected neuron in the next layer.

As the target of the MLP in this work is to distinguish between background and signal events[§], a binary classification is employed. Therefore, the output layer, consisting of

[†] *Forward* meaning here in the direction from input to output.

[§] It does not matter which background process an event belongs to as long as it is correctly classified as being a background event.

only a single neuron, uses a sigmoid as activation function,

$$\sigma(x) = \frac{1}{1 + e^{-x}}. \quad (6.5)$$

The sigmoid has a lower bound at 0 for $x \rightarrow -\infty$ and an upper bound at 1 for $x \rightarrow \infty$. Hence, the output neuron associates a continuous score between 0 and 1 to each event, with 0 being background and 1 signal processes. The neurons in the other layers use the (noiseless) rectified linear unit function (ReLU) as activation function,

$$f(x) = \begin{cases} 0, & x < 0, \\ x, & x \geq 0. \end{cases} \quad (6.6)$$

The MLP used in the following, is trained with a *supervised learning* method, which means that labelled data is used to train the neural net. Labelled data is built of pairs of data consisting of an input object and a desired output value, used to give feedback to the algorithm during the training process. This is achieved through a procedure called *backpropagation* [84]. The used measure indicating how well the algorithm learns from the training data is the *loss function*, a quantisation of the difference between the desired output and the output computed by the algorithm. The *binary cross entropy* is used as loss function in this work. The training effectively consists of finding a global minimum in the multidimensional distribution of the loss function by iteratively adjusting the thresholds and weights of each neuron in such a way that a descent in the loss function gradient takes place. The algorithm responsible for the gradient descent is called *optimiser*. In the following studies, the *Adam* optimiser [85] is used. The implementation [86] of the MLP is done with the *Keras* [87] framework using *TensorFlow* [88] as backend.

The performance of the different setups is mainly assessed by comparing their respective receiver operating characteristic (ROC) curves. In a ROC curve, the background rejection is plotted against the signal efficiency. The higher the background rejection is throughout the entire range of signal efficiency, the better is the performance of the respective setup. Thus, the area under the ROC curve (AUC) is a good indicator for how well a setup is able to classify signal and background events. An AUC of 1.0 equals perfect classification while an AUC of 0.5 is no better than luck. Since not all signal efficiency and background rejection values are of interest, it is also important to not only compare the AUC but also in which signal efficiency range a specific setup outperforms in terms of background rejection.

6.6.2 Input data

The data used as input for the neural net are the MC samples for the different background processes considered previously as well as the (400, 0) signal point. In general, machine learning algorithms require high statistics samples to infer patterns and structures from data. While the number of unweighted MC events is of the order of 10^6 - 10^7 for background

events, the signal sample statistics are often only of the order of 10^3 events, which is not enough for neural nets to learn the distinct characteristics of signal events. Furthermore, producing several millions of events at full-reconstruction level (reco) takes a significant amount of CPU time, even if using AtlFast-II, and is thus why it is not practicable to produce enough signal MC statistics at full-reconstruction level for machine learning studies. Therefore, in the following, a high statistics signal sample at *truth level* — a sample missing the full detector simulation — is used to train the neural nets. Truth samples can be easily generated but have the disadvantage of not accurately simulating data due to the missing detector simulation. In order to reduce the mismodelings, a dedicated approximation technique is used, smearing the distributions of the energies and momenta of the physics objects used and applying reconstruction and identification efficiencies binned in η and ϕ . This smearing technique is implemented in the software framework `SimpleAnalysis` [89] and is explained in detail in section 7.1.1, where it will be heavily reused. Testing the neural net is done on the low statistics sample with fully reconstructed events. For the background, both training and testing use fully reconstructed samples as enough MC background statistics are available.

A summary of plots comparing the agreement between the truth and full-reconstruction signal samples is given in appendix A.2. In general the observables used in the following for training and evaluating the MLP show a good agreement between full-reconstruction and smeared truth samples.

6.6.3 Setup

A range of different setups and architectures are tested. The results from previous studies [90, 91] using MLPs trained on truth-level events are partially used to choose some of the setups to be tested. The performance of the different setups is assessed by comparing their respective ROC curves. In order to avoid biases, only events not used for training are considered for drawing the different curves. It is worth noting that not the entire ROC curve is of interest. For the considered WW signal model, in order to achieve sensitivity, the previous results in this chapter have shown that the background efficiency needs to be roughly of the order of 10^{-4} while the signal efficiency should still be high enough, i.e. in the range of 0.1 or higher.

Preselection cut

With a few million truth level signal events available, it is challenging to load all available background and signal events into memory. Instead of randomly picking a subset of events for both signal and background, different preselection cuts are studied. The advantage of a preselection cut is that it not only reduces the memory load but also already favours an interesting kinematic region. Figure 6.16 shows the impact of different preselection cuts. It can be seen that in the relevant regions of the ROC curves, a preselection on $m_T > 110\text{ GeV}$ slightly outperforms all the other tested preselection cuts. In the

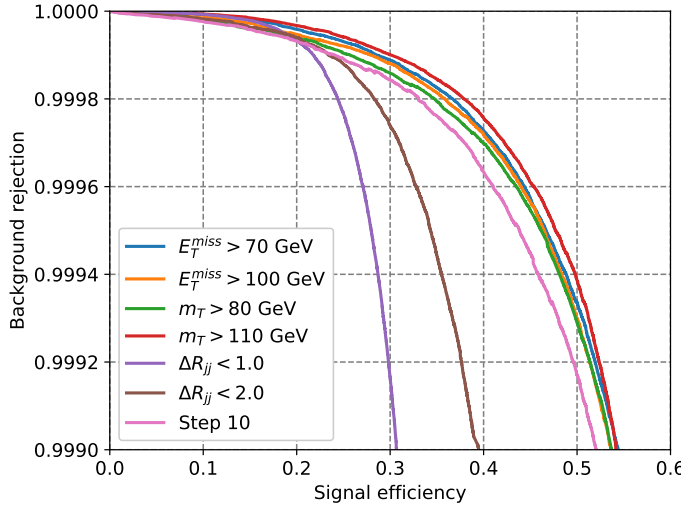


Figure 6.16: Impact of different preselection cuts on the performance of the MLP. It can be seen that, for high background rejection, the *step 10* (randomly picking 1 out of 10 events) shows the lowest signal efficiency. In signal efficiency regions larger than 0.2, the ΔR_{jj} preselection cuts underperform significantly. Overall, a preselection on $m_T > 110 \text{ GeV}$ is found to yield the best results.

following, signal and background events will therefore only be considered if they satisfy $m_T > 110 \text{ GeV}$.

Input observables

Another parameter of interest is the set of observables that are used to train and evaluate the MLP. Again, different setups are tested and compared with the help of their respective ROC curves. In the following, two main different sets of input observables are distinguished: *low-level* and *high-level* quantities.

Low-level observables are the four-momentum components of the lepton and the two first jets as well as E_T^{miss} and $\phi(E_T^{\text{miss}})$:

- E_T^{miss} , $\phi(E_T^{\text{miss}})$, N_{jet} , $N_{b\text{-jet}}$, p_T^ℓ , ϕ^ℓ , η^ℓ , $p_T^{\text{jet}1}$, $\phi^{\text{jet}1}$, $\eta^{\text{jet}1}$, $p_T^{\text{jet}2}$, $\phi^{\text{jet}2}$ and $\eta^{\text{jet}2}$.

As an MLP is not able to deal with varying lengths of input parameters (not all event contains the same number of jets), only the first two jets are included. In the simplified model considered in this chapter, it can be expected that most of the information about the event is already included in the two leading jets. In order to include at least some information about additional jets, the total number of jets N_{jet} and the total number of b -tagged jets $N_{b\text{-jet}}$ are also included.

The term *high-level* denotes observables that have been constructed through combination of low-level observables, as for example the calculation of m_T through \mathbf{p}_T^ℓ and $\mathbf{p}_T^{\text{miss}}$. High-level observables are, if not otherwise stated, the following quantities:

- E_T^{miss} , m_T , m_{jj} , m_{eff} , ΔR_{jj} , N_{jet} , $N_{b\text{-jet}}$.

In principle, the above set of low-level observables contains all information necessary to reproduce the set of high-level quantities. Using low-level observables as input for the MLP could therefore not only result in a neural net reconstructing discriminative high-level observables like m_{eff} or even m_T , but also in a situation where the MLP starts exploiting even more correlations that have not yet been considered in previous studies.

Figure 6.17(a) however shows that, although an MLP trained only on low-level observables as input is able to discriminate signal events against background events, using high-level quantities as input performs noticeably better. This shows that the tested MLP architectures are not yet able to use the full discriminative power supplied by the high-level variables. Training the MLP on the combination of both high- and low-level observables yields, for most parts of the ROC curve, better results than high-level quantities only, illustrating that there is still discriminative information in the four-momentum components not already exploited by the high-level quantities.

In the following, the high-level quantities extended by the transverse momenta of the lepton and the two leading jets are used for training the MLP. Figure 6.17(a) shows that this yields roughly the same ROC curve as the full combination of high- and low-level observables, while allowing faster computation times due to the reduced number of input variables.

It is important to note that there is still a possibility, that even more complex architectures like recurrent neural networks [75, 76] or further optimised MLPs (e.g. through a hyper-parameter scan) could yield setups where low-level observables are comparable to or even outperform high-level quantities.

Network architecture

Although the exact network architecture plays a subordinate role for the final results (given that it is not too simple nor too complex), different MLP sizes are tested. Even though neural nets with very low numbers of neurons or layers can be trained in short periods of time, they generally underperform compared to larger networks as they fail to learn more complex features in data. With an increasing number of neurons and layers, however, the parameter space rapidly grows, causing the need for an increasingly large computational effort in order to train the networks. Choosing a suitable size optimises both computational efficiency and discriminative power of the resulting network.

Figure 6.17(b) compares different architectures, all trained with the set of high-level observables complemented by the transverse momenta. Up to a certain complexity, the MLPs yield increasingly good results. However, there seems to be an optimal size,

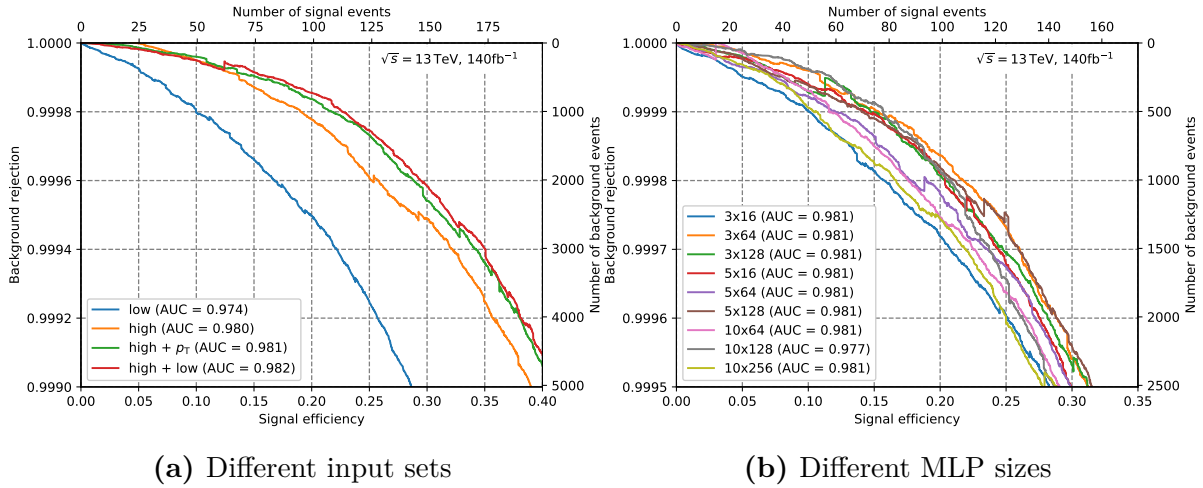


Figure 6.17: Impact of different sets of input quantities (a) as well as different MLP sizes (b). In fig. (b), the nomenclature for each setup is ‘*layers x nodes*’, e.g. three layers and 64 nodes in each layer is written as ‘3x64’. For each setup, the area under the curve (AUC) is stated. The preselection cut of $m_T > 110 \text{ GeV}$ is applied in every setup.

after which the results of the MLP start worsening again if the complexity is further increased. In the following, an MLP with 3 hidden layers and 64 nodes in each layer is chosen. Previous studies [90, 91] have also shown that this size constitutes a powerful general-purpose setup.

6.6.4 Results

The MLP is trained for a maximum of 30 epochs with a batch size of 128 events, but is stopped early if the loss function of the validation set[†] is not decreasing for three consecutive epochs, which helps to prevent overtraining.

In fig. 6.18(b), the distribution of the output score for both signal and background is shown. For illustration purposes, the output-score is spread out through the inverse of the sigmoid function. The full-reconstruction signal sample is evaluated with an MLP that has been trained on the truth signal sample and only test events are used to evaluate the scores in order to prevent biases.

Figure 6.18(a) shows the ROC curves obtained with the same MLP with truth train and truth test samples. As no significant difference between the test and training curve is seen, there is likely no noticeable overtraining.

[†] The validation set is split off from the training set and used for validating the training between epochs.

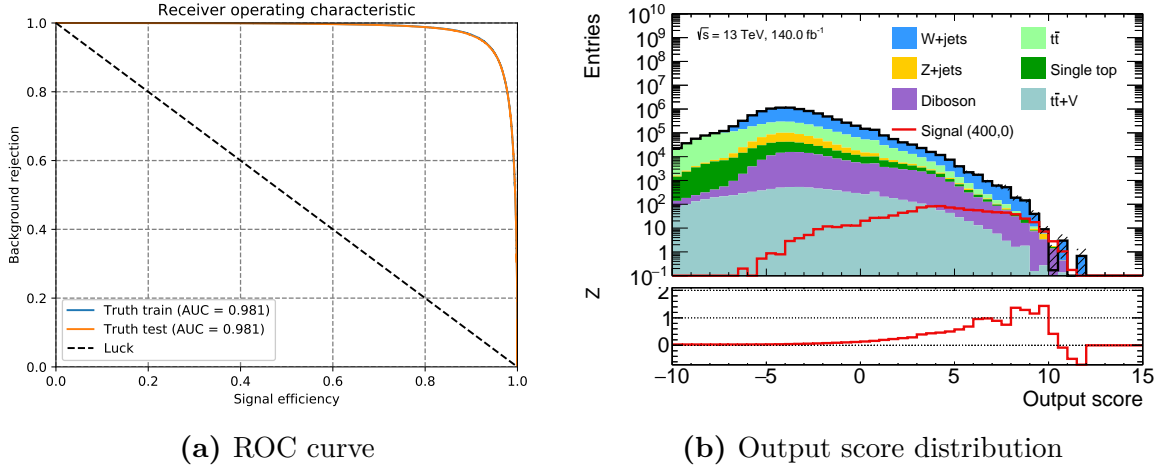


Figure 6.18: Results of a neural net trained on truth-level signal events and tested on full-reconstruction-level signal events. Background events are at full-reconstruction-level both during the training and the testing step. Figure (a) shows the ROC curves from both test and training. As both curves completely overlap, no overtraining has occurred. Figure (b) shows the output score distribution for both background and signal test events together with a significance scan, including statistical uncertainty only. For illustration purposes, the output score is spread out with the inverse of the sigmoid function.

Cut-and-count evaluation

With a simple cut-and-count approach, shown in the lower pad of fig. 6.18(b), a maximum significance of $Z = 1.31$ (only taking into account MC statistical uncertainty) can be reached by cutting on the output score at a value of greater than 8.4. No other cuts, except for the preselection cuts (exactly 1 lepton, at least two jets and $m_T > 110$ GeV) are applied. Table 6.8 summarises the achieved significance value for different uncertainty scenarios. The resulting event yields are in general higher than in the preliminary SR obtained through a multidimensional cut scan, leading to lower statistical uncertainties and fluctuations. However, in such a high yield region, a systematic uncertainty of 30% drastically reduces the significance as it often completely encompasses the signal. Comparing with relatively high statistics signal regions of the previous 1-lepton analyses, a systematic uncertainty of 10% is considered to be still a realistic scenario for a region with such high event yields. This scenario, however, still only yields a significance of $Z = 0.89$.

In summary, no increase in sensitivity is seen compared to the signal region obtained with the N -dimensional cut scan in section 6.4. This is surprising as both approaches essentially use the same input information and therefore a neural net is expected to reach at least the same significance value as a brute-force scan. In the studies presented here, this is not the case. It is, however, possible, that more complex architectures as e.g.

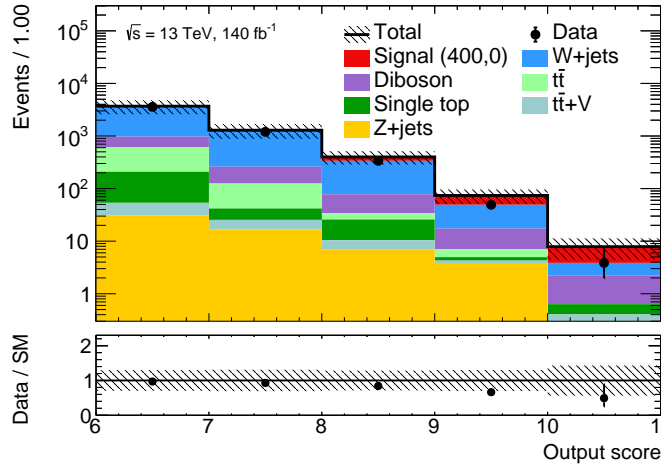


Figure 6.19: Setup of a shape fit on the output score distribution of the neural net. The distribution is binned into five bins from values of 6 to 11. Overflow is included in the last bin. Only events that have not been used for training are considered. MC statistical uncertainties and 10% shape systematic uncertainty are included.

recurrent neural nets [75] are necessary for an algorithm to learn the distinct features of this generic SUSY model. Further conclusions are discussed in section 6.7.

Multi-bin evaluation

Similar to what has been discussed in section 6.5, a simultaneous likelihood fit in multiple bins of the output score distribution (spread out with the inverse of the sigmoid) is investigated. The output score distribution (again spread out through the inverse of the sigmoid) is divided into five bins ranging from values of 6 to 11, including overflow events in the last bin. Figure 6.19 shows the distribution of the background with the signal events stacked on top. As before, MC statistical uncertainty as well as a systematic uncertainty on the shape of the distribution are considered.

With this setup, a discovery significance of 2.15σ (2.26σ) is reached when considering an overall systematic uncertainty of 30% (10%) as well as MC statistical uncertainty. This is an improvement compared to the previous cut-and-count evaluation on the

Table 6.8: Different uncertainty scenarios for the output score significance scan through a cut-and-count approach with the (400,0) benchmark point.

Uncertainty scenario	Output score cut	$Z [\sigma]$
MC statistical unc. only	> 8.4	1.31
MC statistical unc. + 10% systematic unc.	> 7.2	0.89
MC statistical unc. + 30% systematic unc.	> 7.8	0.35

Table 6.9: Different uncertainty scenarios considered in a shape fit on the output score shape.

Uncertainty scenario	$Z [\sigma]$
MC statistical unc. + 10% systematic unc.	2.26
MC statistical unc. + 30% systematic unc.	2.15

output score and roughly the same sensitivity as in the shape fit on m_T . Table 6.9 summarises the different uncertainty scenarios and the achieved discovery significance values. In summary, although neural nets present a considerable increase in complexity, no significant sensitivity improvement compared to cut-based techniques is obtained within this work.

6.7 Discussion

In this chapter, different attempts to estimate the sensitivity of the 1-lepton channel to a generic electroweak pair production SUSY model have been presented. Although targeting an integrated luminosity of 140 fb^{-1} and using analysis techniques with varying degrees of complexity, the reached significance values for the considered benchmark points are in general relatively low.

A first approach uses an N -dimensional cut scan and estimates the significance values in a preliminary signal region with a cut-and-count approach in a single signal region bin. The reached sensitivity is mainly limited by the available MC statistics for $W + \text{jets}$, the dominant background in the region of interest. By adding a multi-bin shape fit in a discriminative observable and slightly relaxing some of the signal region requirements, it is possible to further increase the sensitivity, even though considering both MC statistical uncertainties and an overall systematic uncertainty of 30%. With the currently available MC statistics and a shape fit in the m_T distribution, it could be possible to exclude signal points with $\tilde{\chi}_1^\pm$ masses between 300 GeV and 500 GeV[†] and $\tilde{\chi}_1^0$ masses of up to (roughly) 40 GeV. Compared to the exclusion limits obtained by the *2-lepton* search, an analysis searching for the same simplified model in events with two leptons [78], the introduced shape fit on m_T can exclude slightly higher $\tilde{\chi}_1^\pm$ masses[§], but only lower $\tilde{\chi}_1^0$ masses.

Additionally, machine learning algorithms have been investigated as a tool to discriminate the SUSY signal against SM background. In this work, multilayer perceptrons, a special architecture of neural nets, are used. Although machine learning is a promising tool in many fields of research, no significant increase in sensitivity is obtained in this work for the *WW* model, even if fitting the shape of the output score of the neural net.

[†] The exclusion power on the $\tilde{\chi}_1^\pm$ mass axis could potentially exceed both the lower and upper bound of 300 GeV and 500 GeV respectively, however, due to missing benchmark points in these regions, it is not possible to make any definite statements.

[§] The limits from the *2-lepton* analysis are obtained with data corresponding to an integrated luminosity of 80.5 fb^{-1} as opposed to the optimisation for 140 fb^{-1} presented in this work.

An interesting extension to the studies presented here would be to investigate more complex architectures and whether or not it is possible that machine learning algorithms learn high-level correlations (e.g. m_T or m_{eff}) purely from low-level information [92] (the four-momenta of the physics objects). In this work and other recent studies [90, 91], neural nets trained on low-level information have not yet been able to fully exploit or even outperform the discriminative power of high-level quantities like the transverse mass. Nevertheless, it could in principle be possible to improve this by more complex setups not considered in this work.

In summary, the best approach for searching for the WW model in the 1-lepton channel seems to be through a shape fit setup in a discriminative variable like e.g. m_T . It is not surprising to see that, due to the missing $h \rightarrow b\bar{b}$ decay, the sensitivity to the WW model is significantly weaker than to the Wh model, even when using advanced analysis techniques and optimising for 140 fb^{-1} of data. However, the added advantage of interpreting data with the WW model is an increased model independence due to the generic nature of the model. Although designing a complete analysis using the WW model would be challenging, the presented studies have shown that it is in principle possible to achieve exclusion for certain non-compressed model points. With more MC statistics available at a later stage in Run-2 of the LHC, as well as the use of data-driven methods, the estimation of the m_T shape for the background, especially for $W + \text{jets}$, can become more reliable. This could lead to lower statistical uncertainties and potentially further increase the sensitivity of a shape fit setup.

Chapter 7

Sensitivity of the 1-lepton analysis to the phenomenological MSSM

As explained in section 1.2.7, the reduced parameter space in the phenomenological MSSM (pMSSM) is, with some additional requirements (explained in section 7.4.1), small enough to be systematically scanned and compared to ATLAS data. Although simplified models are often a very useful method to capture a wide range of different phenomena, they evidently fail to capture more complex effects resulting from a larger set of parameters and could assert relationships between SUSY parameters that are not realised in nature. Sampling a more complete portion of the model space of the MSSM, as e.g. the pMSSM, is therefore appealing.

In Run-1 of the LHC, a pMSSM scan [28] including signal regions from a multitude of different SUSY searches has been performed. Amongst other things, it showed that, for the strong 1-lepton analysis, there are significant differences between the nominal results of the search using simplified models and the results to the pMSSM itself. As it turns out, the discrepancies are mostly caused by the use of different signal regions as well as different implementations of the statistical analysis. For this reason, efforts to improve the representation of the 1-lepton analysis in the Run-2 pMSSM scan are presented in the following.

7.1 Motivation and procedure

Compared to other searches for gluinos and squarks, the Run-1 strong 1-lepton analysis [71] showed a competitive sensitivity to different decay topologies. This was, however, not reflected in the Run-1 pMSSM scan, as the strong 1-lepton analysis revealed a reduced sensitivity compared to other analyses.

Previous studies [93] have already shown that the main reason for the large difference in performance is the fact that the Run-1 pMSSM scan did not use the shape fits in m_{eff}

implemented in the nominal analysis, but rather ‘discovery’ signal regions with a single m_{eff} bin, thereby applying a simpler cut-and-count evaluation of the significance instead of using the m_{eff} -shape information.

Similar to the pMSSM scan in Run-1 of the LHC, there are ongoing efforts for a Run-2 pMSSM scan. The goals of the scan are not only to search for SUSY in a larger parameter space and to assess the combined sensitivity of the searches considered in the scan, but also to provide input to the design of future analyses and identify possible blind spots in the parameter space not yet covered by analyses. Up to now, still only the discovery signal regions (defined in section 7.1.2) of the Run-2 strong 1-lepton analysis were implemented instead of the shape fit used in the nominal analysis. As multi-bin fits generally achieve better sensitivity than simple cut-and-count approaches with single bin fits, the implementation of a shape fit for the strong 1-lepton analysis in the Run-2 pMSSM scan is expected to significantly improve the performance of the analysis in the scan.

Since a pMSSM scan samples SUSY models over a vast parameter space, a large amount of model points[†] (10^5 to 10^6 different points) have to be produced, thus preventing the use of a time-consuming full detector reconstruction. Most sampled signal points are therefore truth-level samples that have only been corrected through the *smearing procedure* described in section 7.1.1 in order to consider a minimal detector response approximation and increase the reliability of the results. Hence, in order to successfully implement a shape fit for the 1-lepton analysis in the pMSSM scan, it is of central importance that the shapes of the truth-level distributions match the shapes on full-reconstruction (reco) level. Furthermore, since the scan has to be as CPU-effective as possible, a short completion time has to be achieved for the fit, while still considering a realistic systematic uncertainty scenario and a reliable background prediction[§].

Figure 7.1 schematically summarises the procedure used to verify that a simplified shape fit setup applied on truth samples can indeed successfully reproduce the results of a shape fit on fully reconstructed samples considering all systematic uncertainties. The first step of the procedure compares the distributions between reco and truth samples at preselection and in the signal regions and, if necessary, applies smearing techniques in order to improve the agreement. In a second step, a simplified shape fit setup is applied both on truth and full-reconstruction samples. The resulting exclusion contour is compared with the contour from the Run-2 strong 1-lepton analysis [26], obtained with shape fits in m_{eff} including all systematic uncertainties and performed on fully reconstructed MC samples. More details on the shape fit and the employed signal regions are given in section 7.1.2. A good agreement needs to be found between the results of the analysis and the results obtained using a simplified shape fit and smeared truth

[†] Again, a *model point* is a given model with a unique set of model parameters, which is not feasible for a scan over up to 10^6 points.

[§] A shape fit with full consideration of systematic uncertainties and background estimation through a set of control regions takes, in this case, multiple hours per signal point.

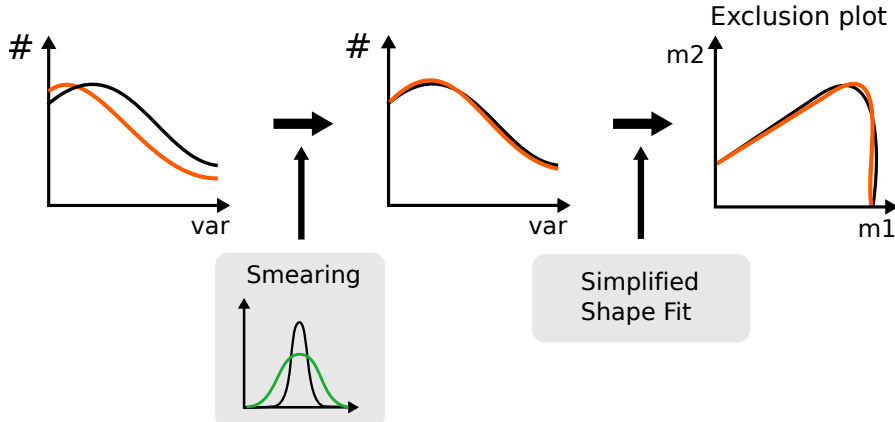


Figure 7.1: Schematic overview of the procedure used to verify the validity of a simplified shape fit setup. The orange line represents truth distributions, and the black line fully reconstructed distributions. A first step includes the application of smearing techniques in order to improve the agreement between the distributions of truth and full-reconstruction samples. A second step verifies that a simplified shape fit setup is able to reproduce the exclusion limits from the 1-lepton analysis.

samples in order for the procedure to yield any meaningful results when applied on a large number of pMSSM models.

7.1.1 Smearing algorithms

The smearing of truth samples is implemented with `SimpleAnalysis` [89], a software package that uses specialised functions developed for ATLAS upgrade studies. The general idea of the smearing procedure is to use results from the combined performance (CP) groups in ATLAS in order to construct approximate parametrisations for reconstruction and identification efficiencies as well as scale factors. Additionally, the energies of the truth objects are smeared with a Gaussian term with a standard deviation corresponding to the energy resolution of the detector, depending on η and p_T and the reconstructed physics object type. In this work, truth electrons, truth muons, truth jets and the truth missing transverse energy are smeared.

For truth electrons, the identification efficiencies depend on η and p_T as well as on the reconstruction working point used. The η -dependency is implemented through several η bins with a fixed width. For the p_T -dependency, a linear interpolation between two adjacent values is used to get the efficiency value for each electron. The rate at which fake electrons are reconstructed in true jets is calculated through ‘fake rates’ depending again on η , p_T and the isolation working point used. The range of the p_T interpolation for both identification and isolation efficiencies extends from 7 GeV to 120 GeV. If an electron is outside of that range, the efficiency values for the respective bound of the

range are used[†]. The energy of the truth electron is subsequently smeared through a Gaussian term with a mean corresponding to the truth value and a standard deviation equal to the energy resolution that depends again on η and p_T .

In the case of truth muons, the identification efficiencies are only binned in η with different values depending on the working point used. As before, the transverse energy of the truth muon is smeared with a Gaussian term. The mean of the Gaussian is equal to the true transverse energy value while the resolution is approximated separately for the barrel and the endcap regions.

The energy of truth jets is smeared with a Gaussian term using a resolution approximation based on five η bins ranging from $|\eta| = 0$ to $|\eta| = 4.5$. Only jets with a truth p_T between 10 GeV and 1500 GeV are smeared. For jets with a truth $p_T > 20$ GeV, the flavour-tagging efficiencies for the different tagging working points are approximated using values measured from a fully reconstructed $t\bar{t}$ MC sample. This includes the tagging efficiencies for light-, bottom-, charm- and tau-jets and, in this work, allows a significantly more realistic simulation of the b -jet multiplicity.

Finally, the smeared missing transverse energy is computed using the transverse momenta of the smeared truth objects and an approximation for the track soft terms (TST). For the TST, based on the ideal momentum balance between hard and soft objects in an event, $\mathbf{p}_T^{\text{hard}} = -\mathbf{p}_T^{\text{soft,true}}$, the truth sum of all smeared hard objects $\mathbf{p}_T^{\text{hard,true}}$ (after OR and including true E_T^{miss}) is smeared with a Gaussian term with standard deviation corresponding to the E_T^{miss} resolution parallel and perpendicular to $\mathbf{p}_T^{\text{hard,true}}$. The resolutions are taken from the data/MC ratios from $Z \rightarrow e^-e^+$ events. The difference between the smeared and the original $\mathbf{p}_T^{\text{hard,true}}$ is taken as approximation for the TST.

7.1.2 Simplified shape fit

In the Run-2 strong 1-lepton analysis, four different signal regions[§] (SRs) are used to be sensitive to different gluino and squark pair-production models. One of the considered models is the gluino one-step model considered in this chapter. Table 7.1 summarises the different signal regions. Among the observables used to define the SRs is the aplanarity, a quantity that is defined to be 3/2 of the third eigenvalue of the sphericity tensor [94] and indicates how spherical the distribution of the momenta of the particles in each event is [46]. Since SUSY events are often characterized by decays into multiple hard objects, they tend to have a more spherical distribution of momenta. In table 7.1, two different signal regions requiring four to five jets are defined, differentiated by a *high-x* and a *low-x*

[†] For an electron with $p_T = 150$ GeV, the same fake rate as for electrons with $p_T = 120$ GeV is used.

[§] Apart from the SRs summarised in table 7.1, another SR targeting events with at least 9 jets is designed in the analysis. Since this 9J SR is not orthogonal to the 6J SR, it cannot be simultaneously fitted but rather needs an independent shape fit. In the following, the 9J SR will therefore not be included.

Table 7.1: Signal regions defined in the Run-2 strong 1-lepton analysis used for the gluino/squark one-step model. For the exclusion, a shape fit in m_{eff} in the defined bins is employed. Table taken and adapted from Ref. [26].

SR	2J	4J high-x	4J low-x	6J
N_ℓ	= 1	= 1	= 1	= 1
p_T^ℓ [GeV]	> 7(6) for $e(\mu)$ and < min(5 · N_{jet} , 35)	> 35	> 35	> 35
N_{jet}	≥ 2	4–5	4–5	≥ 6
E_T^{miss} [GeV]	> 430	> 300	> 250	> 350
m_T [GeV]	> 100	> 450	150–450	> 175
Aplanarity	–	> 0.01	> 0.05	> 0.06
$E_T^{\text{miss}}/m_{\text{eff}}$	> 0.25	> 0.25	–	–
$N_{b-\text{jet}}$ (excl)		= 0 for b -veto, ≥ 1 for b -tag		
m_{eff} [GeV] (excl)	3 bins ∈ [700,1900] + [> 1900]	2 bins ∈ [1000,2000] + [> 2000]	2 bins ∈ [1300,2000] + [> 2000]	3 bins ∈ [700,2300] + [> 2300]
m_{eff} [GeV] (disc)	> 1100	> 1500	> 1650(1300) for gluino (squark)	> 2300(1233) for gluino (squark)

addition. Here, x refers to the ratio of mass differences between the chargino and the LSP and the gluino/squark and the LSP, $x = \frac{m(\tilde{\chi}_1^\pm) - m(\tilde{\chi}_1^0)}{m(\tilde{g}/\tilde{q}) - m(\tilde{\chi}_1^0)}$, introduced in section 1.2.6.

Factoring in the subdivisions in regions requiring at least one b -tagged jet (b -tag region) and regions requiring no b -tagged jet (b -veto region) as well as the different m_{eff} -bins in each SR, a total of 28 SR bins arise. Since each SR bin is completely orthogonal to every other bin, a simultaneous likelihood fit in all bins can be performed. In the full analysis, the background prediction in the SRs is obtained by a simultaneous fit in all bins in the control regions (CRs).

In the simplified shape fit setup used within this chapter, control regions are used to obtain the background estimates nor complete treatment of systematic uncertainties is included. Instead, the fitted background yields in the SRs and their uncertainties are taken from a previous simultaneous fit in the CRs and the SRs (ignoring the signal), performed by the analysis. The results of this background-only fit are available in the auxiliary material of the published results [26]. The statistical model is subsequently approximated by taking, for each SR bin, the total background yields and the total uncertainty and assuming that the uncertainties are completely correlated over all bins. Similar to the full fit in the analysis, the simplified setup performs a simultaneous fit in all 28 SR bins. With this setup, the expected and observed (using data corresponding to 36.1 fb^{-1}) CL_s values for signal points can be determined.

Since the detailed treatment of systematic uncertainties is responsible for the majority of the CPU-time necessary to complete the original fits in the published analysis, this approach, combined with the omission of the CRs, guarantees the short completion time

(of the order of a few seconds as opposed to multiple hours per signal point) needed for an extensive scan over the full pMSSM parameter space. As before in chapter 6, the shape fit is implemented using `HistFitter`.

7.2 Truth- and reco-level comparisons

This section compares truth- and full-reconstruction-level distributions both after applying a basic preselection and in the different SRs used in the strong 1-lepton analysis.

7.2.1 Comparison at preselection level

The applied preselection requires exactly one signal lepton, at least two jets with $p_T > 30 \text{ GeV}$ and $E_T^{\text{miss}} > 250 \text{ GeV}$. Figure 7.2 shows comparisons of truth- and full-reconstruction-level distributions for one exemplary signal point. Although the agreement is in general surprisingly good, some mismodellings of the unsmeared truth samples become visible. Overall, the unsmeared truth MC samples tend to slightly overestimate the total number of events after preselection. This is, however, not surprising as no reconstruction and identification efficiencies are included in the truth MC samples.

Apart from the differences in the total event yields, the truth distributions also exhibit some differences in shape compared to the reco distributions. For example, as can be seen in fig. 7.2(h), the simulation of the b -jet multiplicity at unsmeared truth level, exhibits no agreement at all with the multiplicity from fully reconstructed samples. After applying smearing on the truth samples, thereby considering b -tagging efficiencies and other jet reconstruction corrections, a good agreement between truth and full-reconstruction samples can be achieved (see fig. 7.3(h)).

Similarly, fig. 7.2(b) reveals that the truth samples predict significantly more events with low- p_T leptons than fully reconstructed samples. In fig. 7.4, the lepton p_T distribution is split into the electron and muon components, revealing that electrons contribute more to the lepton p_T mismatch than muons. This is not surprising as electrons have lower reconstruction and identification efficiencies than muons for relatively low transverse momenta [58, 56]. After including an approximation of these efficiencies through the use of the smearing procedure, it can be seen in figs. 7.3(b) and 7.4(b) that the systematic mismatch for low- p_T leptons and especially electrons can be significantly reduced. As the lepton p_T directly influences the m_{eff} distribution, the agreement between truth and full-reconstruction distributions is also improved for m_{eff} after smearing the truth samples.

Additionally, the m_T distribution in fig. 7.2(d) reveals that the truth samples exhibit a slight mismodeling in the shape of m_T . Even though the overall normalisation matches better after smearing, the slight difference in shape persists. However, since the m_T distribution is not used for a shape fit but only a simple lower cut in the SRs, the slight

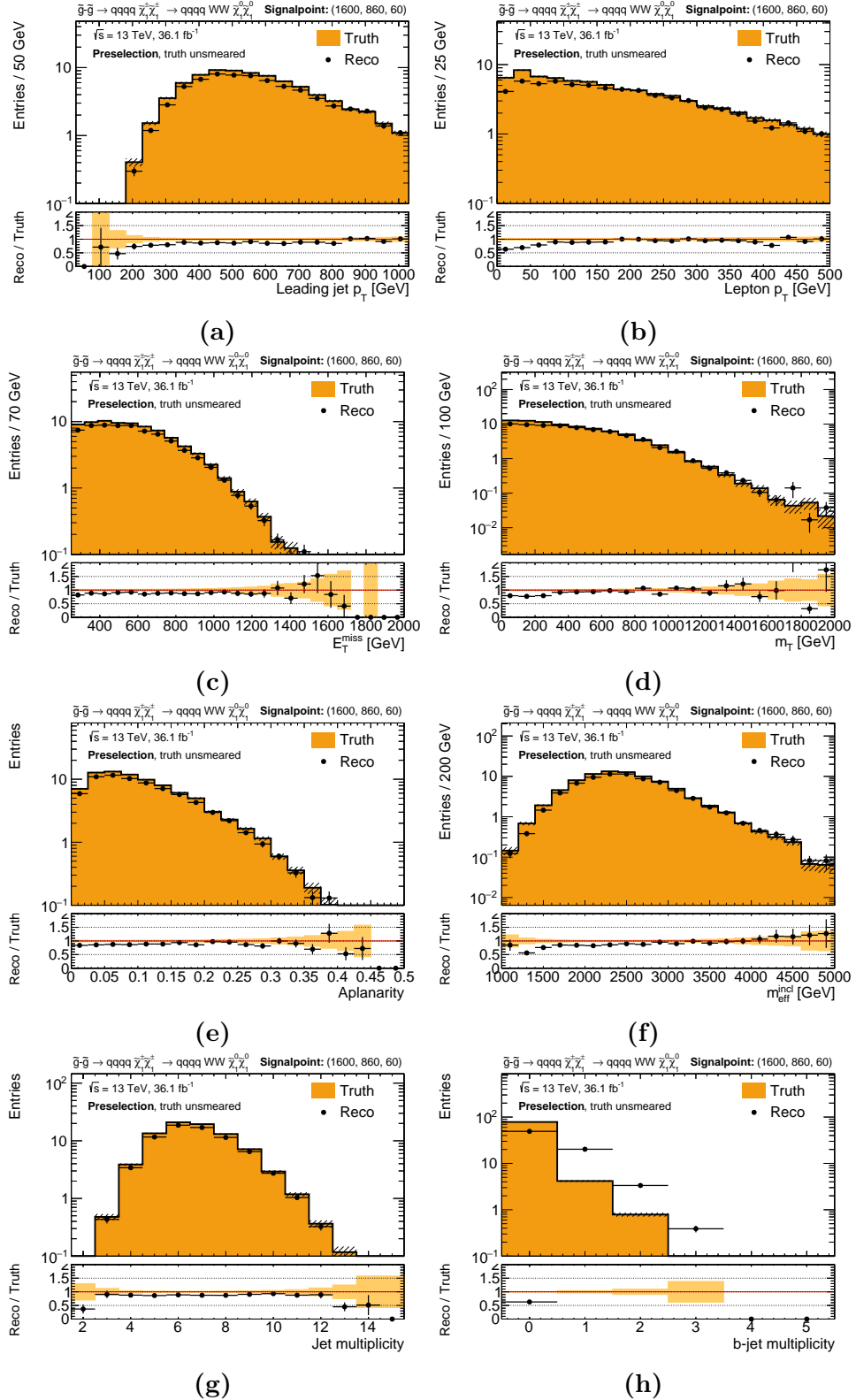


Figure 7.2: Comparison of distributions at reco- and truth-level. The truth samples have not been smeared. The signal point shown is an exemplary point. Throughout the entire signal grid, similar differences between truth and reco are visible. The signal point nomenclature is $(m_{\tilde{g}}, m_{\tilde{\chi}_1^\pm}, m_{\tilde{\chi}_1^0})$ in GeV. The error bands and error bars include MC statistical uncertainty.

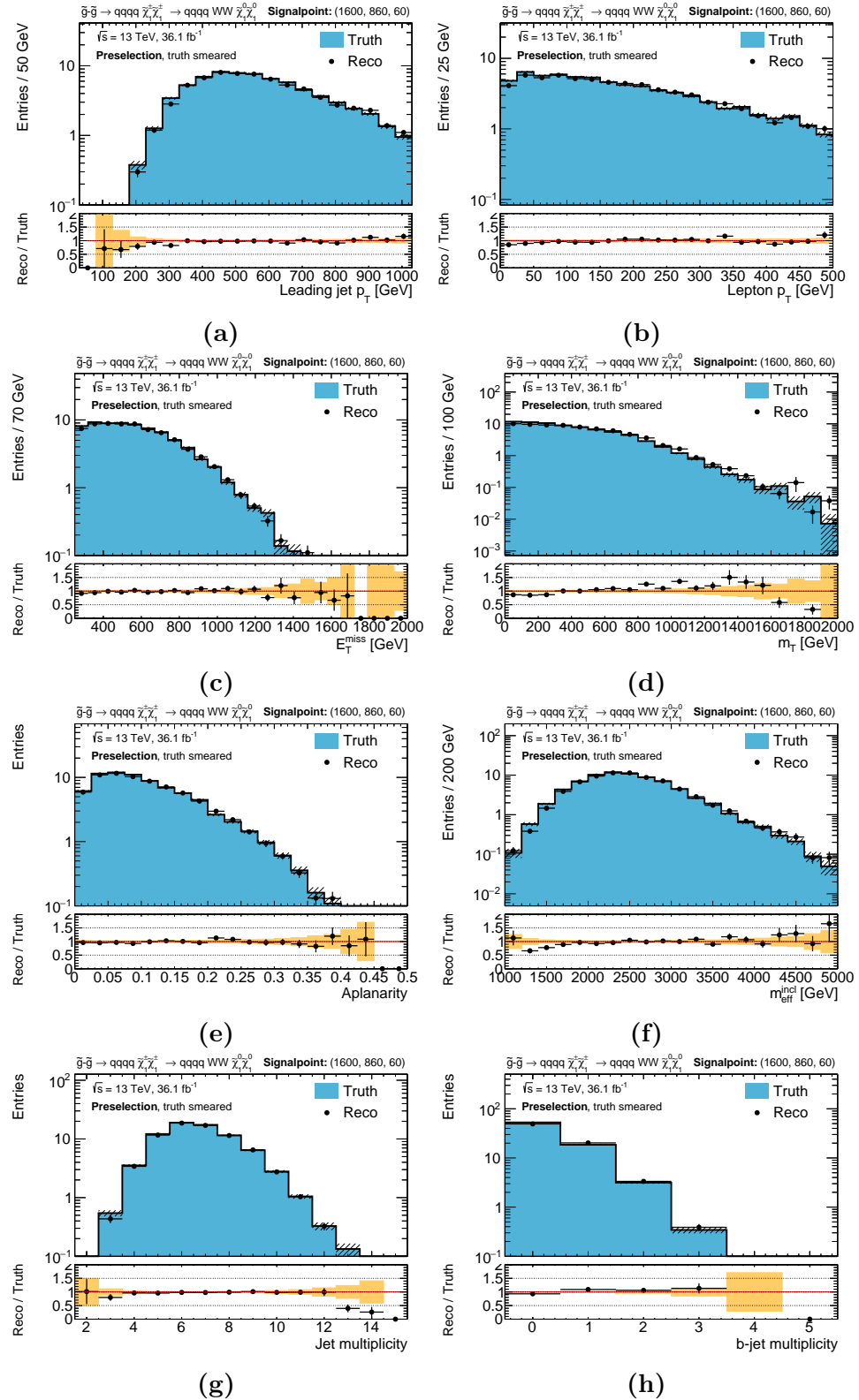


Figure 7.3: Comparison of distributions at reco- and truth-level. The truth samples have been smeared. Applying the smearing methods has helped to reduce the differences between truth and reco distributions. The error bands and error bars include MC statistical uncertainty.

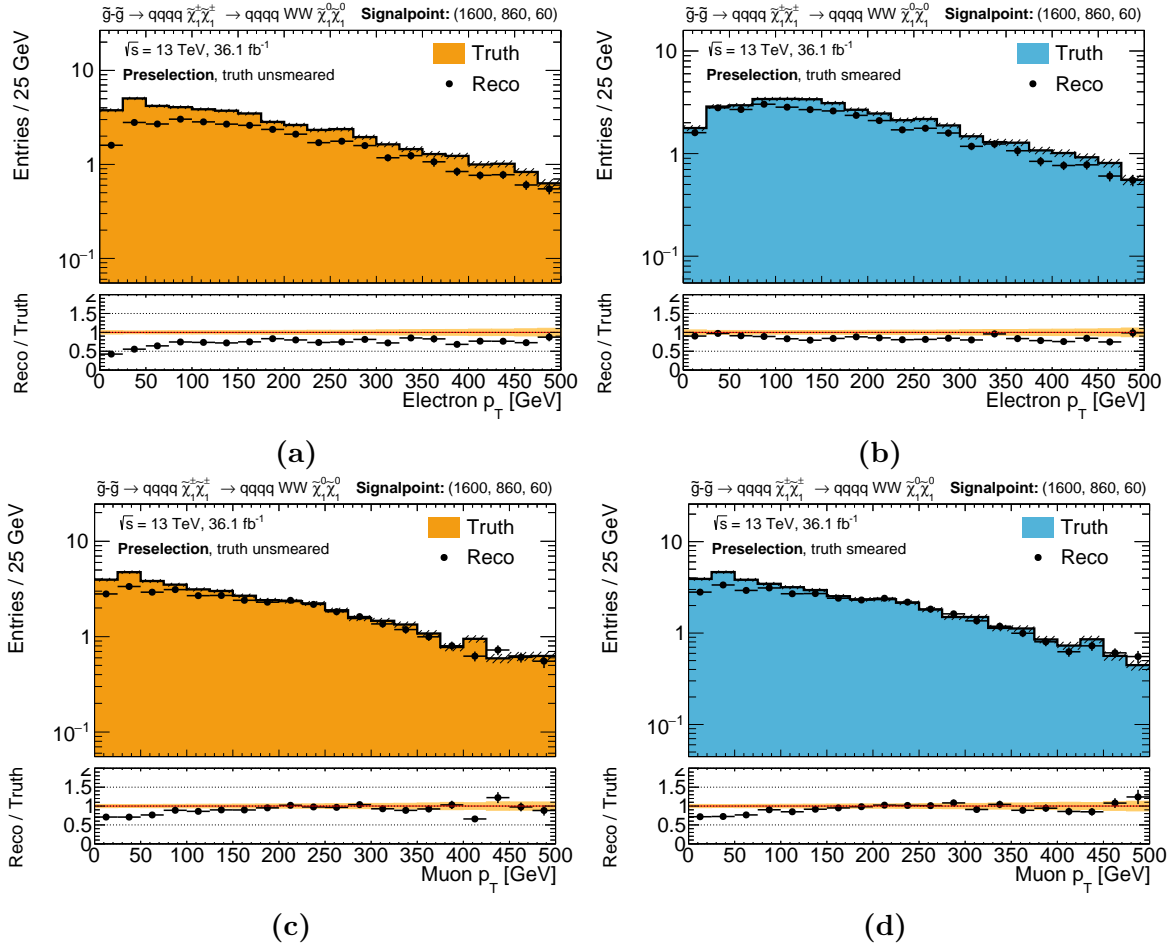


Figure 7.4: Comparison of the reco-level and truth-level lepton p_T distribution split in electron and muon components. In the left column, unsmeared truth samples are shown, while in the right column, smeared truth samples are used. The electrons contribute the most to the systematic mismatch between truth and reco. The application of smearing techniques significantly reduces the low p_T mismatch in the electron distribution. The muon p_T distribution does not show a significant difference after smearing. The error bands and error bars include MC statistical uncertainty.

mismodelling in the smeared truth sample is considered to have an acceptably low effect on the final result.

7.2.2 Comparison in the signal regions

For the performance of the shape fit setup, the agreement of the distributions in the SRs is of central importance, since these are the selections actually used in the fit.

Figure 7.5 shows comparison plots using all the signal points in the signal grid and comparing the total truth yields with the total reco yields in different signal regions. For this purpose, the inclusive SRs (adding up all m_{eff} bins to a single SR bin, thereby ignoring the shapes) are used. The left column in fig. 7.5 shows the truth yields before smearing and the right column after smearing the truth MC samples. The top and middle row contain scatter plots where each signal point in the signal grid is a single point in the plot. A drastic improvement can be seen after applying smearing on the truth MC samples. In general, all points in the scatter plot lie significantly closer to the diagonal, where $N_{\text{events}}^{\text{truth}} = N_{\text{events}}^{\text{reco}}$. This confirms that the overall numbers of events in the SRs predicted by the smeared truth samples matches the prediction by full-reconstruction samples. A complete set of scatter plots for the remaining SRs can be found in appendix B.1.

The agreement of the total yields in each SR is further confirmed in the bottom row in fig. 7.5, showing a combination of all SRs. The ratio between truth and reco yields for each signal point is determined in each SR and filled in a histogram. Entries from b -tag SRs are coloured in light green while entries from b -veto SRs have a dark green colour. The significant overestimation (underestimation) of events in the unsmeared truth samples in b -veto (b -tag) SRs is again clearly visible. After applying smearing, the $N_{\text{events}}^{\text{truth}}/N_{\text{events}}^{\text{reco}}$ ratio distribution is centred around 1, i.e. $N_{\text{events}}^{\text{truth}} \approx N_{\text{events}}^{\text{reco}}$ for a large portion of the signal points.

As a shape fit in m_{eff} is employed in the following, the agreement of the shapes of the distributions rather than the total yields is of importance for this observable. Figure 7.6 therefore shows a comparison between the distributions in different SRs and for exemplary signal points. It can be seen that, after smearing the truth samples, the agreement between the m_{eff} distributions is significantly improved, and the small remaining differences in general lie within the statistical uncertainties.

7.3 Simplified shape fit application

Full-reconstruction signal samples

In order to verify the validity of a simplified shape fit as defined in section 7.1.2, the fit setup is first applied on the same full-reconstruction MC signal samples that have already been used in the strong 1-lepton analysis to derive the published analysis results. Thus,

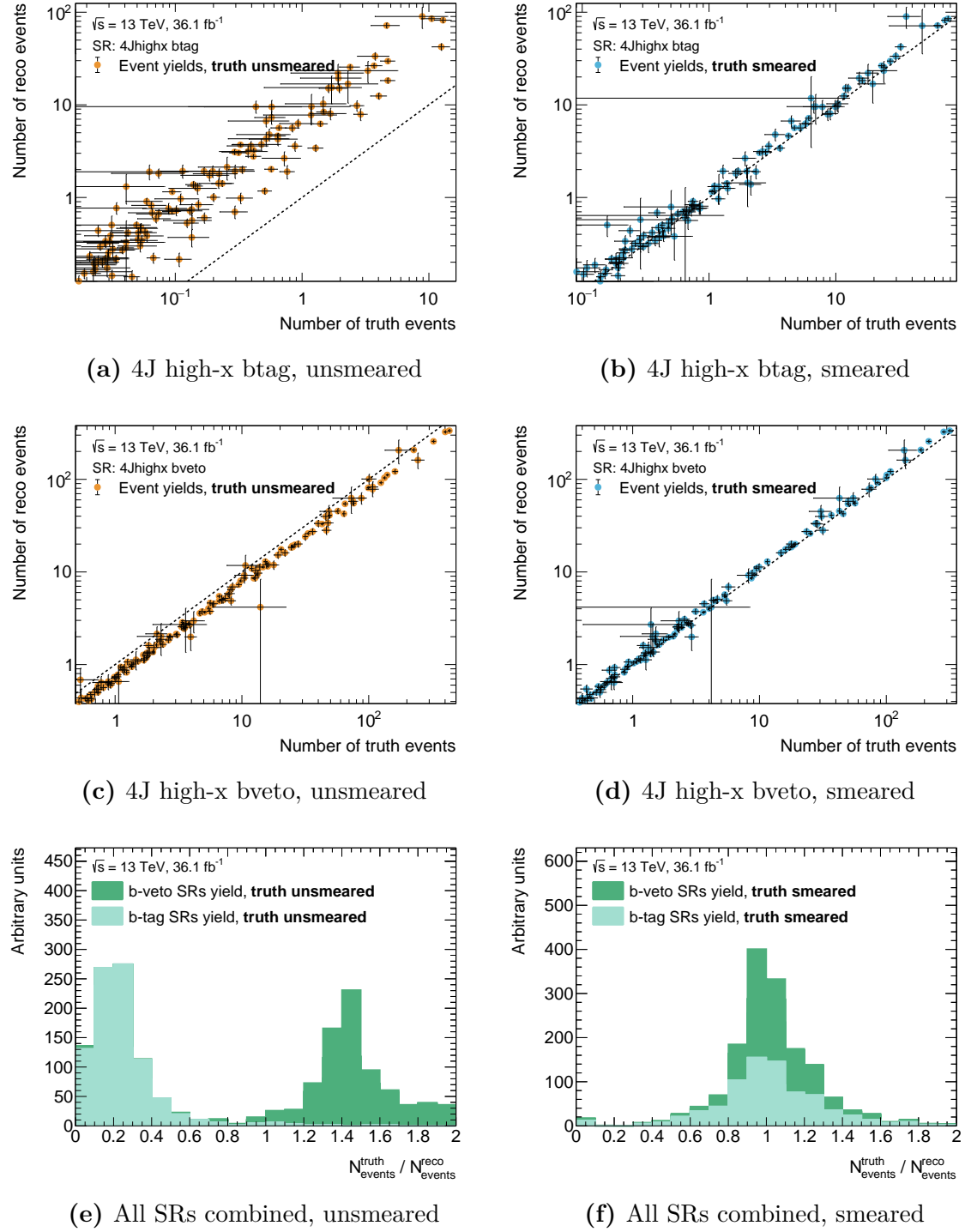


Figure 7.5: Comparison of reco- and truth-level yields in the SRs. All m_{eff} -bins are added up to one single bin per SR. The left column shows the truth yields before smearing and the right column after smearing the truth MC samples. The top and middle row show scatter plots of the yields per signal point in specific SRs. The dotted line is the diagonal where $N_{\text{events}}^{\text{truth}} = N_{\text{events}}^{\text{reco}}$. The error bars include MC statistical uncertainty. The bottom row combines all SRs together, i.e. every signal point in the grid has eight different entries for the eight SRs. In both representations, a significant improvement is seen in the agreement between truth and reco yields in the SRs after applying smearing on the truth samples.

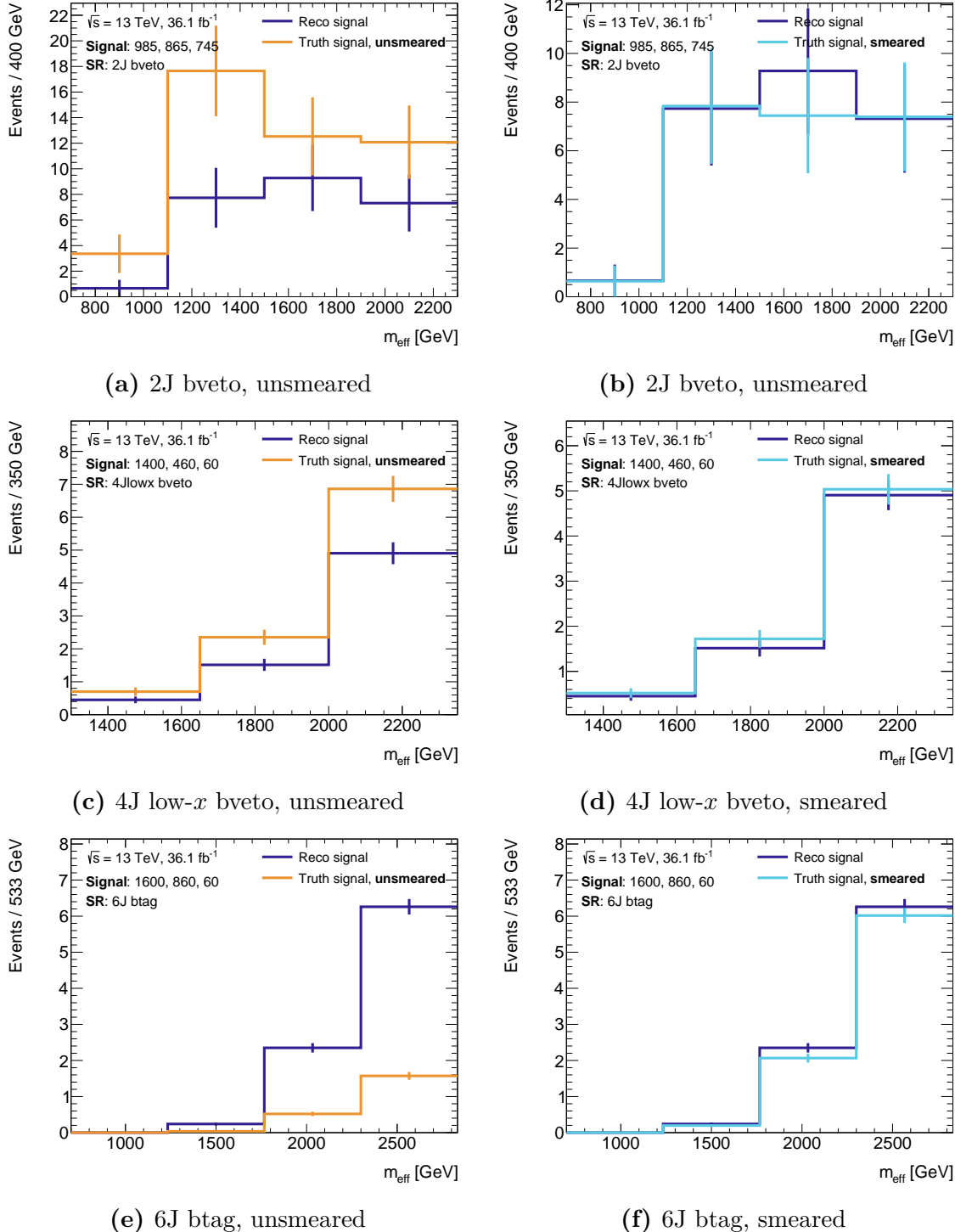


Figure 7.6: Exemplary comparisons of the shape of m_{eff} in different signal regions for various signal points before and after smearing. In general, it can be observed that the agreement between the shapes is significantly better after smearing the truth samples. The error bars include statistical uncertainty from the MC samples.

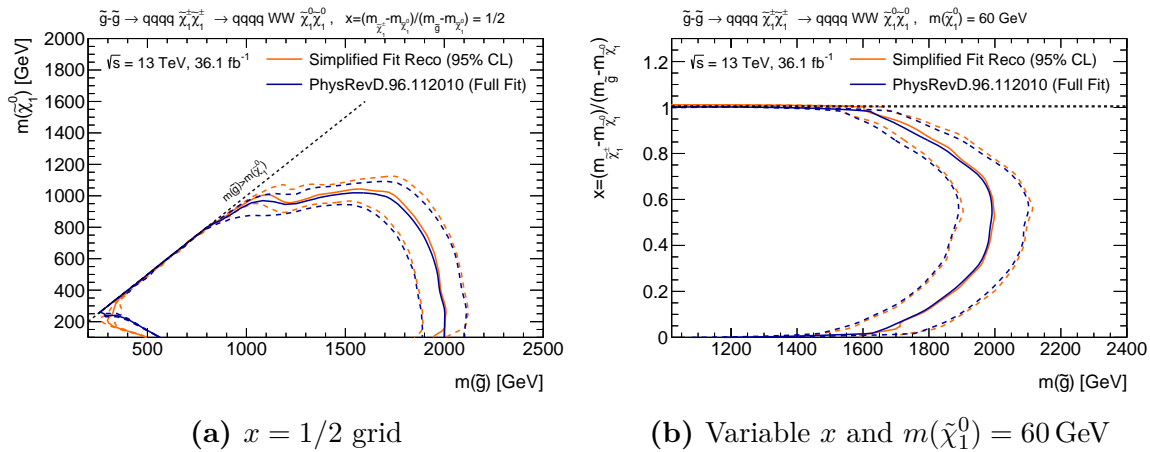


Figure 7.7: Comparison of the exclusion contour (solid line) obtained with the simplified fit (green curve) and the full analysis fit (dark blue curve). Both setups use the same fully reconstructed MC signal samples and the contours are drawn at 95% CL. The dashed lines show the $\pm 1\sigma$ variations. Expected CL_s values are used. Excellent agreement is found between the simplified and the full setup. Figure (a) shows the signal grid with $x = 1/2$ and fig. (b) shows the signal grid with variable x and $m(\tilde{\chi}_1^0) = 60$ GeV.

the only difference between the resulting expected exclusion limits is the simplified nature of the shape fit used within this chapter. Figure 7.7 shows a comparison between the expected exclusion contours obtained by the full analysis fit and by the simplified shape fit. Excellent agreement is seen throughout both $x = 1/2$ and the variable- x versions of the signal grid. Only minor differences are visible in the $x = 1/2$ grid at very low $\tilde{\chi}_1^0$ masses, most probably caused by interpolation artefacts[†].

The excellent agreement between the simplified and the full setup validates the procedure of approximating the statistical model by taking, for each SR bin, the total background and the total uncertainty and assuming the uncertainties to be fully correlated over all bins. While the full statistical evaluation in the strong 1-lepton analysis takes multiple hours per signal point, the simplified shape fit only needs a few seconds. Using this approximation of the strong 1-lepton analysis, computationally efficient and precise statements about the sensitivity of the analysis to other supersymmetric models are possible for the first time.

Figure 7.8 shows a first set of reinterpretation studies of other simplified models within the analysis, illustrating that sensitivity to a variety of other models, including one with R-parity violation, are achieved. In figs. 7.8(a) and 7.8(b), the sensitivity to the gluino two-step model and a pMSSM slice already used in the strong 1-lepton analysis (but analysed with a SR requiring at least 9 jets [26]) is assessed. Figures 7.8(c) and 7.8(d) show the sensitivity of the analysis to gluino/squark pair production models including W and Z/h bosons (as opposed to only W bosons) [95]. Finally, sensitivity is also achieved

[†] The interpolation of grid edges is problematic because not enough neighbouring interpolation points are available on each side.

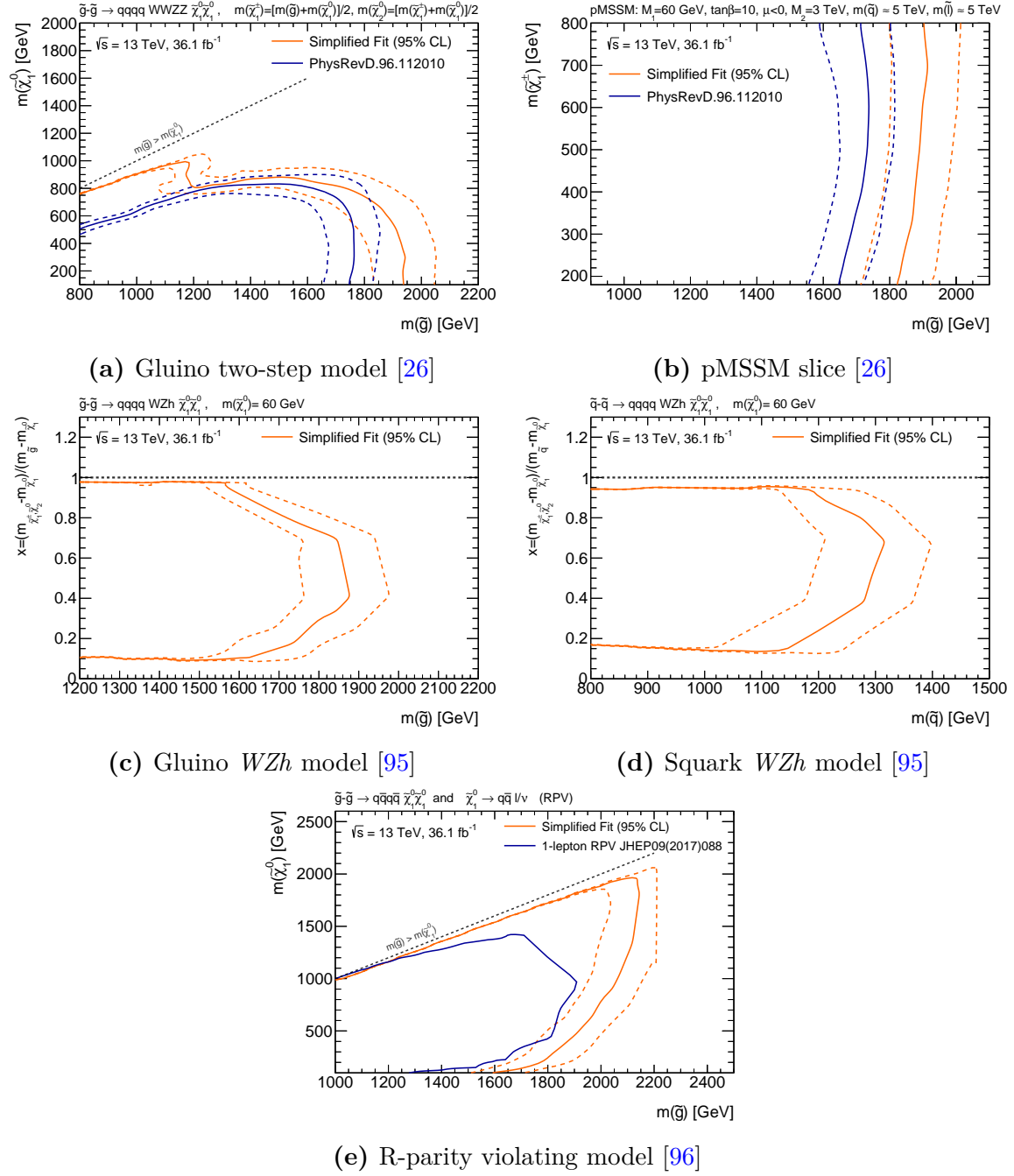


Figure 7.8: The approximation of the full analysis through the simplified shape fit allows reinterpretations of other SUSY models within the strong 1-lepton analysis. All shown contours are expected exclusion limits drawn at 95% CL. Where available, the contours obtained by the simplified fit (in orange) are compared with expected exclusion contours from analyses targeting the respective models (in blue). The strong 1-lepton analysis is not only sensitive to various gluino and squark decay modes, but also a pMSSM slice as well as an R-parity violating model.

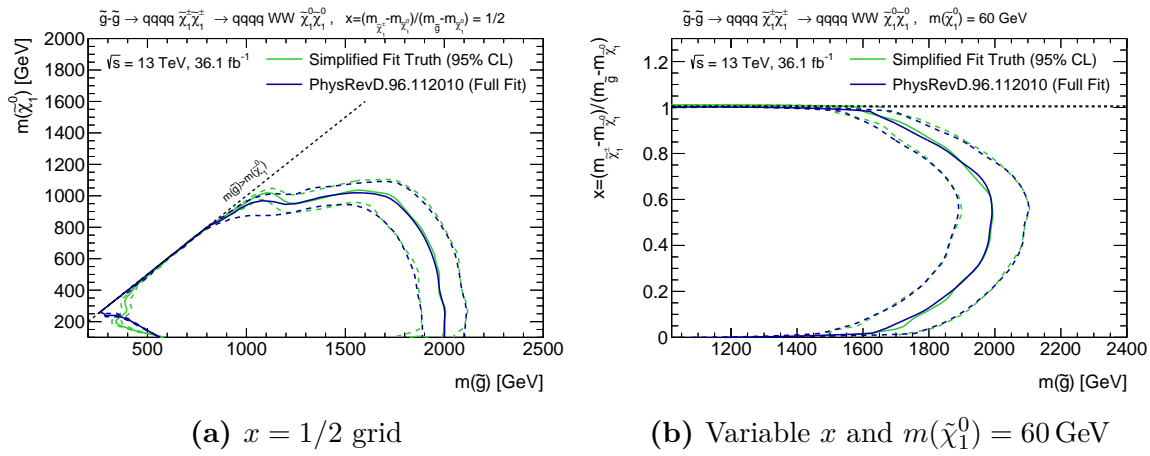


Figure 7.9: Comparison of the exclusion contour (solid line) obtained with the simplified fit (orange curve) and the full analysis fit (dark blue curve). The simplified setup uses smeared truth samples while the full analysis fit used fully reconstructed MC signal samples. All contours are drawn at 95% CL and expected CL_s values are used. The dashed lines show the $\pm 1\sigma$ variations. Good agreement is found between the simplified and the full setup. Figure (a) shows the signal grid with $x = 1/2$ and fig. (b) shows the signal grid with variable x and $m(\tilde{\chi}_1^0) = 60$ GeV.

towards an R-parity violating simplified model that has already been interpreted in an analysis searching for supersymmetry in final states with one lepton and high jet multiplicities [96].

Smeared truth signal samples

As a next step, smeared truth instead of full-reconstruction samples are used with the simplified fit setup. The results for both gluino grids are shown in fig. 7.9. Still, a good agreement is found between the simplified fit and the full analysis setup. In the $x = 1/2$ grid (fig. 7.9(a)), the same interpolation artefacts as before are visible. Additionally, the exclusion contour in the grid with variable x (fig. 7.9(b)) obtained with the smeared truth samples and the simplified fit is not as smooth as the full analysis fit result. This can be explained by the fact that several truth samples for signal points around the exclusion limit have not been available any more, preventing a smooth interpolation between the signal points due to the increased interpolation distance. A representation of the available MC truth samples can be seen in appendix B.3.

This concludes the final step of the validation procedure laid out in fig. 7.1, verifying that a simplified shape fit using smeared truth samples can successfully and efficiently, in terms of needed CPU-time, reproduce the results from a full analysis fit by making use of the fact that an estimation of the background and the systematic uncertainties is already publicly available. As a final step, the simplified shape fit procedure is applied on a large number of models sampled from the pMSSM.

7.4 Application on pMSSM signal samples

7.4.1 Model generation

Sampling the 19 dimensional pMSSM parameter space at regular intervals would be computationally inefficient. Instead, the parameter space is probed by choosing random values for each parameter. The ranges used to scan the pMSSM parameters are listed in appendix B.3 and are bound from above by the requirement that they should be in reach of the LHC. Each unique set of the 19 parameters corresponds to a single model point in the parameter space and is required to exactly conserve R-parity and have the lightest neutralino as LSP.

After the sampling of the parameters, the properties of each model are calculated with a variety of publicly available software packages[†]. Each sampled signal point is subsequently required to fulfil a range of experimental and theoretical requirements [28]. Model points are only accepted if they have consistent electroweak symmetry breaking and a scalar potential that does not break colour or electric charge. Additionally, the squared-mass values of all the particles must be positive. Furthermore, models, where `SoftSUSY` [97] — a program that calculates the SUSY particle spectrum — reports theoretical pathologies, are also discarded. Finally, a series of experimental constraints are applied, discussed in detail in Ref. [28]. They include precision electroweak and flavour constraints, dark matter constraints as well as collider constraints from LEP and the LHC.

For the set of models fulfilling the requirements, cross-sections are computed and events are generated. A truth-level analysis including the application of smearing methods is performed with `SimpleAnalysis`. Finally, the expected pMSSM yields are compared to 36.1 fb^{-1} of ATLAS data.

For this work, the result from 61617 pMSSM models have been available and are discussed in the following.

7.4.2 Observed exclusion power improvement

For each considered pMSSM model, an observed CL_s value can be computed by comparing the pMSSM yields to data through the simplified shape fit. Figure 7.10(a) shows a histogram of the observed CL_s values for all models. As a comparison, the results achieved with the discovery SRs (that were previously implemented in the scan) are also included. Models with $CL_s < 0.5$ are considered to be excluded. As expected, the simplified shape fit significantly increases the number of models that can be excluded.

The scatter plot shown in fig. 7.10(b) confirms that in every case (except one single model), the simplified shape fit achieves lower CL_s values than the discovery SRs. Table 7.2 summarises the number of models excluded by the discovery SRs and the simplified

[†] A description (slightly outdated in terms of the used software versions) can be found in Ref. [28].

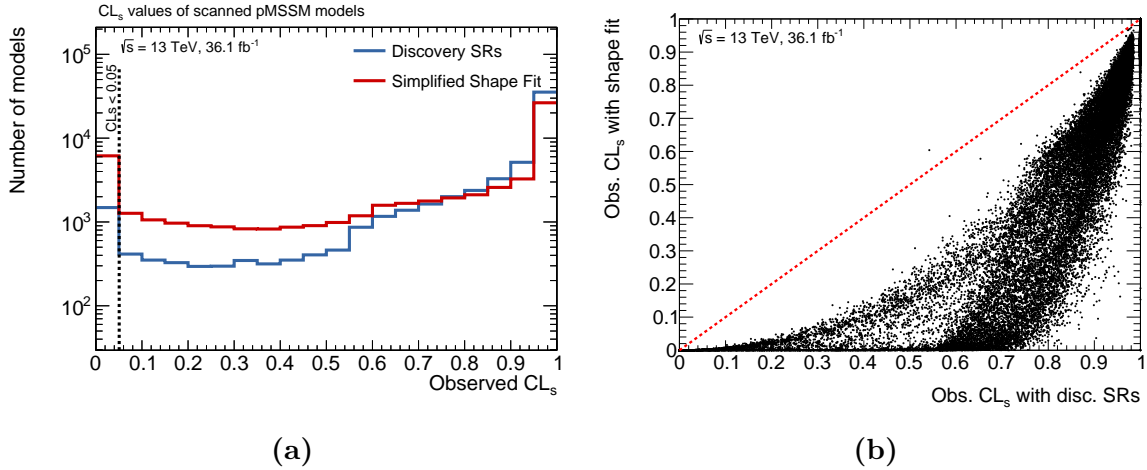


Figure 7.10: Observed CL_s values for the scanned pMSSM models. Both the results from the simplified shape and the discovery SRs are shown. In fig. (a), the models are binned into their observed CL_s values and the dashed line indicates the $CL_s < 0.05$ threshold needed for exclusion. In fig. (b), a 2-dimensional scatter plot is shown. Each sampled model corresponds to a single point in the scatter plot. All models (except one) lie below the red diagonal, indicating that the shape fit is always better than the discovery SRs.

shape fit, respectively. It shows that, by using the simplified shape fit, four times more models can be excluded. In total, 10% of the sampled models can be excluded through the simplified shape fit, but only 2.4% with the discovery SRs when comparing with ATLAS data.

Figure 7.11 compares the pMSSM model exclusion to the gluino and squark exclusion contours obtained in the nominal analysis by interpreting data with simplified gluino and squark pair-production models (shown as orange contour). The pMSSM models are binned in $m_{\tilde{g}}/m_{\tilde{q}}$ and $m_{\tilde{\chi}_1^0}$ and a number indicates how many models fall in each bin. The colour codes the fraction of pMSSM models in each bin that are excluded through the strong 1-lepton analysis using the simplified shape fit. Bins coloured in black contain only excluded models.

In the gluino grid in fig. 7.11(a), although slightly weaker, the exclusion power to pMSSM models follows more or less the shape of the exclusion limit obtained with the simplified

Table 7.2: Number of models excluded by the discovery SRs and the simplified shape fit. The values in parentheses correspond to the relative number of excluded models.

CL_s	Number (percentage) of excluded models	
	Discovery SRs	Simplified shape fit
Expected	1415 (2.3%)	6637 (10.8%)
Observed	1485 (2.4%)	6150 (10.0%)

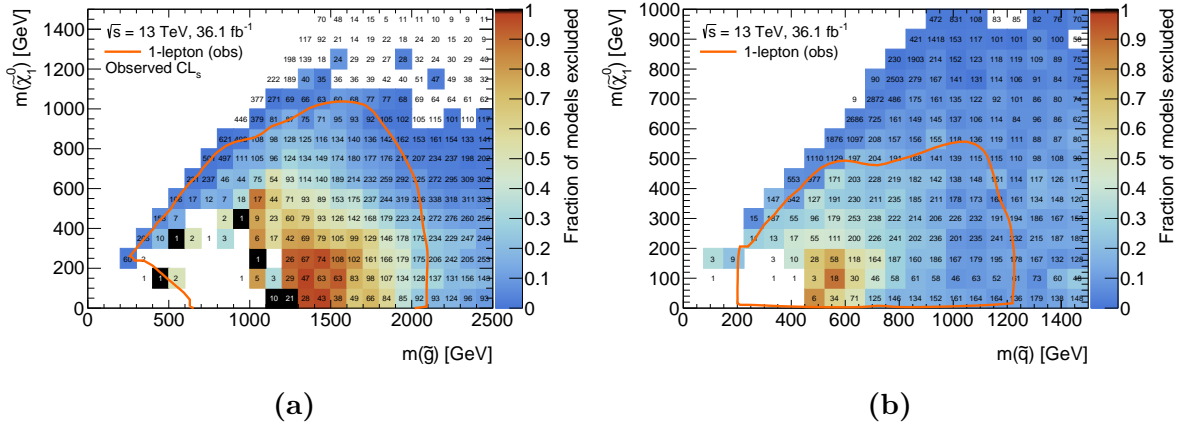


Figure 7.11: Results of the pMSSM scan in the two-dimensional space spanned by the masses of the gluino/squark and the LSP in each model. Each bin is labelled with a number indicating how many sampled models fall into the bin (without any preselection). The colour axis indicates the percentage of these models excluded by the simplified fit in each bin. Bins where all models are excluded are painted in black. Bins with no exclusion are left white. The orange contour is the observed exclusion contour of the strong 1-lepton analysis for the gluino/squark $x = 1/2$ grid at 95% CL.

models. For relatively light LSPs with masses below 300 GeV, and gluino masses up to 1.6 TeV, more than 90% of the non-compressed pMSSM models can be excluded. At gluino masses of 2 TeV, the analysis is still able to exclude roughly 40% to 50% of the sampled models with relatively light LSPs. As the mass of the LSP increases, the exclusion power decreases. The rate of decrease is slightly faster for pMSSM models than for the simplified models, resulting in a region at $m_{\tilde{\chi}_1^0} \approx 700$ GeV and $m_{\tilde{g}} \approx 1.9$ TeV where the discrepancy of the exclusion power between the pMSSM and the simplified models is slightly larger. The sensitivity to pMSSM models also decreases when approaching the diagonal. Although the analysis is in general sensitive to extremely compressed simplified models with $m_{\tilde{g}} < 900$ GeV, nearly no sensitivity to pMSSM models is observed in that region and the fraction of excluded models drops to below 1%. The reason for this discrepancy is further discussed in section 7.4.3.

In the squark grid in fig. 7.11(b), the correspondence between the results from the simplified models and the exclusion power to the pMSSM models is in general not as good as in the $m_{\tilde{g}} - m_{\tilde{\chi}_1^0}$ plane. Up to $m_{\tilde{\chi}_1^0} \approx 100$ GeV and $m_{\tilde{g}} \approx 600$ GeV, the majority of the pMSSM models can still be excluded. A decrease of sensitivity towards compressed models can be observed.

Although the simplified squark one-step model used in the strong 1-lepton analysis explicitly only considers first and second generation squark production and therefore the nominal 1-lepton analysis is optimised for first and second generation squarks, fig. 7.12 shows that decent sensitivity to stop and sbottom quarks is also achieved. Up to

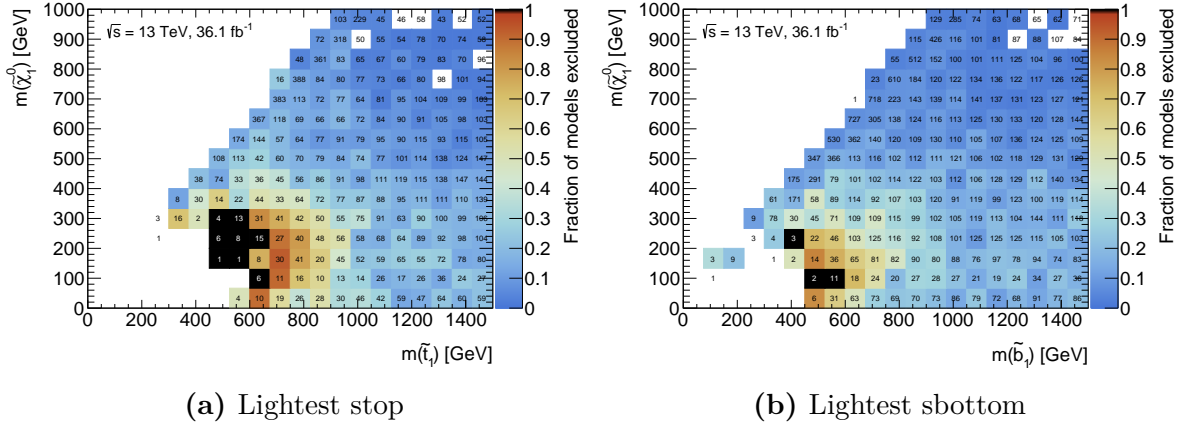


Figure 7.12: Sensitivity of the strong 1-lepton analysis to third generation squarks.

$m_{\tilde{t}_1} = 800$ GeV (see fig. 7.12(a)) and $m_{\tilde{b}_1} = 650$ GeV (see fig. 7.12(b)), the majority of the pMSSM models with relatively light LSPs can still be excluded.

7.4.3 Future prospects

In section 7.4.2, the increase in exclusion power compared to discovery SRs as well as representations of the sensitivity in different two-dimensional planes have been discussed. Despite the higher exclusion power of the simplified shape fit compared to the discovery SRs, the analysis still has a very low sensitivity ($CL_s > 0.9$) to many sampled models. Instead of looking at models where the analysis is able to achieve at least some sensitivity or even exclusion, it could potentially be interesting to investigate the models where the analysis is not able to achieve any sensitivity. Studying these models and explaining why no sensitivity is achieved, could reveal blind spots or possibilities for future improvement of the analysis.

Figure 7.13 summarises where the models with low sensitivity are located in the $m_{\tilde{g}} - m_{\tilde{\chi}_1^0}$ plane. Only models that have not been excluded by the strong 1-lepton analysis are used to fill the bins of the histogram. The colour determines how many of these models also have $CL_s > 0.9$, i.e. very low sensitivity using the simplified shape fit. The specific value of $CL_s > 0.9$ is chosen to illustrate the distribution of models that have not only narrowly missed the exclusion, but show no sensitivity at all. Additionally, as can be seen in fig. 7.10(a), the large majority of models has $CL_s > 0.9$, making it appealing to investigate their distribution in the $m_{\tilde{g}} - m_{\tilde{\chi}_1^0}$ plane. Up to $m_{\tilde{\chi}_1^0} = 500$ GeV and $m_{\tilde{g}} = 1$ TeV, i.e. in mass ranges where most models are already excluded, all of the remaining non-excluded models show very low sensitivity, although cross-sections are in principle still relatively high. This indicates that these are models where only very few events satisfy the SR requirements and where it is a priori difficult (or even impossible) to be sensitive

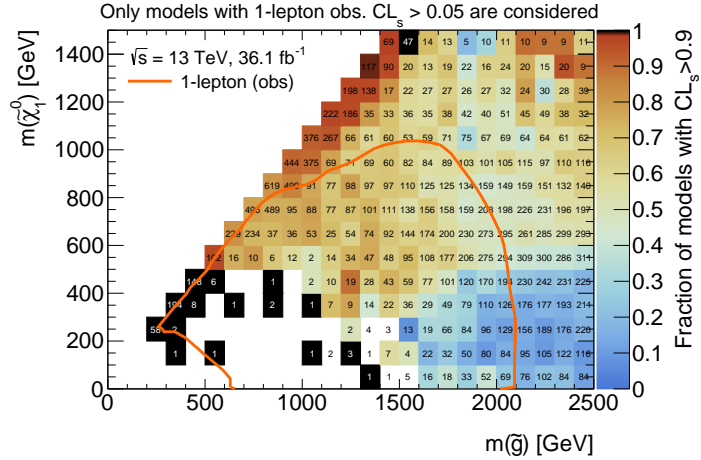


Figure 7.13: Distribution of the pMSSM models where the strong 1-lepton analysis has very low sensitivity, i.e. $CL_s > 0.9$. Only models with $CL_s > 0.05$ are used to fill the bins. The colour codes the fraction of the models where $CL_s > 0.9$. The exclusion contour obtained with the simplified model is shown as reference.

with the 1-lepton analysis and where a slight increase in data is not likely to suddenly result in exclusion.

This observation can be further investigated by the plots in fig. 7.14. In fig. 7.14(a) the fraction of low-sensitivity models that have a lepton in less than 0.05% of all events is shown. Figure 7.14(b) shows the fraction of low-sensitivity models with less than ten total events with a lepton in the final state. It is visible that the majority of the remaining low-sensitivity models within the simplified model exclusion contour and especially models towards more compressed scenarios already fail to produce enough events with a lepton in the final state. Any other SR cut apart from the lepton requirement is ignored. Even when lowering the respective thresholds to 0.01% in fig. 7.14(c) and three total events in fig. 7.14(d) and still not applying any other cuts, the majority of the low-sensitivity models are still below these requirements. Thus, the lack of sensitivity towards compressed models can be explained by the fact that most of these models do not produce enough events with a lepton in the final state. Such models are intrinsically difficult to discover or exclude with a search that explicitly requires a lepton in the final state. Most importantly, however, this rules out a lack of coverage of model characteristics or a blind spot of the analysis as the cause of low sensitivity for these models. For the non-excluded models well within the simplified model exclusion contour but not covered by the explanation of not producing enough final states with a lepton, more detailed event-wise information would be needed in order to investigate the reason for the low-sensitivity.

In figs. 7.14(e) and 7.14(f), the fraction of non-excluded models with less than 100 events with at least 6 jets and less than 100 events with $E_T^{\text{miss}} > 600 \text{ GeV}$, respectively, is shown[†]. Although the requirements of at least 6 jets or $E_T^{\text{miss}} > 600 \text{ GeV}$ are relatively tight when compared to the SR requirements in the strong 1-lepton analysis, only very few pMSSM models produce less than 100 events. It can therefore be concluded, that the requirements on the jet multiplicity and E_T^{miss} , contrary to requiring exactly one lepton, do not significantly restrict the sensitivity to pMSSM models.

Additionally, fig. 7.13 reveals that, from the non-excluded models with relatively high gluino mass and LSPs with $m_{\tilde{\chi}_1^0} < 500 \text{ GeV}$, only a small fraction has $CL_s > 0.9$, implying that there are still quite a lot of models left where the analysis achieves some sensitivity. Therefore, with 140 fb^{-1} of data being available by the end of Run-2, the number of excluded models in that region can be expected to noticeably increase.

[†] The exact values of the jet multiplicity and E_T^{miss} requirements are chosen following the relatively restricted information available from the pMSSM scan and with the objective to illustrate that even tight requirements do not significantly constrain the number of pMSSM models.

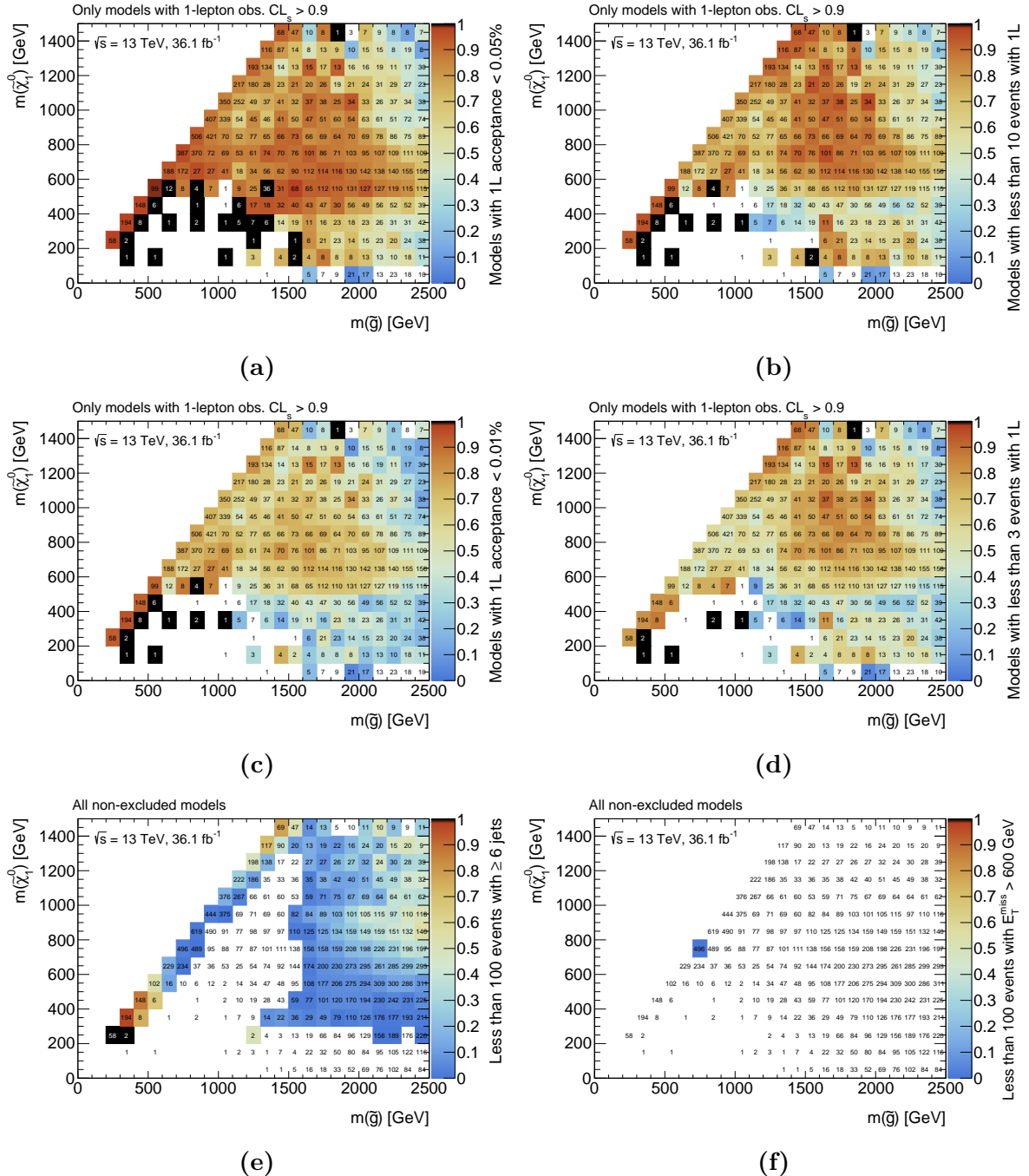


Figure 7.14: Influence of different requirements. The colour of each bin in fig. (a) indicates the fraction of the models that have a lepton in the final state in less than 0.05% of all events. In fig. (c) this threshold is lowered to 0.01% of all events. In fig. (b) the colour indicates the fraction of models that have less than ten events with a lepton in the final state. Figure (d) lowers this threshold to three total events. In fig. (e), the colour indicates the fraction of non-excluded models with less than 100 events with at least 6 jets in the final state. Figure (f) shows the fraction of non-excluded models with less than 100 events with $E_T^{\text{miss}} > 600 \text{ GeV}$. In each figure, apart from the mentioned requirement, no additional cuts are applied.

Chapter 8

Summary

Supersymmetry is a class of theories that extends the Standard Model by introducing a symmetry between bosons and fermions. It provides an elegant way to resolve some of the open questions of the Standard Model and, although no supersymmetric particles have been discovered so far, is one of the most promising extensions to the Standard Model. However, even the Minimal Supersymmetric Standard Model has more than 100 free parameters, which is too much to be scanned completely and compared to data.

Therefore, SUSY searches at ATLAS usually employ simplified models, where only a small set of supersymmetric particles and parameters are studied. All other supersymmetric particles, not explicitly participating in the considered decay chains, are set to be kinematically unreachable. In this work, several ideas to search and approaches for SUSY have been presented. Most of the work presented is based on an analysis searching for SUSY in events with exactly one isolated lepton, at least two jets and missing transverse momentum. Previous experiences have shown that this analysis is highly sensitive to the strong production of gluinos and squarks while remaining model independent to a large degree. Additionally, a similar electroweak analysis has shown that sensitivity to electroweak production of SUSY particles can be achieved for a specific simplified model studying the decays of $\tilde{\chi}_1^\pm \tilde{\chi}_2^0 \rightarrow \tilde{\chi}_1^0 \tilde{\chi}_1^0 W h$ with $W \rightarrow \ell\nu$ and $h \rightarrow b\bar{b}$.

The first study presented in this work aims to assess the sensitivity to models featuring the electroweak production of two charginos with decays to neutralinos and W bosons. The advantage of this generic model is that it does not include distinctive decays like $h \rightarrow b\bar{b}$, allowing a potential future analysis to remain more model-independent. However, this also implies that a lower sensitivity is expected due to the lack of discriminating model characteristics. Although various analysis techniques have been tested and an integrated luminosity of 140 fb^{-1} is considered, the sensitivity to this model remains at relatively low levels. Nonetheless, the model is further pursued as even higher luminosities will yield better sensitivity and, additionally, a combination with other analyses could be considered, allowing to make a statement about this model for the first time in the 1-lepton channel.

By exploiting the differing shapes of the m_T distribution with multi-bin techniques, models with chargino masses up to 500 GeV (and potentially more) or lightest neutralino masses of roughly 40 GeV could be excluded in case no significant excess is seen in data corresponding to 140 fb^{-1} . Compared to an analysis searching for supersymmetry in events with two leptons using the same simplified model and data corresponding to an integrated luminosity of 80.5 fb^{-1} [78], slightly higher chargino masses but lower lightest neutralino masses can be excluded with this approach. Machine learning techniques are not found to significantly increase the sensitivity compared to multi-bin likelihood fits. In general, the achieved significances largely depend on the available Monte Carlo statistics for estimating the $W + \text{jets}$ background, the dominant background in many interesting kinematic regions. With more statistics available later in Run-2 of the LHC and/or with data-driven techniques to estimate the $W + \text{jets}$ background, the sensitivity could therefore potentially be further increased.

Instead of using simplified models, the number of parameters of the MSSM can be reduced by setting a number of constraints. The phenomenological MSSM (pMSSM) only contains 19 free parameters that can be systematically scanned and compared to ATLAS data. In a second part of this work, an approximation of the published strong 1-lepton analysis has been presented. With the introduced simplified shape fit procedure, a computationally efficient and precise statement about the sensitivity of the analysis to a large number of other supersymmetric models can be made for the first time. Apart from reinterpretation studies using other simplified models, this approximation allows to interpret the analysis in a large number of different models belonging to the pMSSM, resulting in a more appropriate representation of the analysis in a scan of the pMSSM than has been previously possible.

Bibliography

- [1] J.-L. Gervais and B. Sakita, “Field Theory Interpretation of Supergauges in Dual Models,” *Nucl. Phys.* **B34** (1971) 632–639. [,154(1971)].
- [2] M. Slawinska, “High-luminosity LHC prospects with the upgraded ATLAS detector,” *PoS DIS2016* (2016) 266, [arXiv:1609.08434 \[hep-ex\]](https://arxiv.org/abs/1609.08434).
- [3] Rayleigh, “Joseph john thomson, 1856 - 1940,” *Obituary Notices of Fellows of the Royal Society* **3** no. 10, (1941) 587–609,
<http://rsbm.royalsocietypublishing.org/content/3/10/587.full.pdf>.
<http://rsbm.royalsocietypublishing.org/content/3/10/587>.
- [4] D. J. Griffiths, *Introduction to elementary particles; 2nd rev. version.* Physics textbook. Wiley, New York, NY, 2008. <https://cds.cern.ch/record/111880>.
- [5] M. E. Peskin and D. V. Schroeder, *An Introduction to quantum field theory.* Addison-Wesley, Reading, USA, 1995.
<http://www.slac.stanford.edu/~mpeskin/QFT.html>.
- [6] E. Noether and M. A. Tavel, “Invariant variation problems,”
[arXiv:physics/0503066](https://arxiv.org/abs/physics/0503066).
- [7] C. N. Yang and R. L. Mills, “Conservation of isotopic spin and isotopic gauge invariance,” *Phys. Rev.* **96** (Oct, 1954) 191–195.
<https://link.aps.org/doi/10.1103/PhysRev.96.191>.
- [8] C. Patrignani and P. D. Group, “Review of particle physics,” *Chinese Physics C* **40** no. 10, (2016) 100001. <http://stacks.iop.org/1674-1137/40/i=10/a=100001>.
- [9] **Super-Kamiokande** Collaboration, Y. Fukuda *et al.*, “Evidence for oscillation of atmospheric neutrinos,” *Phys. Rev. Lett.* **81** (1998) 1562–1567,
[arXiv:hep-ex/9807003 \[hep-ex\]](https://arxiv.org/abs/hep-ex/9807003).
- [10] Z. Maki, M. Nakagawa, and S. Sakata, “Remarks on the unified model of elementary particles,” *Prog. Theor. Phys.* **28** (1962) 870–880. [,34(1962)].
- [11] M. Kobayashi and T. Maskawa, “CP Violation in the Renormalizable Theory of Weak Interaction,” *Prog. Theor. Phys.* **49** (1973) 652–657.
- [12] Y. Nambu, “Quasiparticles and Gauge Invariance in the Theory of Superconductivity,” *Phys. Rev.* **117** (1960) 648–663. [,132(1960)].

- [13] J. Goldstone, “Field Theories with Superconductor Solutions,” *Nuovo Cim.* **19** (1961) 154–164.
- [14] S. P. Martin, “A Supersymmetry primer,” [arXiv:hep-ph/9709356 \[hep-ph\]](https://arxiv.org/abs/hep-ph/9709356). [Adv. Ser. Direct. High Energy Phys.18,1(1998)].
- [15] V. C. Rubin and W. K. Ford, Jr., “Rotation of the Andromeda Nebula from a Spectroscopic Survey of Emission Regions,” *Astrophys. J.* **159** (1970) 379–403.
- [16] D. Clowe, M. Bradac, A. H. Gonzalez, M. Markevitch, S. W. Randall, C. Jones, and D. Zaritsky, “A direct empirical proof of the existence of dark matter,” *Astrophys. J.* **648** (2006) L109–L113, [arXiv:astro-ph/0608407 \[astro-ph\]](https://arxiv.org/abs/astro-ph/0608407).
- [17] E. W. Kolb, “Particle Physics Foundations of Dark Matter, Dark Energy, and Inflation (2/3).”, <http://cds.cern.ch/record/1447482>.
- [18] Planck Mission, “Cosmic microwave background.” <http://planck.cf.ac.uk/results/cosmic-microwave-background>, March, 2013. Accessed: 2018-07-06.
- [19] R. Frezzotti, M. Garofalo, and G. Rossi, “Nonsupersymmetric model with unification of electroweak and strong interactions,” *Phys. Rev.* **D93** no. 10, (2016) 105030, [arXiv:1602.03684 \[hep-ph\]](https://arxiv.org/abs/1602.03684).
- [20] S. Coleman and J. Mandula, “All possible symmetries of the s matrix,” *Phys. Rev.* **159** (Jul, 1967) 1251–1256. <https://doi.org/10.1103/PhysRev.159.1251>.
- [21] R. Haag, J. T. Lopuszanski, and M. Sohnius, “All Possible Generators of Supersymmetries of the s Matrix,” *Nucl. Phys.* **B88** (1975) 257. [,257(1974)].
- [22] C. Csáki and P. Tanedo, “[Beyond the Standard Model](#),” in *Proceedings, 2013 European School of High-Energy Physics (ESHEP 2013): Paradfurdo, Hungary, June 5-18, 2013*, pp. 169–268. 2015. [arXiv:1602.04228 \[hep-ph\]](https://arxiv.org/abs/1602.04228). <https://inspirehep.net/record/1422131/files/arXiv:1602.04228.pdf>.
- [23] **Super-Kamiokande** Collaboration, K. Abe *et al.*, “Search for proton decay via $p \rightarrow e^+ \pi^0$ and $p \rightarrow \mu^+ \pi^0$ in 0.31 megaton-years exposure of the Super-Kamiokande water Cherenkov detector,” *Phys. Rev.* **D95** no. 1, (2017) 012004, [arXiv:1610.03597 \[hep-ex\]](https://arxiv.org/abs/1610.03597).
- [24] J. Alwall, P. Schuster, and N. Toro, “Simplified Models for a First Characterization of New Physics at the LHC,” *Phys. Rev.* **D79** (2009) 075020, [arXiv:0810.3921 \[hep-ph\]](https://arxiv.org/abs/0810.3921).
- [25] **LHC New Physics Working Group** Collaboration, D. Alves, “Simplified Models for LHC New Physics Searches,” *J. Phys.* **G39** (2012) 105005, [arXiv:1105.2838 \[hep-ph\]](https://arxiv.org/abs/1105.2838).
- [26] **ATLAS** Collaboration, “Search for squarks and gluinos in events with an isolated lepton, jets, and missing transverse momentum at $\sqrt{s} = 13$ TeV with the ATLAS detector,” *Phys. Rev.* **D96** no. 11, (2017) 112010, [arXiv:1708.08232 \[hep-ex\]](https://arxiv.org/abs/1708.08232).

- [27] **MSSM Working Group** Collaboration, A. Djouadi *et al.*, “The Minimal supersymmetric standard model: Group summary report,” in *GDR (Groupement De Recherche) - Supersymetrie Montpellier, France, April 15-17, 1998.* 1998. [arXiv:hep-ph/9901246 \[hep-ph\]](https://arxiv.org/abs/hep-ph/9901246).
https://inspirehep.net/record/481987/files/arXiv:hep-ph_9901246.pdf.
- [28] **ATLAS** Collaboration, “Summary of the ATLAS experiment’s sensitivity to supersymmetry after LHC Run 1 — interpreted in the phenomenological MSSM,” *JHEP* **10** (2015) 134, [arXiv:1508.06608 \[hep-ex\]](https://arxiv.org/abs/1508.06608).
- [29] CERN, “About cern.” <http://cds.cern.ch/record/1997225>. Accessed: 2018-07-11.
- [30] CERN, “LHC Guide.” Mar, 2017.
- [31] L. R. Evans and P. Bryant, “LHC Machine,” *JINST* **3** (2008) S08001. 164 p.
<http://cds.cern.ch/record/1129806>. This report is an abridged version of the LHC Design Report (CERN-2004-003).
- [32] **ATLAS** Collaboration, “ATLAS Public Results - Luminosity Public Results Run 1.” <https://twiki.cern.ch/twiki/bin/view/AtlasPublic/LuminosityPublicResults>. Accessed: 2018-07-17.
- [33] **ATLAS** Collaboration, “ATLAS Public Results - Luminosity Public Results Run 2.” <https://twiki.cern.ch/twiki/bin/view/AtlasPublic/LuminosityPublicResultsRun2>. Accessed: 2018-07-17.
- [34] E. Mobs, “The CERN accelerator complex. Complexe des accélérateurs du CERN.” <https://cds.cern.ch/record/2197559>. General Photo.
- [35] **ATLAS** Collaboration, “The ATLAS Experiment at the CERN Large Hadron Collider,” *JINST* **3** (2008) S08003.
- [36] **ATLAS** Collaboration, “ATLAS: Detector and physics performance technical design report. Volume 1.”
- [37] **Particle Data Group** Collaboration, M. Tanabashi *et al.*, “Review of Particle Physics,” *Phys. Rev.* **D98** (2018) 030001. <http://pdg.lbl.gov>.
- [38] J. Pequenao, “Computer generated image of the whole ATLAS detector.” Mar, 2008.
- [39] **ATLAS** Collaboration, “ATLAS Insertable B-Layer Technical Design Report,” Tech. Rep. CERN-LHCC-2010-013. ATLAS-TDR-19, Sep, 2010.
<http://cds.cern.ch/record/1291633>.
- [40] **ATLAS** Collaboration, F. Pastore, “ATLAS Run-2 status and performance,” *Nucl. Part. Phys. Proc.* **270-272** (2016) 3–7.
- [41] **ATLAS** Collaboration, A. R. Martínez, “The Run-2 ATLAS Trigger System,” *J. Phys. Conf. Ser.* **762** no. 1, (2016) 012003.
- [42] S. Weinzierl, “Introduction to Monte Carlo methods,” [arXiv:hep-ph/0006269 \[hep-ph\]](https://arxiv.org/abs/hep-ph/0006269).

- [43] M. H. Seymour and M. Marx, “Monte Carlo Event Generators,” in *Proceedings, 69th Scottish Universities Summer School in Physics : LHC Phenomenology (SUSSP69): St.Andrews, Scotland, August 19-September 1, 2012*, pp. 287–319. 2013. [arXiv:1304.6677 \[hep-ph\]](https://arxiv.org/abs/1304.6677).
<https://inspirehep.net/record/1229804/files/arXiv:1304.6677.pdf>.
- [44] J. Bellm *et al.*, “Herwig 7.0/Herwig++ 3.0 release note,” *Eur. Phys. J.* **C76** no. 4, (2016) 196, [arXiv:1512.01178 \[hep-ph\]](https://arxiv.org/abs/1512.01178).
- [45] T. Sjostrand, S. Mrenna, and P. Z. Skands, “PYTHIA 6.4 Physics and Manual,” *JHEP* **05** (2006) 026, [arXiv:hep-ph/0603175 \[hep-ph\]](https://arxiv.org/abs/hep-ph/0603175).
- [46] N. M. Hartmann, *Search for Supersymmetry in events with an isolated lepton, at least 2-9 jets and missing transverse momentum with the ATLAS detector*. PhD thesis, Munich U., 2018. https://www.etp.physik.uni-muenchen.de/publications/theses/download/phd_nhartmann.pdf.
- [47] GEANT4 Collaboration, S. Agostinelli *et al.*, “GEANT4: A Simulation toolkit,” *Nucl. Instrum. Meth.* **A506** (2003) 250–303.
- [48] ATLAS Collaboration, “The ATLAS Simulation Infrastructure,” *Eur. Phys. J.* **C70** (2010) 823–874, [arXiv:1005.4568 \[physics.ins-det\]](https://arxiv.org/abs/1005.4568).
- [49] T. Gleisberg, S. Hoeche, F. Krauss, M. Schonherr, S. Schumann, F. Siegert, and J. Winter, “Event generation with SHERPA 1.1,” *JHEP* **02** (2009) 007, [arXiv:0811.4622 \[hep-ph\]](https://arxiv.org/abs/0811.4622).
- [50] S. Alioli, P. Nason, C. Oleari, and E. Re, “A general framework for implementing NLO calculations in shower Monte Carlo programs: the POWHEG BOX,” *JHEP* **06** (2010) 043, [arXiv:1002.2581 \[hep-ph\]](https://arxiv.org/abs/1002.2581).
- [51] T. Sjöstrand, S. Ask, J. R. Christiansen, R. Corke, N. Desai, P. Ilten, S. Mrenna, S. Prestel, C. O. Rasmussen, and P. Z. Skands, “An Introduction to PYTHIA 8.2,” *Comput. Phys. Commun.* **191** (2015) 159–177, [arXiv:1410.3012 \[hep-ph\]](https://arxiv.org/abs/1410.3012).
- [52] J. Alwall, R. Frederix, S. Frixione, V. Hirschi, F. Maltoni, O. Mattelaer, H. S. Shao, T. Stelzer, P. Torrielli, and M. Zaro, “The automated computation of tree-level and next-to-leading order differential cross sections, and their matching to parton shower simulations,” *JHEP* **07** (2014) 079, [arXiv:1405.0301 \[hep-ph\]](https://arxiv.org/abs/1405.0301).
- [53] D. Bogavac, A. Cervelli, J. Lorenz, M. D’Onofrio, Y. Gao, M. J. Sullivan, R. El Kosseifi, and S. Muanza, “Search for chargino and neutralino production in final state with one lepton, two b-jets consistent with a Higgs boson, and missing transverse momentum at $\sqrt{s} = 13$ TeV with the ATLAS detector,” Tech. Rep. ATL-COM-PHYS-2017-381, CERN, Geneva, Apr, 2017.
<https://cds.cern.ch/record/2259593>.
- [54] ATLAS Collaboration, “Selection of jets produced in 13TeV proton-proton collisions with the ATLAS detector,” Tech. Rep. ATLAS-CONF-2015-029, CERN, Geneva, Jul, 2015. <https://cds.cern.ch/record/2037702>.

- [55] **ATLAS** Collaboration, “Electron and photon energy calibration with the ATLAS detector using LHC Run 1 data,” *Eur. Phys. J.* **C74** no. 10, (2014) 3071, [arXiv:1407.5063 \[hep-ex\]](https://arxiv.org/abs/1407.5063).
- [56] **ATLAS** Collaboration, “Electron identification measurements in ATLAS using $\sqrt{s} = 13$ TeV data with 50 ns bunch spacing,” Tech. Rep. ATL-PHYS-PUB-2015-041, CERN, Geneva, Sep, 2015. <https://cds.cern.ch/record/2048202>.
- [57] **ATLAS** Collaboration, “Electron efficiency measurements with the ATLAS detector using the 2015 LHC proton–proton collision data.” ATLAS-CONF-2016-024, 2016. <https://cds.cern.ch/record/2157687>.
- [58] **ATLAS** Collaboration, “Muon reconstruction performance of the ATLAS detector in proton–proton collision data at $\sqrt{s} = 13$ TeV,” *Eur. Phys. J.* **C76** no. 5, (2016) 292, [arXiv:1603.05598 \[hep-ex\]](https://arxiv.org/abs/1603.05598).
- [59] M. Cacciari, G. P. Salam, and G. Soyez, “The Anti-k(t) jet clustering algorithm,” *JHEP* **04** (2008) 063, [arXiv:0802.1189 \[hep-ph\]](https://arxiv.org/abs/0802.1189).
- [60] M. Cacciari, G. P. Salam, and G. Soyez, “FastJet User Manual,” *Eur. Phys. J.* **C72** (2012) 1896, [arXiv:1111.6097 \[hep-ph\]](https://arxiv.org/abs/1111.6097).
- [61] **ATLAS** Collaboration, “Topological cell clustering in the ATLAS calorimeters and its performance in LHC Run 1,” *Eur. Phys. J.* **C77** (2017) 490, [arXiv:1603.02934 \[hep-ex\]](https://arxiv.org/abs/1603.02934).
- [62] **ATLAS** Collaboration, “Tagging and suppression of pileup jets with the ATLAS detector.” ATLAS-CONF-2014-018, 2014. <https://cds.cern.ch/record/1700870>.
- [63] **ATLAS** Collaboration, “Jet Calibration and Systematic Uncertainties for Jets Reconstructed in the ATLAS Detector at $\sqrt{s} = 13$ TeV.” ATL-PHYS-PUB-2015-015, 2015. <https://cds.cern.ch/record/2037613>.
- [64] **ATLAS** Collaboration, “Optimisation of the ATLAS b -tagging performance for the 2016 LHC Run.” ATL-PHYS-PUB-2016-012, 2016. <https://cds.cern.ch/record/2160731>.
- [65] **ATLAS** Collaboration, “Performance of missing transverse momentum reconstruction with the ATLAS detector using proton-proton collisions at $\sqrt{s} = 13$ TeV,” [arXiv:1802.08168 \[hep-ex\]](https://arxiv.org/abs/1802.08168).
- [66] D. Adams *et al.*, “Recommendations of the Physics Objects and Analysis Harmonisation Study Groups 2014,” Tech. Rep. ATL-PHYS-INT-2014-018, CERN, Geneva, Jul, 2014. <https://cds.cern.ch/record/1743654>.
- [67] M. Cacciari, G. P. Salam, and G. Soyez, “The Catchment Area of Jets,” *JHEP* **04** (2008) 005, [arXiv:0802.1188 \[hep-ph\]](https://arxiv.org/abs/0802.1188).
- [68] G. Cowan, K. Cranmer, E. Gross, and O. Vitells, “Asymptotic formulae for likelihood-based tests of new physics,” *Eur. Phys. J.* **C71** (2011) 1554, [arXiv:1007.1727 \[physics.data-an\]](https://arxiv.org/abs/1007.1727). [Erratum: Eur. Phys. J.C73,2501(2013)].

- [69] G. Cowan, “Discovery sensitivity for a counting experiment with background uncertainty,”
- [70] L. Moneta, K. Belasco, K. S. Cranmer, S. Kreiss, A. Lazzaro, D. Piparo, G. Schott, W. Verkerke, and M. Wolf, “The RooStats Project,” *PoS ACAT2010* (2010) 057, [arXiv:1009.1003 \[physics.data-an\]](https://arxiv.org/abs/1009.1003).
- [71] **ATLAS** Collaboration, “Search for supersymmetry using final states with one lepton, jets, and missing transverse momentum with the ATLAS detector in $\sqrt{s} = 7$ TeV pp ,” *Phys. Rev. Lett.* **106** (2011) 131802, [arXiv:1102.2357 \[hep-ex\]](https://arxiv.org/abs/1102.2357).
- [72] **ATLAS** Collaboration, X. Chen, “Prospects of LHC Higgs Physics at the end of Run III,” Tech. Rep. ATL-PHYS-PROC-2017-019, CERN, Geneva, Mar, 2017. <https://cds.cern.ch/record/2256082>.
- [73] D. Schaefer, D. M. Portillo Quintero, P. Francavilla, C. M. Macdonald, M. Petrov, and E. Tolley, “Object based Missing Transverse Momentum Significance in the ATLAS Detector,” Tech. Rep. ATL-COM-PHYS-2017-1735, CERN, Geneva, Dec, 2017. <https://cds.cern.ch/record/2294922>.
- [74] **Aachen-Annecy-Birmingham-CERN-Helsinki-London(QMC)-Paris(CdF)-Riverside-Rome-Rutherford-Saclay(CEN)-Vienna** Collaboration, G. Arnison *et al.*, “Further evidence for charged intermediate vector bosons at the SPS collider,” *Phys. Lett. B* **129** no. CERN-EP-83-111, (Jun, 1985) 273–282. 17 p. <https://cds.cern.ch/record/163856>.
- [75] E. Alpaydin, *Introduction to Machine Learning*. The MIT Press, 2nd ed., 2010.
- [76] I. Goodfellow, Y. Bengio, and A. Courville, *Deep Learning*. MIT Press, 2016. <http://www.deeplearningbook.org>.
- [77] N. Hartmann, “ahoi.” <https://gitlab.com/nikoladze/ahoi>, 2018.
- [78] **ATLAS Collaboration** Collaboration, “Search for direct chargino pair production with W-boson mediated decays in events with two leptons and missing transverse momentum at $\sqrt{s} = 13$ TeV with the ATLAS detector,” Tech. Rep. ATLAS-CONF-2018-042, CERN, Geneva, Jul, 2018. <https://cds.cern.ch/record/2632578>.
- [79] M. Baak, G. J. Besjes, D. Côte, A. Koutsman, J. Lorenz, and D. Short, “HistFitter software framework for statistical data analysis,” *Eur. Phys. J.* **C75** (2015) 153, [arXiv:1410.1280 \[hep-ex\]](https://arxiv.org/abs/1410.1280).
- [80] **ROOT** Collaboration, K. Cranmer, G. Lewis, L. Moneta, A. Shibata, and W. Verkerke, “HistFactory: A tool for creating statistical models for use with RooFit and RooStats,” Tech. Rep. CERN-OPEN-2012-016, New York U., New York, Jan, 2012. [http://cds.cern.ch/record/1456844](https://cds.cern.ch/record/1456844).
- [81] W. Verkerke and D. P. Kirkby, “The RooFit toolkit for data modeling,” *eConf C0303241* (2003) MOLT007, [arXiv:physics/0306116 \[physics\]](https://arxiv.org/abs/physics/0306116). [,186(2003)].

- [82] R. Brun and F. Rademakers, “ROOT: An object oriented data analysis framework,” *Nucl. Instrum. Meth.* **A389** (1997) 81–86.
- [83] I. Antcheva *et al.*, “Root — a c++ framework for petabyte data storage, statistical analysis and visualization,” *Computer Physics Communications* **182** no. 6, (2011) 1384 – 1385. <http://www.sciencedirect.com/science/article/pii/S0010465511000701>.
- [84] S. Linnainmaa, “Taylor expansion of the accumulated rounding error,” *BIT Numerical Mathematics* **16** no. 2, (Jun, 1976) 146–160.
<https://doi.org/10.1007/BF01931367>.
- [85] D. P. Kingma and J. Ba, “Adam: A method for stochastic optimization,” *CoRR* **abs/1412.6980** (2014) , [arXiv:1412.6980](https://arxiv.org/abs/1412.6980). <http://arxiv.org/abs/1412.6980>.
- [86] N. Hartmann, “Kerasrootclassification.” <https://gitlab.physik.uni-muenchen.de/Nikolai.Hartmann/KerasROOTClassification/>, 2018.
- [87] F. Chollet *et al.*, “Keras.” <https://keras.io>, 2015.
- [88] M. Abadi *et al.*, “TensorFlow: Large-scale machine learning on heterogeneous systems,” 2015. <https://www.tensorflow.org/>. Software available from tensorflow.org.
- [89] **ATLAS** Collaboration, “Simpleanalysis.” <https://gitlab.cern.ch/atlas-phys-susy-wg/SimpleAnalysis>, 2018.
- [90] T. Weber, *Search for gluinos with machine learning techniques using momentum components of reconstructed objects with the ATLAS detector*. Bachelor’s thesis, Munich U., 2018. https://www.etp.physik.uni-muenchen.de/publications/bachelor/download_auth_etp/bac18_tweber.pdf.
- [91] A. Wester, *Search for gauginos in final states with one lepton using machine learning techniques with simulated data of the ATLAS detector*. Bachelor’s thesis, Munich U., 2018. https://www.etp.physik.uni-muenchen.de/publications/bachelor/download_auth_etp/bac18_awester.pdf.
- [92] P. Baldi, P. Sadowski, and D. Whiteson, “Searching for Exotic Particles in High-Energy Physics with Deep Learning,” *Nature Commun.* **5** (2014) 4308, [arXiv:1402.4735 \[hep-ph\]](https://arxiv.org/abs/1402.4735).
- [93] K. Lieret, *Truth-level based estimation of the sensitivity to pMSSM models in events with one hard lepton*. Bachelor’s thesis, Munich U., 2015. https://www.etp.physik.uni-muenchen.de/publications/bachelor/download_auth_etp/bac15_klieret.pdf.
- [94] C. Chen, “New approach to identifying boosted hadronically-decaying particle using jet substructure in its center-of-mass frame,” *Phys. Rev.* **D85** (2012) 034007, [arXiv:1112.2567 \[hep-ph\]](https://arxiv.org/abs/1112.2567).
- [95] D. Bogavac, *Searches for supersymmetric particles decaying to W and Higgs bosons in events with an isolated lepton with the ATLAS detector*. PhD thesis, Munich U., 2018. https://www.etp.physik.uni-muenchen.de/publications/theses/download/phd_dbogavac.pdf.

- [96] **ATLAS** Collaboration, M. Aaboud *et al.*, “Search for new phenomena in a lepton plus high jet multiplicity final state with the ATLAS experiment using $\sqrt{s} = 13$ TeV proton-proton collision data,” *JHEP* **09** (2017) 088, [arXiv:1704.08493 \[hep-ex\]](https://arxiv.org/abs/1704.08493).
- [97] B. C. Allanach, “SOFTSUSY: a program for calculating supersymmetric spectra,” *Comput. Phys. Commun.* **143** (2002) 305–331, [arXiv:hep-ph/0104145 \[hep-ph\]](https://arxiv.org/abs/hep-ph/0104145).

Symbols

Acronyms / Abbreviations

ALICE	A Large Ion Collider Experiment, page 20
ATLAS	A Toroidal LHC ApparatuS, page 20
AtlFast-II	ATLAS fast simulation II, page 28
AUC	Area under the curve, page 72
BDT	Boosted Decision Tree, page 36
BSM	Beyond the Standard Model, page 10
CERN	Conseil Européen pour la Recherche Nucléaire, page 19
CKM	Cabibbo-Kobayashi-Maskawa, page 8
CL	Confidence level, page 42
CMS	Compact Muon Solenoid, page 20
CP	Combined performance, page 83
CSC	Cathode Strip Chambers, page 24
ECal	Electromagnetic Calorimeter, page 23
EWK	Electroweak, page 3
FCNC	Flavour-changing neutral currents, page 18
FSR	Final state radiation, page 26
Fullsim	ATLAS full detector simulation, page 28
GRL	Good Runs List, page 33
GUT	Grand unified theory, page 12
GWS	Glashow, Weinberg and Salam, page 3
HCal	Hadronic Calorimeter, page 23

HF	Heavy flavour, page 31
HLT	High Level Trigger, page 24
IBL	Insertable B-Layer, page 23
ID	Inner Detector, page 22
IP	Interaction Point, page 20
IR	Insertion Region, page 19
ISR	Initial state radiation, page 26
JVT	Jet Vertex Tagger, page 35
L1	Level 1 Trigger, page 24
LAr	Liquid Argon, page 23
LEP	Large Electron Positron Collider, page 19
LHCb	Large Hadron Collider beauty, page 20
LHCf	Large Hadron Collider forward, page 20
LHC	Large Hadron Collider, page 19
LH	Likelihood, page 34
LINAC2	Linear accelerator 2, page 20
LSP	Lightest supersymmetric particle, page 10
MC	Monte Carlo, page 26
MDT	Monitored drift tubes, page 24
ML	Maximum likelihood, page 40
MLP	Multilayer perceptron, page 70
MoEDAL	Monopole and Exotics Detector at the LHC, page 20
MS	Muon spectrometer, page 23
MSSM	Minimal Supersymmetric Standard Model, page 12
NLO	Next-to-leading order, page 27
OR	Overlap removal, page 36
PDF	Parton Distribution Function, page 26
PMNS	Pontecorvo–Maki–Nakagawa–Sakata, page 8

MSSM	Phenomenological Minimal Supersymmetric Standard Model, page 18
PS	Proton Synchrotron, page 20
QCD	Quantum chromodynamics, page 6
QED	Quantum electrodynamics, page 6
QFT	Quantum field theory, page 4
reco	Full reconstruction, page 73
RF	Radio-frequency, page 19
ROC	Receiver operator characteristic, page 52
RPC	Resistive Plate Chamber, page 24
SCT	Semiconductor Tracker, page 23
SM	Standard Model, page 3
SPS	Super Proton Synchrotron, page 20
SR	Signal region, page 62
SUSY	Supersymmetry, page 9
TGC	Thin Gap Chamber, page 24
TOTEM	Total Elastic and diffractive cross section Measurement, page 20
TRT	Transition Radiation Tracker, page 23
TST	Track soft terms, page 36
VEV	Vacuum expectation value, page 9
WIMP	Weakly interacting massive particle, page 10

Appendix A

A.1 N-1 plots for cut-scan results

In the following, a full set of N-1 plots for the cut combinations obtained in the N -dimensional cut scan presented in section 6.3 is provided. The plots show the cuts on the different observables as they are obtained by the N -dimensional cut scan, without any further manual optimisation. The significance is computed with `BinomialExpZ` by integrating the number of events in the direction of the cut-arrow and includes a 30% systematic uncertainty. In view of data-driven methods to estimate especially the $W + \text{jets}$ background, the statistical uncertainty is not included. The N-1 plots are used to further tune the requirements, i.e. remove cuts that don't improve the sensitivity noticeably and tweak some of the cuts to slightly better values. Some of the plots seem to indicate that a much higher cut value would yield a higher significance. Such cuts, however, are not chosen by the N -dimensional cut optimisation (and neither by the manual optimisation) because they fail to fulfil one or more of the statistical requirements set in section 6.3.

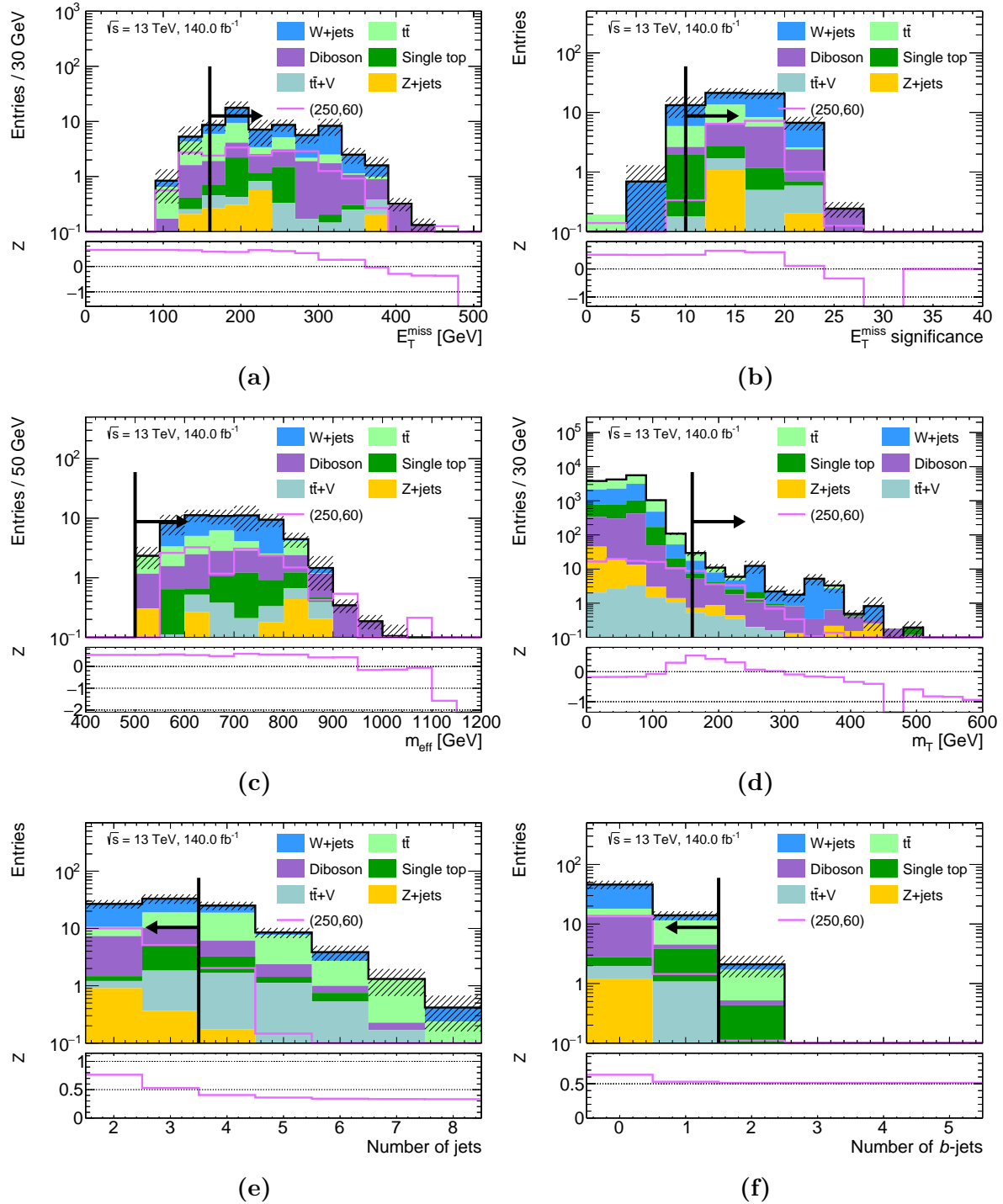


Figure A.1: First set of N-1 plots for the chosen cut combination for the **(250, 60)** signal point. These plots form the basis for a manual optimisation step that removes some of the unnecessary cuts or tweaks suboptimal cuts to better values.

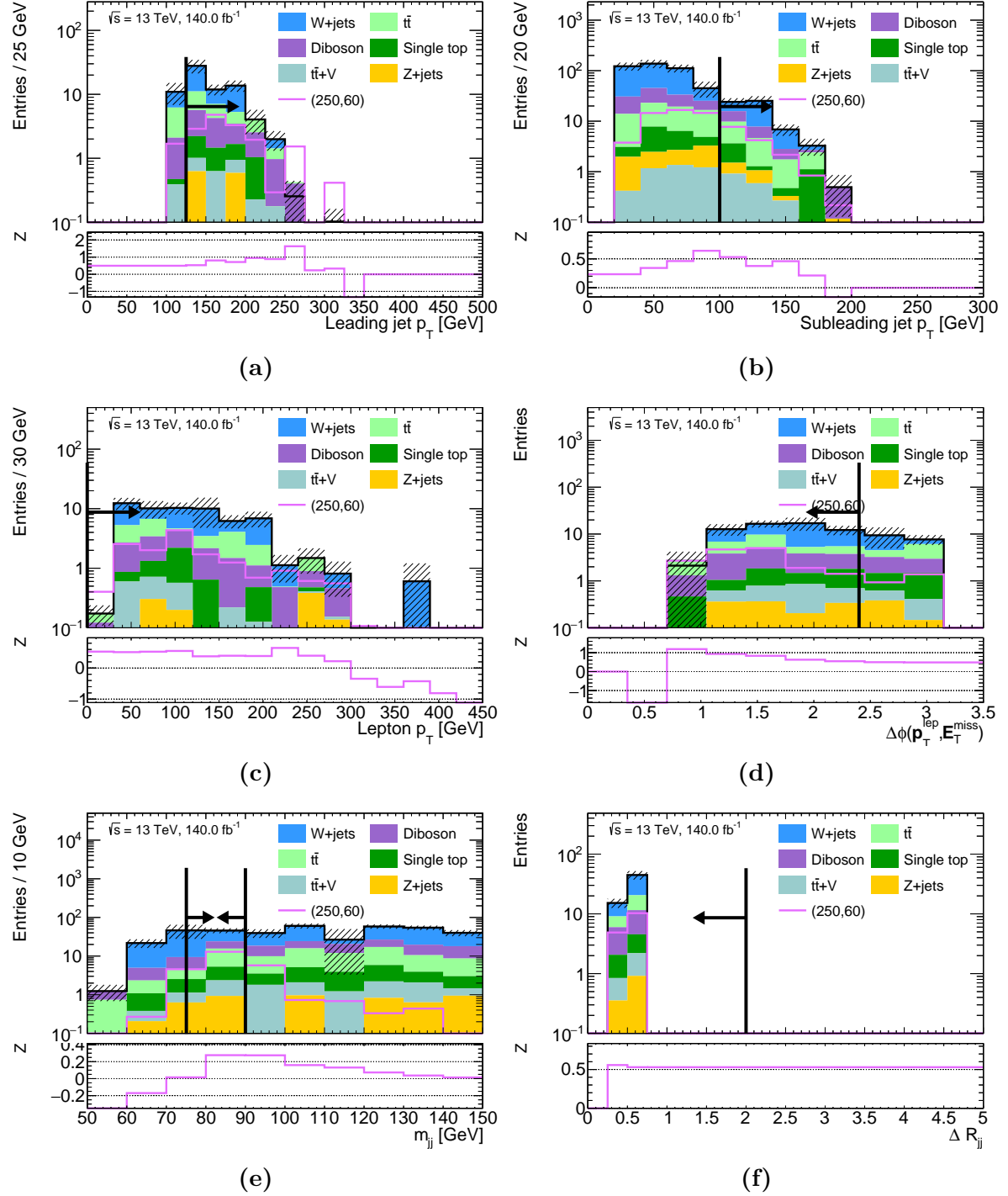


Figure A.2: Second set of N-1 plots for the chosen cut combination for the (250, 60) signal point. These plots form the basis for a manual optimisation step that removes some of the unnecessary cuts or tweaks suboptimal cuts to better values. In fig. (e), for illustration purposes, the lower requirement is not applied while the upper cut is scanned.

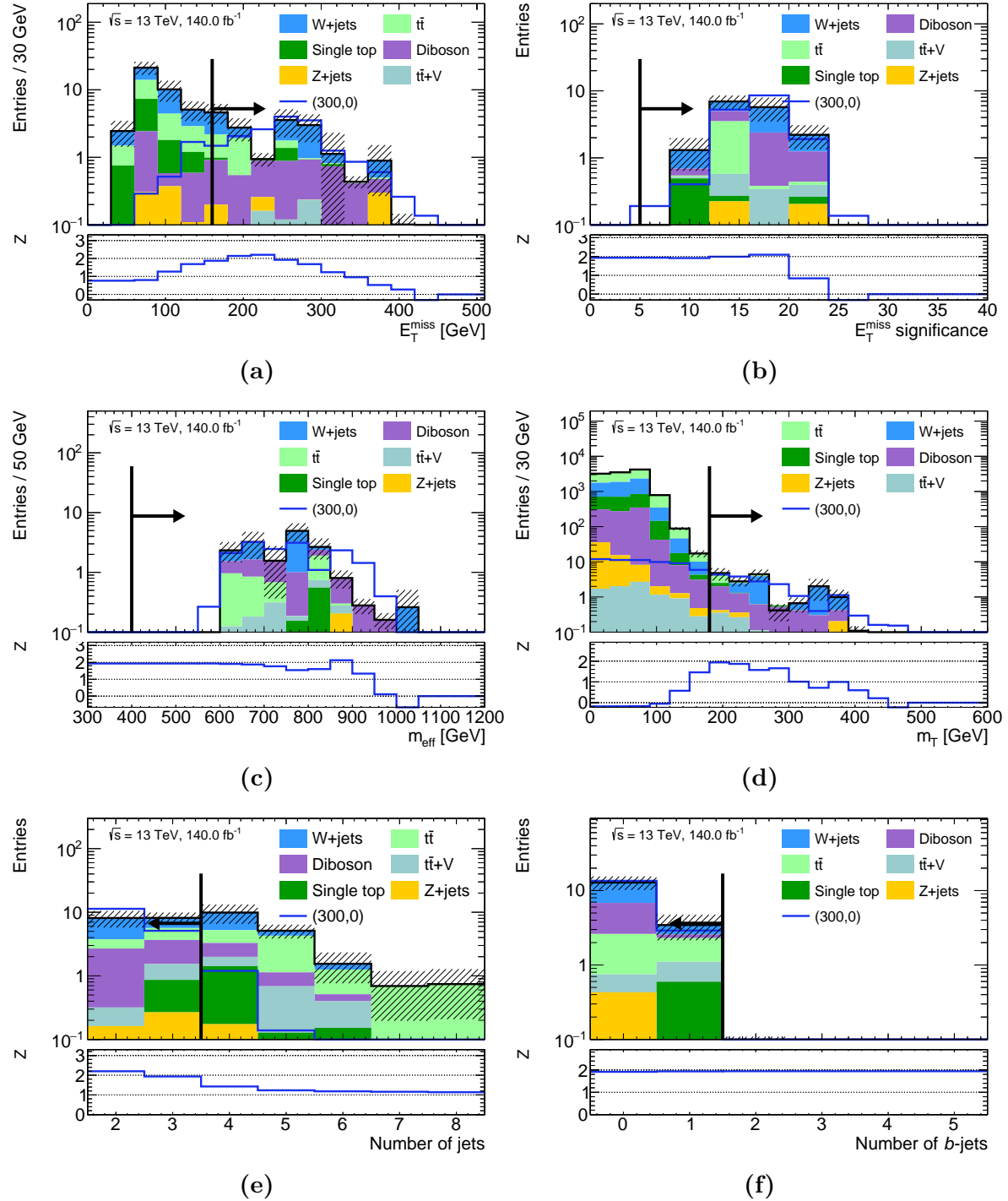


Figure A.3: First set of N-1 plots for the chosen cut combination for the **(300, 0)** signal point. These plots form the basis for a manual optimisation step that removes some of the unnecessary cuts or tweaks suboptimal cuts to better values.

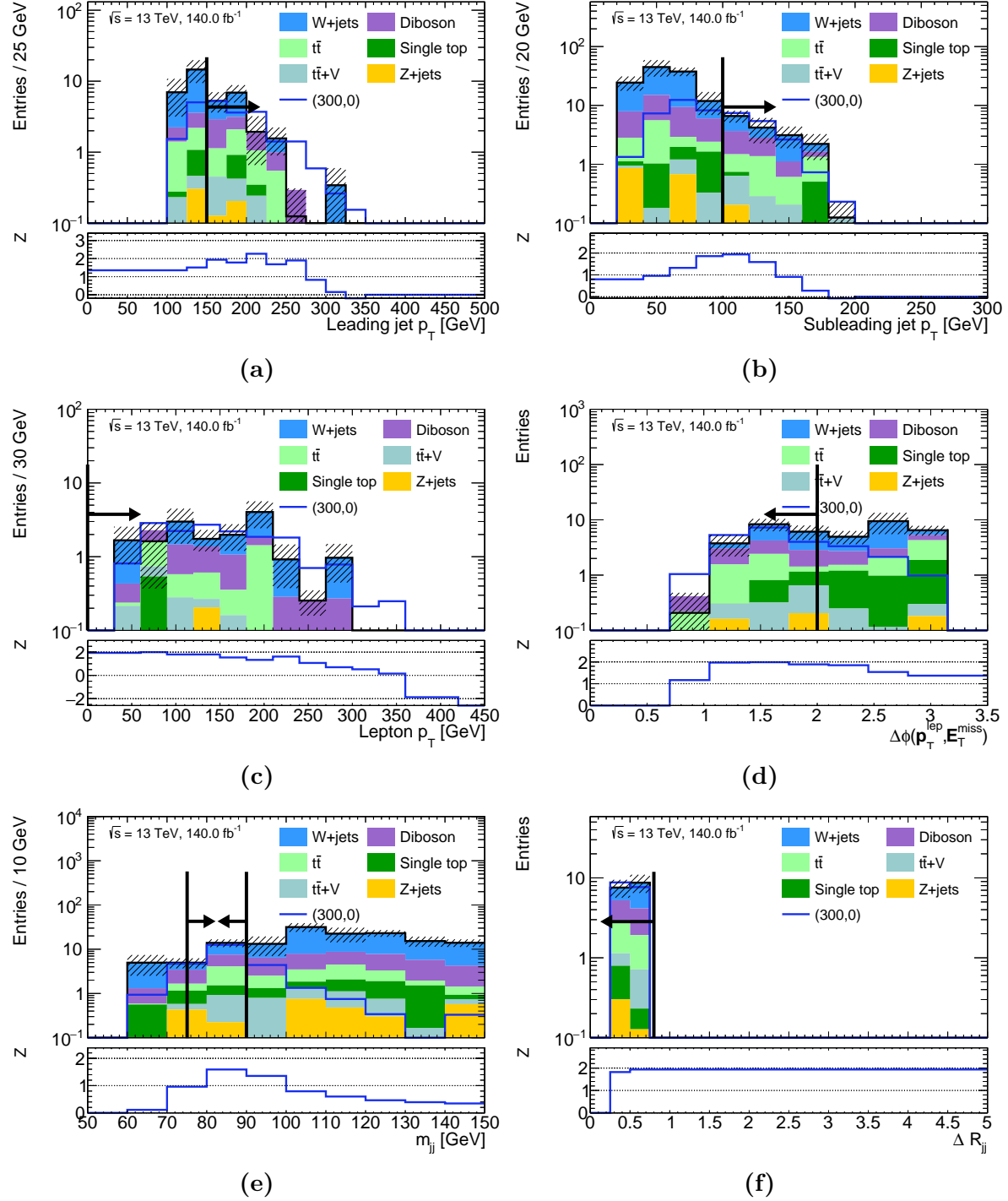


Figure A.4: Second set of N-1 plots for the chosen cut combination for the $(300, 0)$ signal point. These plots form the basis for a manual optimisation step that removes some of the unnecessary cuts or tweaks suboptimal cuts to better values. In fig. (e), for illustration purposes, the lower requirement is not applied while the upper cut is scanned.

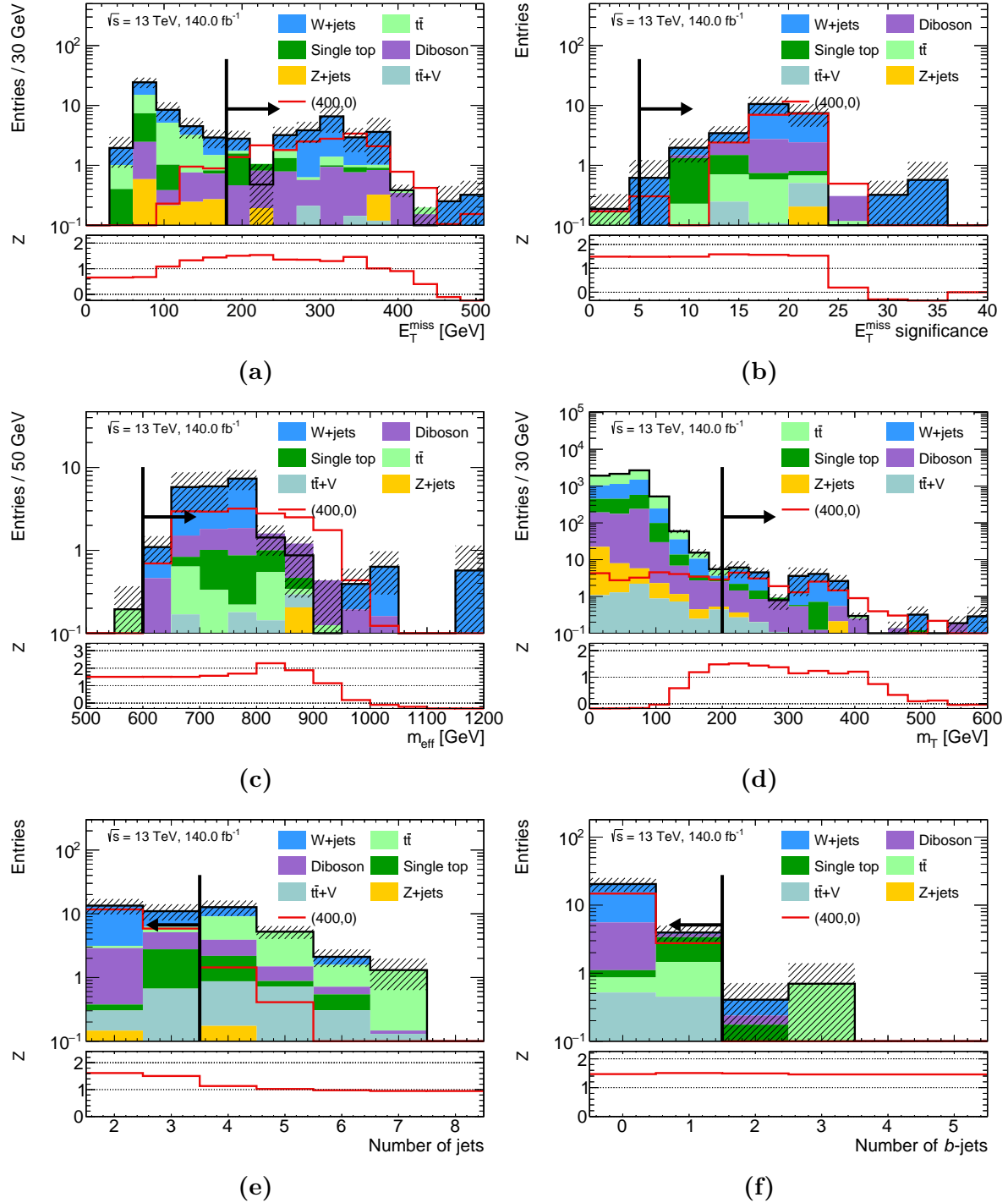


Figure A.5: First set of N-1 plots for the chosen cut combination for the $(400, 0)$ signal point. These plots form the basis for a manual optimisation step that removes some of the unnecessary cuts or tweaks suboptimal cuts to better values.

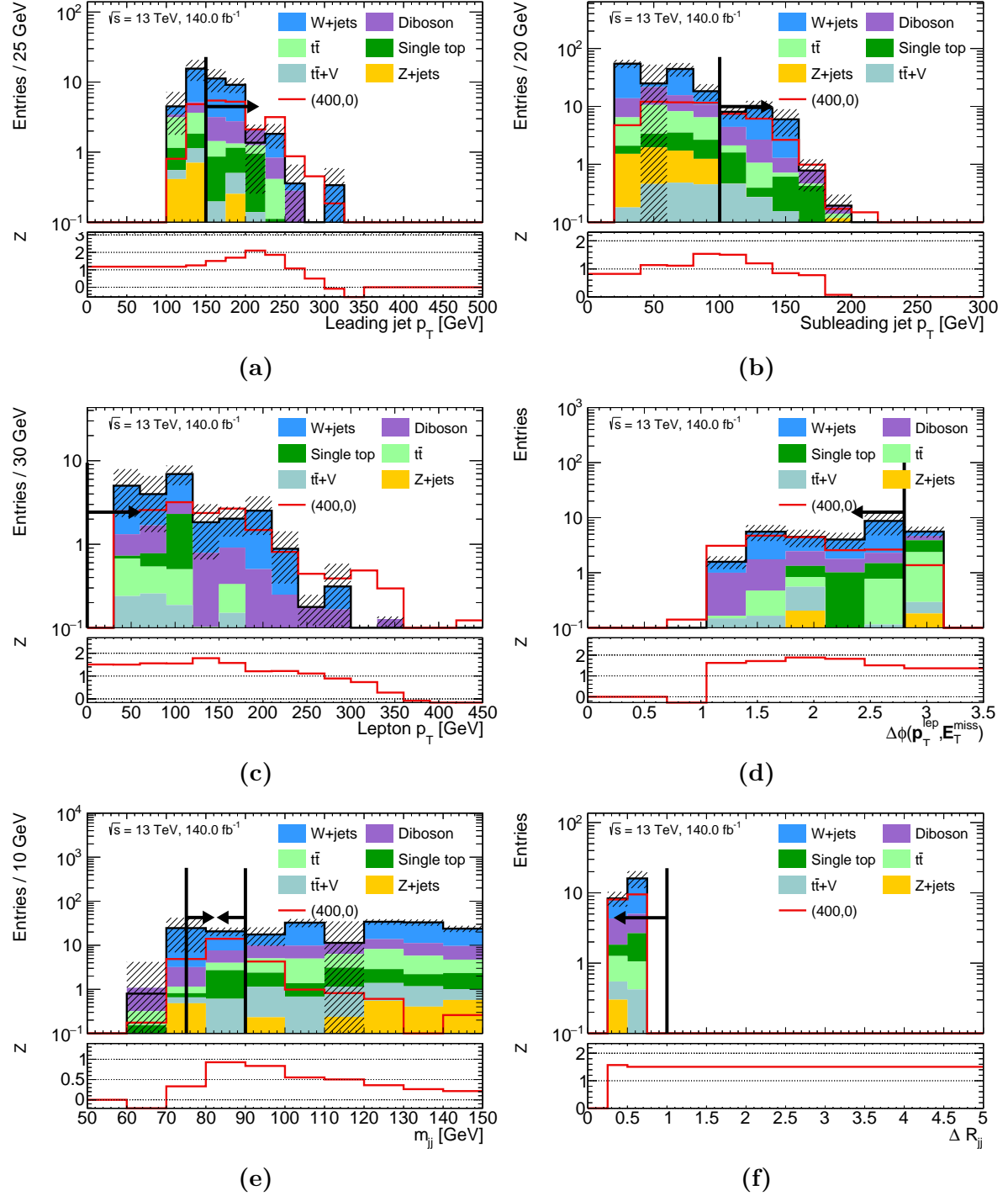


Figure A.6: Second set of N-1 plots for the chosen cut combination for the $(400, 0)$ signal point. These plots form the basis for a manual optimisation step that removes some of the unnecessary cuts or tweaks suboptimal cuts to better values. In fig. (e), for illustration purposes, the lower requirement is not applied while the upper cut is scanned.

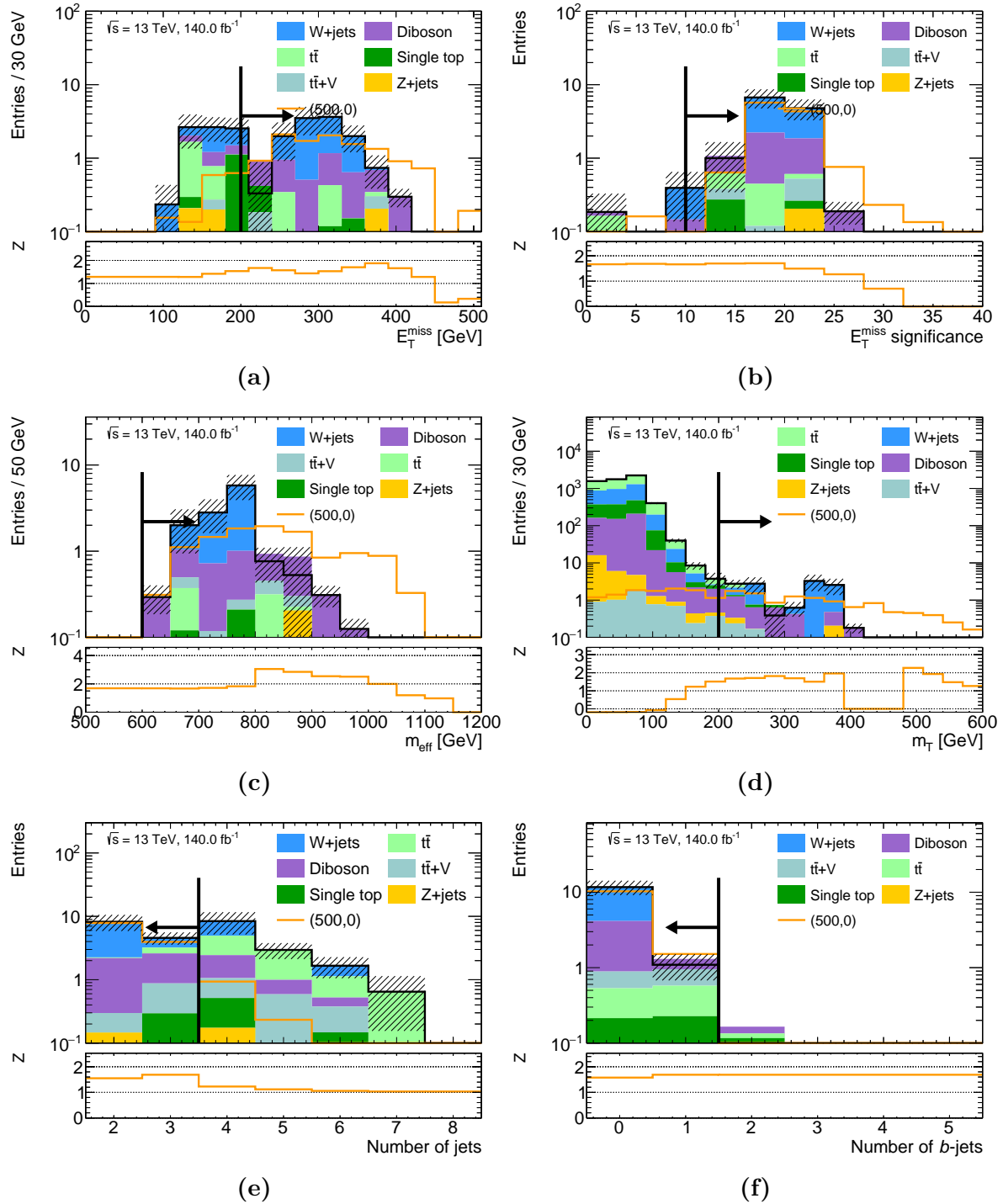


Figure A.7: First set of N-1 plots for the chosen cut combination for the (500, 0) signal point. These plots form the basis for a manual optimisation step that removes some of the unnecessary cuts or tweaks suboptimal cuts to better values.

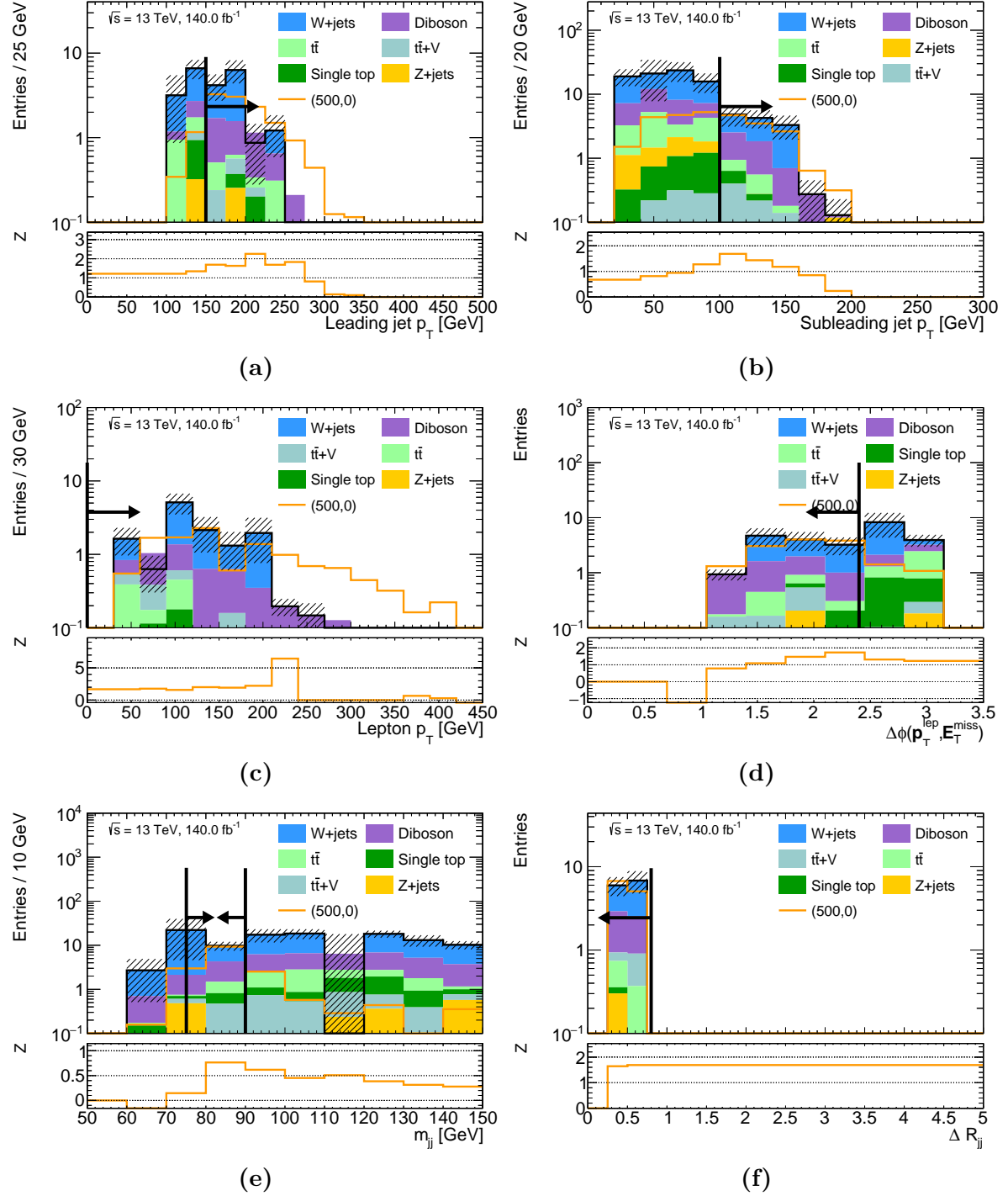


Figure A.8: Second set of N-1 plots for the chosen cut combination for the $(500, 0)$ signal point. These plots form the basis for a manual optimisation step that removes some of the unnecessary cuts or tweaks suboptimal cuts to better values. In fig. (e), for illustration purposes, the lower requirement is not applied while the upper cut is scanned.

A.2 Truth- and full-reconstruction-level comparisons

This section summarises the comparisons between the (400,0) signal sample at truth-level and full-reconstruction-level, after applying smearing on the truth sample with `SimpleAnalysis` [89]. The truth sample contains roughly 2 million MC events after preselection and is used to train the neural net in section 6.6. In general, the agreement between truth and full reconstruction is found to be sufficiently good for the observables used within the machine learning algorithm. The m_T distribution shows a slight mis-modeling, even after smearing. Furthermore, the lepton p_T distribution reveals that the truth sample still predicts more low- p_T leptons than the fully reconstructed sample, even though an approximation of detector efficiencies is included through `SimpleAnalysis`.

Although these minor differences reduce the performance of the neural nets when testing with events from the fully reconstructed sample, the gain in sensitivity due to the increased truth statistics is found to prevail.

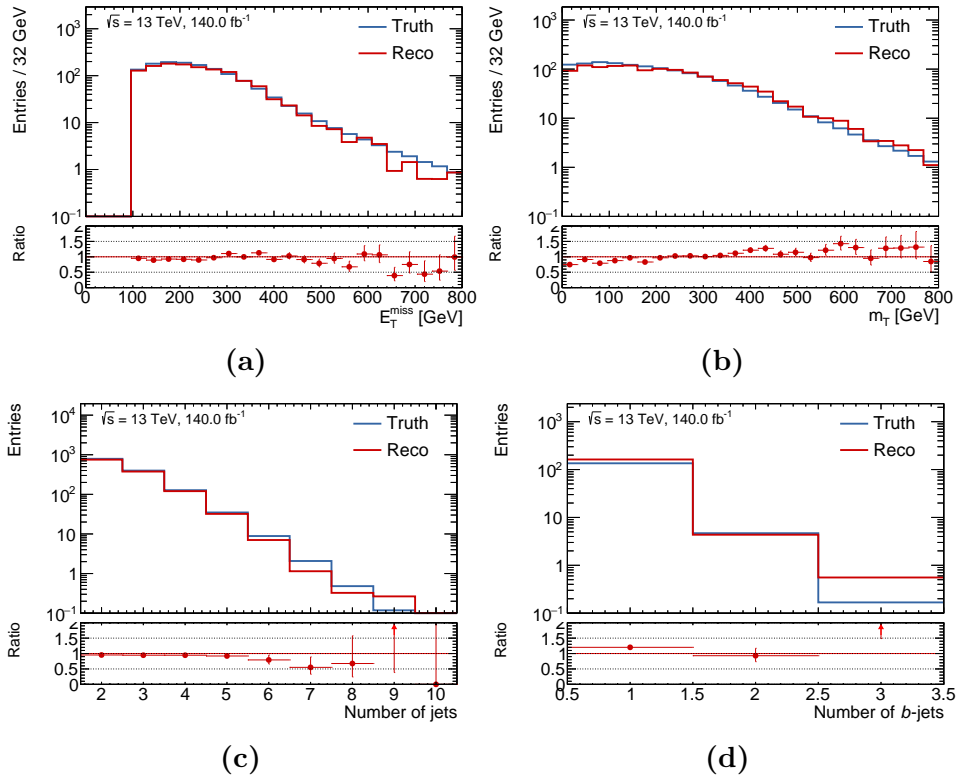


Figure A.9: First set of ratio plots comparing the various distributions for the (400,0) signal point at truth and full reconstruction. The truth sample has been smeared. In general, the agreement is found to be sufficiently good. Most of the differences fall within statistical uncertainty.

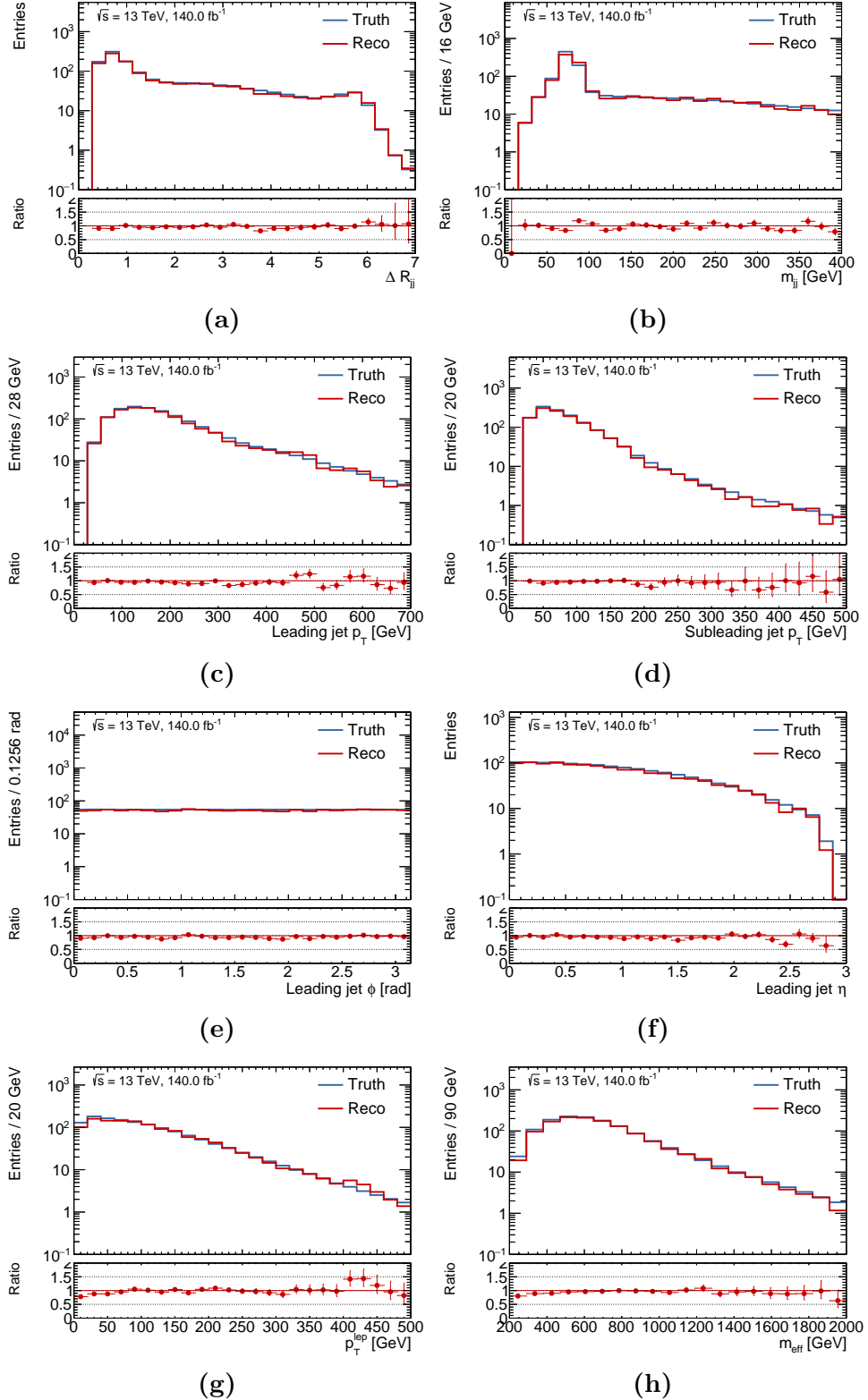


Figure A.10: Second set of ratio plots comparing the various distributions for the (400,0) signal point at truth and full reconstruction. The truth sample has been smeared. In general, the agreement is found to be sufficiently good. Most of the differences fall within statistical uncertainty.

A.3 Available statistics for training MLP

Table A.1 summarises the raw number of events available for training neural nets both before and after requiring $m_T > 110 \text{ GeV}$. A preselection of exactly one lepton and at least two jets is always applied. The available number of fully reconstructed signal events is extremely low, hence the need for a large statistics truth sample, where more than 600.000 events are still available even after requiring $m_T > 110 \text{ GeV}$.

Table A.1: Number of events before and after requiring $m_T > 110 \text{ GeV}$ on top of the preselection of exactly one lepton and at least two jets.

Process	Preselection	Preselection + $m_T > 110 \text{ GeV}$
Truth signal	2345000	644962
Reco signal	8225	5548
$W + \text{jets}$	66647010	5372518
$Z + \text{jets}$	16533269	1481975
Diboson	9703947	1541441
$t\bar{t}$	22072205	2263805
Single top	4344810	318643
$t\bar{t} + V$	3552619	664332

Appendix B

B.1 Scatter plots comparing truth and reco yields in the SRs

The following figs. B.1 and B.2 show scatter plots comparing the truth and reco yields in the remaining SRs. Each signal point in the grid corresponds to a single point in the scatter plot, indicating how well the number of truth events agrees with the number of reco events, expected through MC. The dashed black line represents the main diagonal where $N_{\text{events}}^{\text{truth}} = N_{\text{events}}^{\text{reco}}$. The left column of each figure shows the results for unsmeared truth samples, while the right column shows the results for smeared truth samples. In general, the spread of the points in the scatter plots is much smaller for the smeared truth samples. Additionally, the mean ratio between truth and reco events is very close to 1 for smeared truth samples, while it is far away from 1 for unsmeared truth samples. The missing b -tag and jet efficiencies in the unsmeared truth samples are also visible, causing an underestimation (overestimation) of events in b -tag (b -veto) SRs.

In general, a significant increase in agreement between truth and reco is observed after applying smearing techniques on the truth samples.

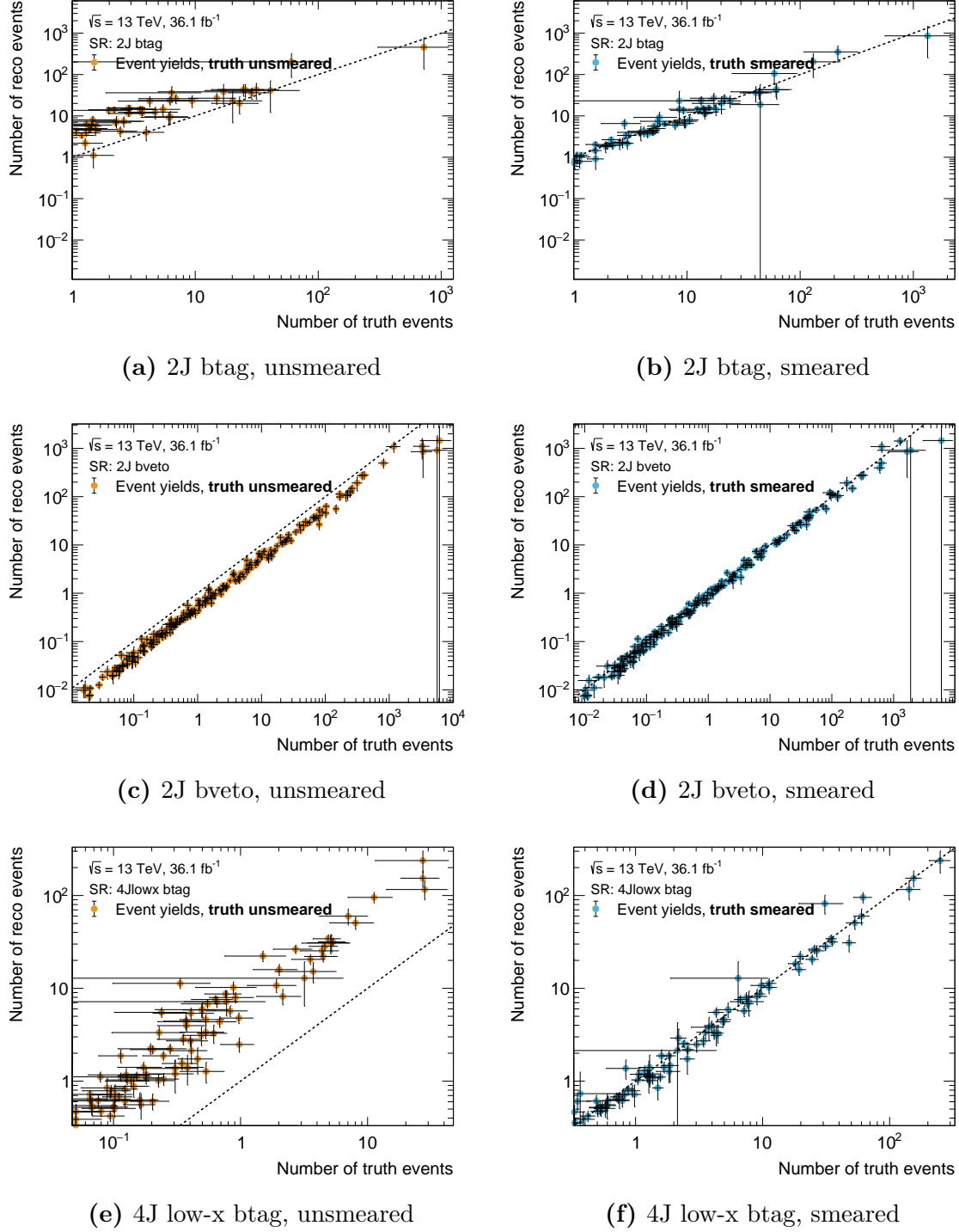


Figure B.1: First set of reco- and truth-level yields comparisons in the SRs. All m_{eff} -bins are added up to one single bin per SR. The left column shows the truth yields before smearing and the right column after smearing the truth MC samples. The dashed line is the diagonal where $N_{\text{events}}^{\text{truth}} = N_{\text{events}}^{\text{reco}}$. The error bars include MC statistical uncertainty. A significant improvement is seen in the agreement between truth and reco yields in the SRs after applying smearing on the truth samples.

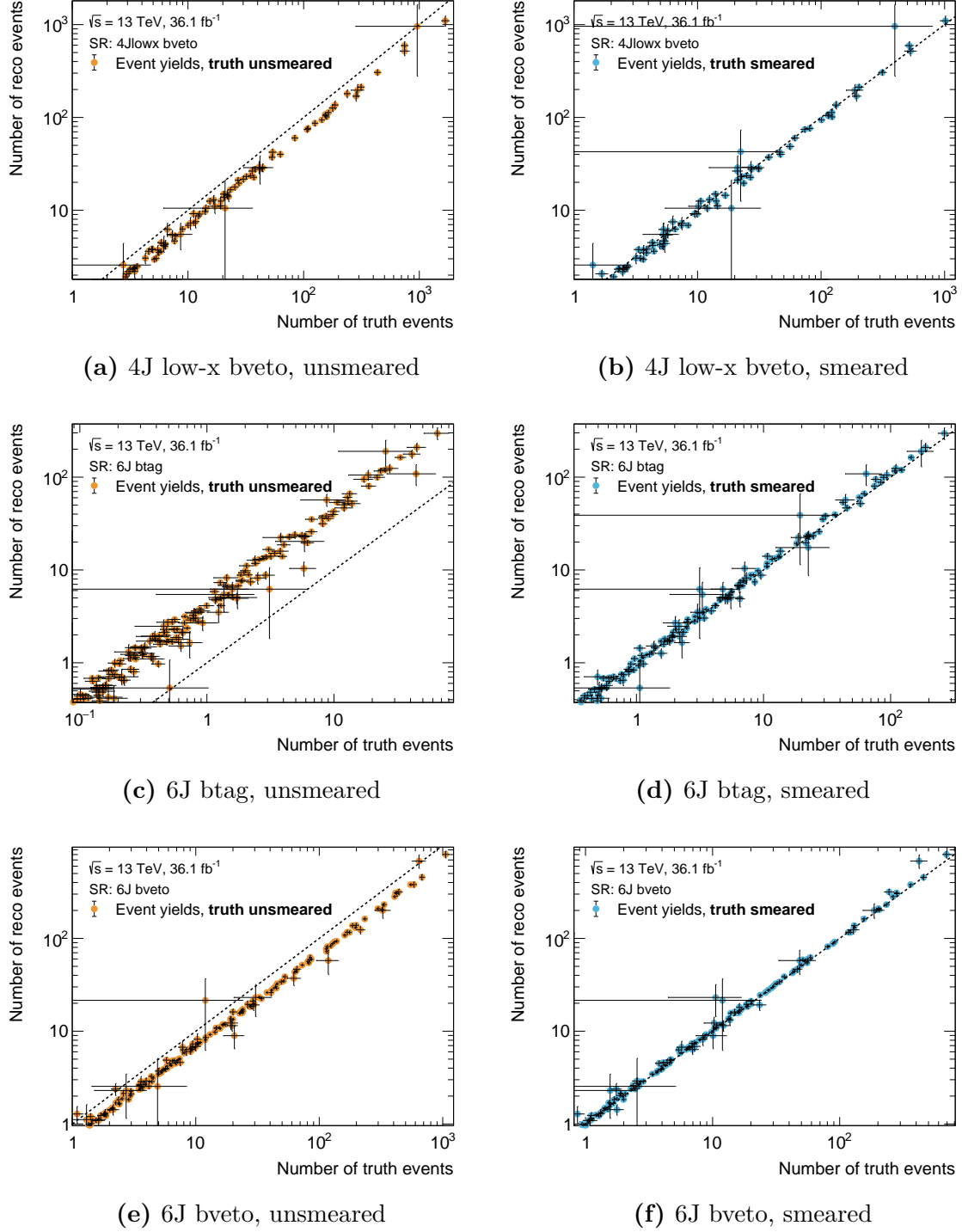


Figure B.2: Second set of reco- and truth-level yields comparisons in the SRs. All m_{eff} -bins are added up to one single bin per SR. The left column shows the truth yields before smearing and the right column after smearing the truth MC samples. The dashed line is the diagonal where $N_{\text{events}}^{\text{truth}} = N_{\text{events}}^{\text{reco}}$. The error bars include MC statistical uncertainty. A significant improvement is seen in the agreement between truth and reco yields in the SRs after applying smearing on the truth samples.

B.2 Available truth samples for the gluino one-step model

Not all signal points in the gluino one-step grid had corresponding truth-level samples that were still available. Therefore, the truth-level grids are significantly coarser than the reco-level grids. This results in minor interpolation artefacts, especially when directly comparing exclusion limits obtained with reco- and truth-level samples, respectively.

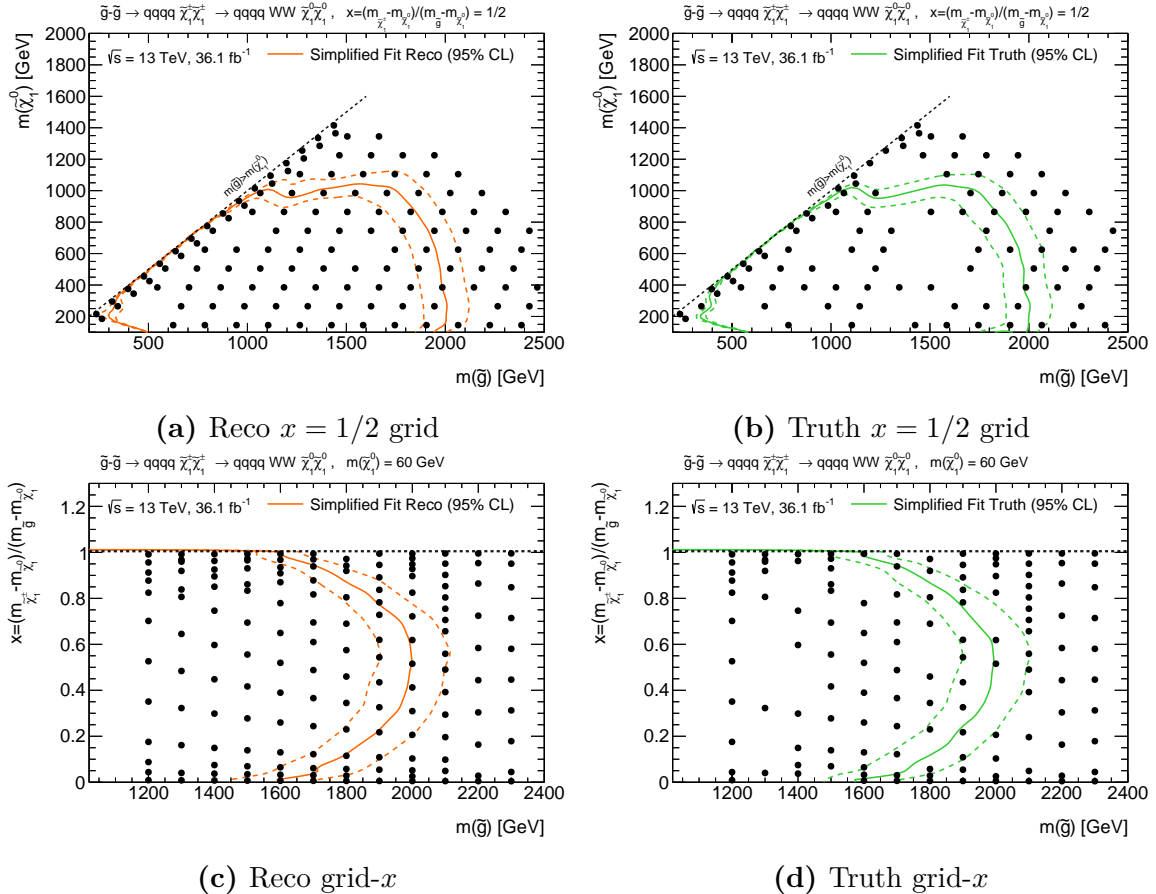


Figure B.3: Illustration of the difference in the availability of signal points for the gluino grids depending on whether truth-level or reco-level signal grids are considered. Not every reco-level signal sample has a corresponding truth-level sample that is still available for the presented studies. All values in the left column stem from public analysis results [26].

B.3 pMSSM parameter scan ranges

Table B.1 summarises the scan ranges used for the 19 pMSSM parameters in order to sample the model space. The 4 TeV upper bound on most of the mass parameters is used in order for all the states to be kinematically accessible at the LHC. Since $|A_t|$ affects loop corrections to the mass of the Higgs boson, a larger range is permitted for this parameter in order to increase the fraction of sampled models with a lightest Higgs mass close to the measured value [28].

Table B.1: Scan ranges used for each of the 19 pMSSM parameters.

Parameter	min	max	Note
$m_{\tilde{L}_1}$ ($= m_{\tilde{L}_2}$)	0 GeV	4 TeV	Left-handed slepton (first two gens.) mass
$m_{\tilde{e}_1}$ ($= m_{\tilde{e}_2}$)	0 GeV	4 TeV	Right-handed slepton (first two gens.) mass
$m_{\tilde{L}_3}$	0 GeV	4 TeV	Left-handed stau doublet mass
$m_{\tilde{e}_3}$	0 GeV	4 TeV	Right-handed stau mass
$m_{\tilde{Q}_1}$ ($= m_{\tilde{Q}_2}$)	0 GeV	4 TeV	Left-handed squark (first two gens.) mass
$m_{\tilde{u}_1}$ ($= m_{\tilde{u}_2}$)	0 GeV	4 TeV	Right-handed up-type squark (first two gens.) mass
$m_{\tilde{d}_1}$ ($= m_{\tilde{d}_2}$)	0 GeV	4 TeV	Right-handed down-type squark (first two gens.) mass
$m_{\tilde{Q}_3}$	0 GeV	4 TeV	Left-handed squark (third gen.) mass
$m_{\tilde{u}_3}$	0 GeV	4 TeV	Right-handed top squark mass
$m_{\tilde{d}_3}$	0 GeV	4 TeV	Right-handed bottom squark mass
$ M_1 $	0 GeV	4 TeV	Bino mass parameter
$ M_2 $	0 GeV	4 TeV	Wino mass parameter
$ \mu $	0 GeV	4 TeV	Bilinear Higgs mass parameter
M_3	0 GeV	4 TeV	Gluino mass parameter
$ A_t $	0 GeV	8 TeV	Trilinear top coupling
$ A_b $	0 GeV	4 TeV	Trilinear bottom coupling
$ A_\tau $	0 GeV	4 TeV	Trilinear τ lepton coupling
M_A	0 GeV	4 TeV	Pseudoscalar Higgs boson mass
$\tan \beta$	1	60	Ratio of the Higgs vacuum expectation values

Danksagung

An dieser Stelle möchte ich mich herzlich bei allen bedanken, die mich bei der Anfertigung dieser Arbeit unterstützt haben. Insbesondere danke ich herzlich

- Prof. Dr. Dorothee Schaile für die Möglichkeit, diese Arbeit an ihrem Lehrstuhl durchzuführen sowie das Korrekturlesen der Arbeit.
- Dr. Jeanette Lorenz für die ausgezeichnete Betreuung, die vielen Anregungen, sowie die ehrliche und konstruktive Kritik beim Korrekturlesen dieser Arbeit. Sie hat es mir ermöglicht aktiv im 1-Lepton Analyseteam an der Suche nach Supersymmetrie mitwirken zu können.
- Dr. Nikolai Hartmann für die unzähligen Diskussionen über den Sinn und Unsinn der Datenanalyse mit und ohne ATLAS Software. Vielen Dank für die stets geduldige und ausführliche Beantwortung meiner Fragen, sowie das Bereitstellen unzähliger Zeilen Code, ohne die vieles schwieriger gewesen wäre.
- Allen Mitgliedern des Lehrstuhls Schaile für die angenehme und freundliche Arbeitsatmosphäre.
- Allen Freunden, die stets da waren, wenn ich sie gebraucht habe.

I also want to thank the entire 1-lepton analysis team, especially the coordinators Jeanette Lorenz, Da Xu and Alberto Cervelli. Thank you for the always supportive and enjoyable work environment. Many thanks also to Valentina Tudorache for patiently answering all my questions as well as all the entertaining conversations.

En léiwen Merci och dem Yannick Erpelding fir d'Korrekturliesen — och wann en net alles verstanen huet — an dem Nick Beffort, fir all déi domm Reddit Posts an dei onzähleg Stonnen zesummen mat enger Spezi an der Hand.

Zu gudden Läschte, wëll ech op dëser Platz menger ganzer Famill merci soen, virun allem mengen léiwen Elteren an menger wonnerbarer Schwëster. Merci dass dir mëch bei allem waat ech maachen énnerstëtzzt an dass ech émmer op iech zielen kann, och wann ech weit fort sin. Ouni iech wier daat heiten net méiglech gewiescht. Besonneschen Merci och dem Nathalie Münster, dofir dass et mech seit Joren émmer énnerstëtzzt an émmer fir mech do as, och wann ech heiansdo depriméiert oder duercherneen sin.

Selbstständigkeitserklärung

Hiermit erkläre ich, die vorliegende Arbeit mit dem Titel

**Sensitivity studies for a search for charginos in final states with one lepton
with the ATLAS detector and interpretation of a search for gluinos and
squarks in the pMSSM**

Sensitivitätsstudien zu einer Suche nach Charginos in Endzuständen mit einem Lepton
mit dem ATLAS Detektor und Interpretation einer Suche nach Gluinos und Squarks im
pMSSM

selbstständig verfasst zu haben und keine anderen als die in der Arbeit angegebenen
Quellen und Hilfsmittel benutzt zu haben.

Eric Schanet
München, den 17. September 2018

